Fabrication and characterization of nanodevices based on III-V nanowires

Andrès De de Luna Bugallo Luna Bugallo

▶ To cite this version:

Andrès De de Luna Bugallo Luna Bugallo. Fabrication and characterization of nanodevices based on III-V nanowires. Other [cond-mat.other]. Université Paris Sud - Paris XI, 2012. English. NNT : 2012PA112117 . tel-00731763

HAL Id: tel-00731763
https://theses.hal.science/tel-00731763

Submitted on 13 Sep 2012

HAL is a multi-disciplinary open access archive for the deposit and dissemination of scientific research documents, whether they are published or not. The documents may come from teaching and research institutions in France or abroad, or from public or private research centers.

L'archive ouverte pluridisciplinaire **HAL**, est destinée au dépôt et à la diffusion de documents scientifiques de niveau recherche, publiés ou non, émanant des établissements d'enseignement et de recherche français ou étrangers, des laboratoires publics ou privés.

No D'ORDRE :

THÈSE DE DOCTORAT

Spécialité : Physique

École Doctorale "Sciences et Technologies de l'Information des Télécommunications et des Systèmes"

présentée par :

Andrés de Luna Bugallo

Fabrication and characterization of nanodevices based on III-V nanowires

Soutenue le ....devant les membres du jury :

François Julien	Directeur de thèse
Jean-Claude De Jaeger	Rapporteur
Abdallah Ougazzaden	Rapporteur
Christophe Durand	Examinateur
Daniel Bouchier	Examinateur
Maria Tchernycheva	Co-directeur

GENERAL INTRODUCTION **5**

1. INTRODUCTION **8**

1.1 NANOSCIENCE AND NANOWIRES **8**
1.2 SEMICONDUCTOR MATERIALS **9**
1.3 CRYSTALLINE STRUCTURE **10**
POLARITY 11
HETEROSTRUCTURES 13
1.4 ELECTRONIC PROPERTIES **13**
1.5 NANOWIRE EXPITAXY **16**
PARTICLE-ASSISTED GROWTH 18
PARTICLE-FREE GROWTH 19
NANOWIRE GROWTH OF III-VS ON SI 19
SELECTIVE AREA GROWTH 20
1.6 APPLICATIONS **21**
PHOTODETECTORS 21
LEDS 23
PHOTOVOLTAIC DEVICES 24
LASERS 25

2. NANOFABRICATION **29**

INTRODUCTION **29**
2.1 FABRICATION OF SINGLE NANOWIRE DEVICES **31**
2.1.1 SUBSTRATE PREPARATION 31
2.1.2 NANOWIRE DISPERSION 32
2.1.3 ELECTRON BEAM LITHOGRAPHY 33
2.1.4 METALLIZATION 41
2.1.5 LIFT-OFF 42
2.1.6 CONTACT ANNEALING 43
2.2 PLANARIZATION **43**
2.2.1 HSQ DEPOSITION AND TRANSFORMATION 45
2.2.2 HSQ ETCHING 47
2.2.3 HSQ REMOVAL 48
2.3 FABRICATION OF ARRAY NANOWIRE DEVICES **49**
2.3.1 ENCAPSULATION AND TRANSFORMATION 50
2.3.2 RIE ETCHING 51
2.3.3 PHOTOLITHOGRAPHY 52
2.3.4 INDIUM TIN OXIDE DEPOSITION 55
CONCLUSIONS **58**

3. PHOTODETECTORS BASED ON NANOWIRE ENSEMBLES **62**

3.1 INTRODUCTION **62**
3.2 NANOWIRE PHOTODETECTOR STRUCTURE **69**
3.3 ELECTRICAL PROPERTIES OF THE NANOWIRE PHOTODETECTOR **71**
3.4 ELECTRO-OPTICAL RESPONSE **73**
3.5 OPERATION SPEED **75**
3.6 PHOTOCURRENT SPECTROSCOPY **76**
3.7 DEPENDENCE ON THE INCIDENT POWER **77**
3.8 OPTICAL BEAM INDUCED CURRENT **78**
CONCLUSIONS **80**

4. GAN/ALN SINGLE NANOWIRE PHOTODETECTORS **84**

4.1 NANOWIRE STRUCTURE **85**
4.2 MICRO PHOTOLUMINESCENCE SPECTROSCOPY **87**
4.3 CATHODOLUMINESCENCE **89**
4.4 ELECTRONIC TRANSPORT **92**
4.4.1 INFLUENCE OF ENVIRONMENTAL CONDITIONS 94
4.4.2 RESONANT TUNNELING 95
4.5 OPTICAL RESPONSE AND PHOTOCURRENT SPECTROSCOPY **97**
CONCLUSIONS **102**

5. INGAN/GAN SINGLE WIRE PHOTODETECTORS AND LIGHT EMITTERS **105**

INTRODUCTION **105**
5.1 GAN/INGAN QW STRUCTURE **106**
5.2 WIRE STRUCTURE OF AN N-I-N JUNCTION: THE T929 SAMPLE **108**
5.2.1 MICRO PHOTOLUMINESCENCE SPECTROSCOPY 110
5.2.2 ELECTRICAL CHARACTERIZATION AND OPTICAL RESPONSE 111
5.2.3 OPERATION SPEED 113
5.2.4 PHOTOCURRENT SPECTROSCOPY 114
5.2.5 OPTICAL BEAM INDUCED CURRENT 115
5.3 INGAN/GAN NANOWIRE LEDS **116**
5.3.1 WIRE P-I-N JUNCTION STRUCTURES : SAMPLES T1163, T1164 AND T1165 **118**
5.3.2 PHOTOLUMINESCENCE 119
5.3.3 IDENTIFICATION OF SPECTRAL CONTRIBUTIONS BY CATHODOLUMINESCENCE 121
5.3.4 ELECTROLUMINESCENCE 123
5.3.5 ON-CHIP INTEGRATION 127
CONCLUSIONS 129

CONCLUSIONS AND PERSPECTIVES **133**

General introduction

In the recent years the development in the field of III-N semiconductor technology has been spectacular. Numerous GaN-based devices including light emitting diodes (LEDs), laser diodes (LDs), photodetectors and high power microwave power switches have been developed and brought to the market. The driving force behind the fast development of III-N semiconductors has been the demand for short wavelength emitters. To date there exists only a few semiconductor material systems suitable for such applications. Several II-VI semiconductors such as ZnSe and ZnS have been extensively studied but the devices short lifetime limits their use (Nakamura, 1998). Among the II-VI materials, zinc oxide (ZnO) holds promises as a material for blue and UV optoelectronics, but difficulties in p-type doping hinder the use of ZnO in devices (Klingshirn, 2007). Therefore, the III-N material system is currently the only practical solution for short wavelength semiconductor detectors and emitters.

The efficiency of devices based on III-N materials has improved substantially in the last decades by reducing the dimensions, and changing the design using e.g. quantum wells (QW), multiple QWs (superlattice heterostructures) and quantum dots (QDs) in the active layers. Such structures not only confine the carriers in the growth direction but also passivate surface states at the lower bandgap material surface. However, the choice of materials for the growth of defect free heterostructures is limited by the lattice mismatch issues. This is also one of the main reasons inhibiting the integration of III-V materials on Si.

Such problems can be avoided in the growth of III-N nanowires (NWs). NWs are structures with lengths up to few microns. However their small cross section (10ths of nanometers) favors an efficient elastic strain relaxation inhibiting the generation of structural defects. This fact opens the possibility of growing high-quality materials with an important lattice mismatch with the substrate. At the same time, III-V NWs preserve and enhance the properties of 2D layer epitaxial growth allowing the possibility to form axial heterostructures, quantum dots, p- and n-type doping but also more complex structures such as radial heterostructures and branched nanowires. Because of these advantages, III-N nanowires have been proposed for a wide variety of applications. In particular they are consider as promising building blocks in nanoscale electronics and optoelectronics devices; such as

photodetectors (Soci, 2007)(Kouwe, 2010), transistors (Motayed, 2006), biosensors (Patolsky, 2006), light sources (Qian et al., 2008)(Koester, 2011), solar cells (Dong, 2009), etc.

In this context, the aim of the present work is to develop the fabrication of III-N nanowires devices presenting strategies to assemble single and ensemble nanowires into functional components, and to understand the device behavior by electrical and optical characterizations. The manuscript of this thesis is subdivided as follows:

In the first chapter I present a brief introduction to the structural, optical and electronic properties of III-V semiconductors with a special focus on nitride materials. Then, I give a general description of the different growth techniques of semiconductor nanowires emphasizing the possibility to integrate them on highly mismatched substrates such as silicon. The rest of the chapter provides a quick overview of the state of art in semiconductor nanowires and their applications.

The second chapter focuses on the technological processing to fabricate devices based on nanowires. I describe the different steps in order to electrically address a single nanowire by electron beam lithography as well as the metallization process for achieving ohmic contacts for n-type and p-type GaN nanowires. In the same context, I show the influence of the nanowires diameter and the strategy to follow in the case when it exceeds 350 nm. Then, I expose a second type of devices based on vertical nanowire ensembles. Its fabrication procedure involves the encapsulation of the nanowires on a dielectric material, optical lithography (to define the device dimensions and to carry out the metal depositions) and the use of indium-tin oxide to contact the nanowire tips.

The third chapter is dedicated to the study of a visible-blind photodetector based on p-i-n GaN nanowires ensembles grown on a Si (111) substrate. Using electrical characterization in the dark and under UV illumination, I show that these devices exhibit a peak responsivity of 0.47 A/W exceeding that of thin film counterparts. I then study the spectral response of the photocurrent. The devices show an onset at 3.27 eV and a high UV-to-visible rejection ratio; in addition, no spectral contribution from the Si substrate is present.

Chapter four presents a study of UV photodetectors based on single heterostructured nanowires. The photodetector consists of an n-i-n structure containing GaN/AlN quantum discs in the intrinsic region of the nanowires. After describing the structural characteristics of the studied samples, I focus on the results of photoluminescence and cathodoluminescence spectroscopy evidencing the quantum disc emissions. Spectral contributions above and below the GaN bandgap are related to the variation of the discs thickness and the quantum confined Stark effect. Then, I present electronic transport in these nanowires; I show that when electrons are forced to pass through the multi quantum disc region, the electron transport occurs by tunneling which is revealed by a negative differential resistance in the I-V curves. I then study the spectral response of the nanowire photodetectors. The photocurrent spectra show a sub-band-gap peak related to the interband absorption between the confined states in the large quantum discs. The built-in electric field favors the extraction of photogenerated carriers from the discs.

The last chapter is dedicated to the demonstration of photodetectors and light emitters based on radial InGaN/GaN multi quantum wells (MQW) embedded in GaN wires. I show how the spectra, obtained by photoluminescence and cathodoluminescence experiments vary according to the excitation spot position. I present the photoresponse results for wires used as photodetectors showing a contribution below the GaN band gap. Optical beam induced current (OBIC) measurements demonstrate that, this signal is exclusively generated in the InGaN MQW region. I then present the fabrication and characterization of LEDs based on these wires. The electroluminescence show a red shift when the In content in the QWs increases, which is in good agreement with photoluminescence results. I also show that the electroluminescence signal consists of two major contributions depending on the levels of current injection, due to the presence of radial and axial MQW systems. Finally, I propose an integrated optical system combining a simple wire emitter and detector, which opens prospects for future photonic structure for nanocircuits.

1. Introduction

In this chapter I first present the general properties of III-nitride semiconductors that will be needed for the interpretation of experimental results. Then, I give a brief overview of the two main nanowire growth modes, particle-assisted and particle-free, and I present different types of nanowire heterostructures. The last part is dedicated to the review of optoelectronic devices based on nanowires.

1.1 Nanoscience and nanowires

It is well known that systems composed of a reduced number of atoms exhibit quantum effects that can have dramatic implications for their properties, behavior and potential applications. With the reduction of the system size, the physical principles important to atoms, but normally negligible in bulk, begin to increase in importance. Size effects become important when at least one dimension of a crystal is reduced to the order of hundreds of atoms, which corresponds to the length scale of nanometers. This has instigated the explosive growth of the fields of nanoscience and nanotechnology -- the study and manipulation of matter at a scale of tens of nanometers. As understanding the unique properties of nanostructures increases, so does the interest in and potential of practical applications that take advantage of these properties.

Nanowires are quasi 1-dimensional semiconductor nano-crystals, they have a diameter < 100 nm, whereas the axis is considerably longer, typically in the µm range. Such structures are of particular interest for device applications, as they exhibit unique and fascinating physical properties (mechanic toughness, higher carrier mobility, luminescence efficiency, lowered lasing threshold). In the last decade, these systems have been one main topics of research of the scientific community, to the point of considering as fundamental 'building blocks' for

the realization of entirely new classes of nano-scale devices and circuits, with applications stretching from photonics to nano-electronics, and from sensors to photovoltaics.

1.2 Semiconductor materials

Among different domains addressed by the nanoscience, one of the most important research fields is related to the study of semiconductor materials. Semiconductor technology has enabled the information technology revolution. Computers, game consoles, satellites, mobile phones are now integral parts of daily life.

A semiconductor exhibits a band gap, which is an energy interval in which no electron states are allowed. In a semiconductor at low temperature the states below the gap are fully occupied by electrons, and the states above the gap are empty. Since completely filled bands (or empty bands) carry no net current, these materials are insulators at absolute zero (Weisstein, 1976). However, at room temperature these materials have a finite conductance that can be controlled by introducing impurity atoms (doping) and applying electrical fields. The complimentary metal oxide semiconductor (CMOS) transistor technology, which is the core of the current computer technology, is based on the ability to "switch" a semiconductor material (generally silicon) between a conducting and a non-conducting state.

The so-called III-V semiconductors are compound materials composed of elements from groups III and V of the periodic system, for example, GaAs, GaN and InP. They are more expensive than Si, and the processing technology is less mature. However, these materials have functionality that Si does not possess. The most important difference is perhaps that most of them exhibit a so-called direct band gap, meaning that electrons can relax to lower energy states radiatively (recombine with holes) with conserved momentum.

The group III-nitride family, consisting of gallium nitride (GaN), aluminum nitride (AlN), indium nitride (InN), their alloys and heterostructures exhibit some unique properties among III-V semiconductors, such as a band gap covering a large domain ranging from the deep UV to the infrared, high breakdown voltage, high thermal conductivity, chemical inertness, mechanical stability, etc. Because of these properties, group-III nitrides have been considered as very promising materials for optoelectronic devices.

1.3 Crystalline structure

In semiconductor materials atoms are organized in a three dimensional lattice, where the same periodic structure is repeated over the space of the crystal. The group III-nitrides can crystallize either in hexagonal (wurtzite) or cubic (zinc blende) structures. Both of these structures can be grown either by MBE or MOVPE epitaxial methods. However, the wurtzite structure is thermodynamically more stable and therefore is more widespread in optoelectronic applications. In this work the nanowire samples have a wurtzite crystal structure only, therefore we focus our study on this structure.

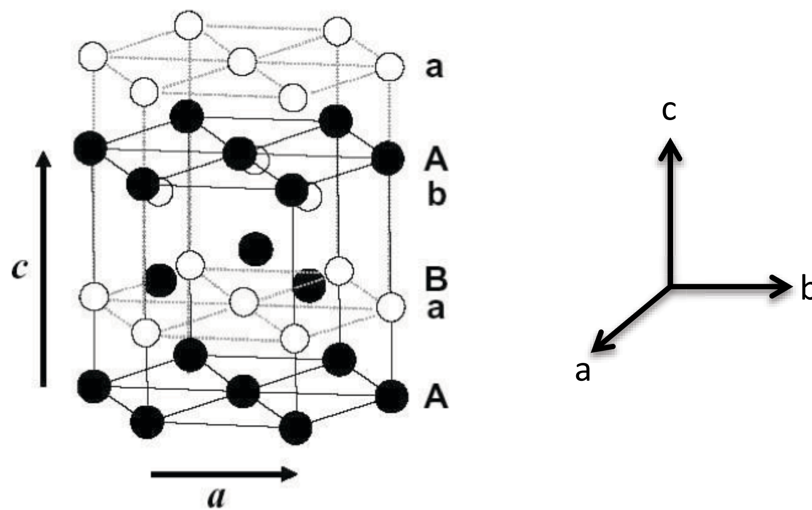

Figure 1.1 Wurtzite Structure

The Bravais lattice of the wurtzite structure is hexagonal, and the three vectors, $\vec{a}$, $\vec{b}$, and $\vec{c}$, define the lattice. Wurtzite structure is constituted of two sub-compact hexagonal networks, which form an ABAB type stacking along the c [0001] direction as shown in figure 1.1. The hexagonal unit cell is defined by two vectors a (length of the hexagon side) and c (height of the hexahedron). The wurtzite structure consists of two interpenetrating hexagonal close-packed (hcp) sublattices, each with one type of atom, shifted along the c-axis by the distance 3c/8 in the case of ideal wurtzite structure. This parameter can deviate from this ideal value and change from material to material. The crystallographic parameters of nitrides are summarized in Table 1.1 (Vurgaftman, 2001).

	GaN	AlN	InN
a	3,189 Å	3,112 Å	3,545 Å
c	5,185 Å	4,982 Å	5,703 Å
c/a	1,626	1,601	1,608
u/c	0,337	0,382	0,375

Table 1.1 Lattice constants for III-V materials at room temperature crystallized in wurtzite structure.

Polarity

One of the main characteristics of the wurtzite structure is that it does not have a symmetry inversion center, which leads to a non-equivalence of the [0 0 0 1] and [0 0 0 -1] directions. There are two different polarities depending on the orientation of element III: if the binding metal-nitrogen points toward the surface, the material has Ga polarity (or Al or In), otherwise it is N polarity. Figure 1.2 shows these two situations for GaN.

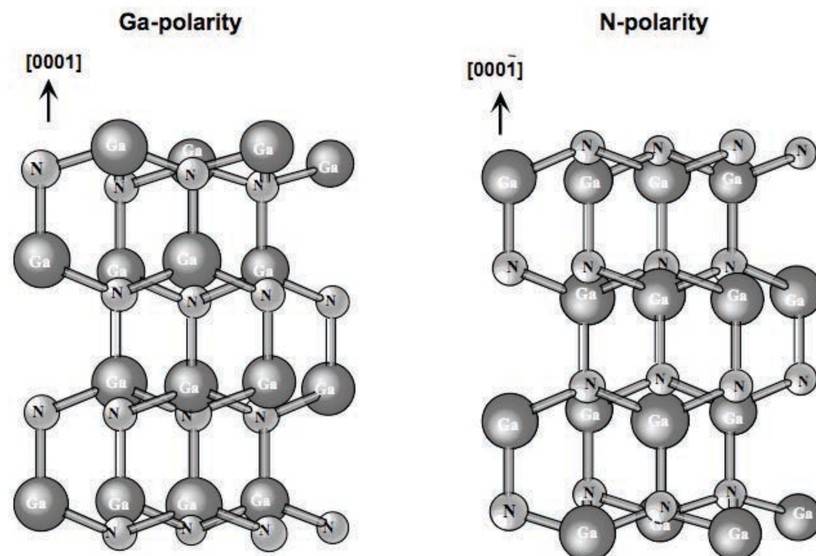

Figure 1.2 Ga-face and N-face polarities in a wurtzite GaN structure.

The deviation of the GaN unit cell from the ideal hexagonal wurtzite geometry and the strong ionic character of

the III-N bond are the origins of polarization properties of wurtzite III-N semiconductors. The total polarization in the crystal in the absence of external fields is the sum of spontaneous and piezoelectric polarizations. Spontaneous polarization originates from the fact that the barycentre of positive charges does not superpose with the barycentre of negative charges. This leads to the formation of dipoles in each cell which add to each other through the crystal to give a total macroscopic polarization vector which, Due to the crystal symmetry the polarization is aligned along the [0001] direction, with the positive direction pointing parallel to the [0001]-axis. In Ga-polar GaN films the spontaneous field points towards the surface plane of the film (Bernardini, 1997). The spontaneous polarization constants (p_{sp}) for binary III-N materials according to Bernardini, are shown in Table 1.2.

Parameter (C/m^2)	GaN	InN	AlN
p_{sp}	-0.029	-0.032	-0.081
e_{31}	-0.49	-0.57	-0.60
e_{33}	0.73	0.97	1.56

Table 1.2. Spontaneous polarization (psp) and piezoelectric constants (e_{31} and e_{33}) of group-III nitrides.

The piezoelectric polarization is caused by a strain induced deformation of lattice parameters a, c and u. In hexagonal wurtzite lattice the piezoelectric polarization p_{pe} along the [0001]-axis depends on two independent piezoelectric coefficients e_{31} and e_{33} as:

$$\delta p_{pe} = e_{33}\frac{c-c_0}{c_0} + 2e_{31}\frac{a-a_0}{a_0}$$

where a (a_0) and c (c_0) are the values of the lattice parameters under deformation (in equilibrium). The equation omits the polarization caused by shear strain, as it is not present in epitaxial structures. From the equation it can be shown that in epitaxial III-N layers under tensile strain in the basal plane the polarization is always negative,

and in layers under compressive strain the polarization is positive.

Heterostructures

In heterostructures, where layers of different materials are stacked, a discontinuity in the polarization vectors appears at each interface between the different compounds. This polarization discontinuity leads to the formation of surface charges bound to the interfaces (figure 1.3a); the total charge is proportional to the difference of the polarization in the two layers: $\sigma = \vec{n}\left(\vec{P}_a - \vec{P}_b\right)$ This surface-charge is negative for a heterojunction AlN/GaN and positive for a heterojunction GaN/AlN. Figure 1.3b shows the orientation of the electric polarization in four different cases: GaN and AlN strain-free configuration, strain-compensation configuration, strained AlN and relaxed GaN, strained GaN and relaxed AlN.

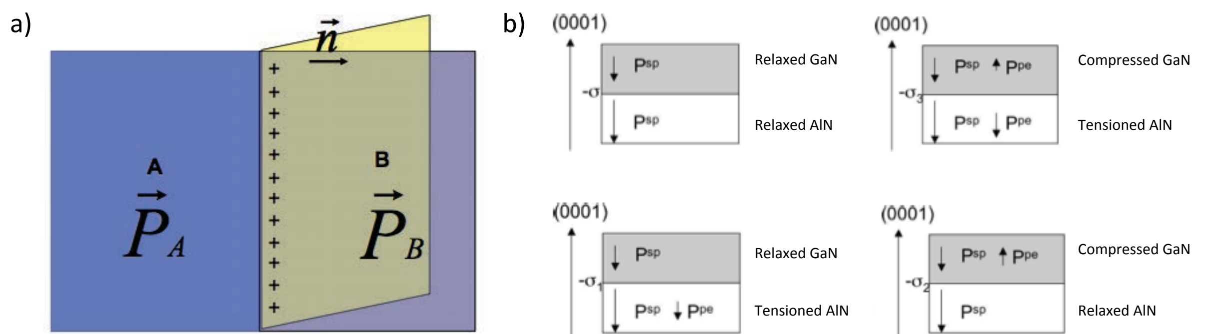

Figure 1.3 a) Interface surface charge due to polarization discontinuity. b) Spontaneous and piezoelectric polarization in AlN/GaN heterojunctions for different strain configurations.

1.4 Electronic properties

In crystals the periodic arrangement of atoms modifies the single atom energy states into energy bands. These energy bands govern the movement of electrons in the crystal. In semiconductors there exists an energy band gap between energy bands. In this energy band configuration the higher energy band is called the conduction band, and the lower energy band -- the valence band. In direct band gap semiconductors the conduction band

minimum (CBM) is located at the same electron wave vector (k) value as the valence band maximum (VBM). Direct band gap semiconductors are especially important for optoelectronic applications since radiative transitions from CBM to VBM have a much higher probability than in indirect band gap semiconductors.

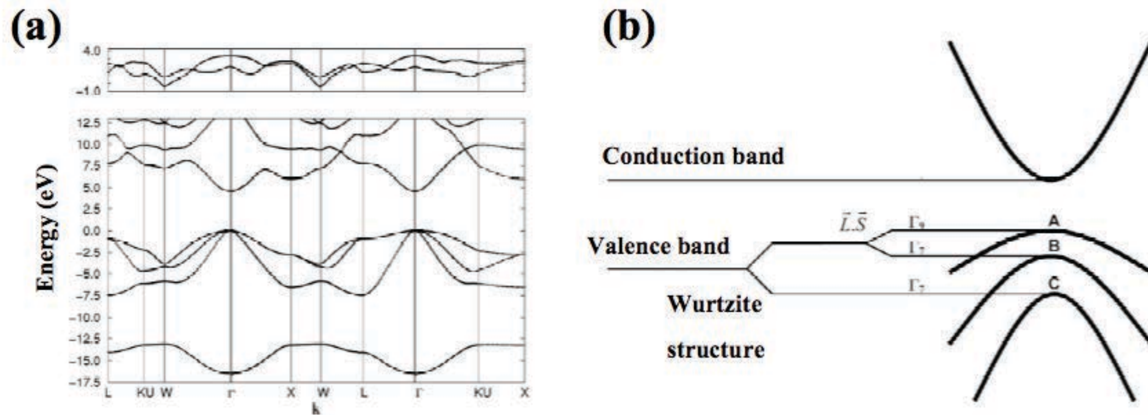

Figure 1.4 Calculated GaN band structure (I. N. Remediakis et E. Kaxiras). (b) GaN band structure near k=0 (Γ point).

The GaN band structure calculated by I. N. Remediakis and E. Kaxiras (Remediakis & Kaxiras, 1999) is presented in Figure I.4 (a) and a schematic representation of the energy bands around the Γ point is presented in Figure 1.4 (b).The conduction band originates from the coupling of s type antibonding orbitals, while the valence band originates from p type bonding orbitals. As shown in figure 1.4b, the conduction band is unique and has the Γ_7 symmetry, while the valence band is splitted in three bands due to the interaction with the crystal field because of spin- orbit coupling. These three bands are called A, B and C and are of Γ_9, Γ_7 and Γ_7 symmetries, respectively. They are also called “heavy hole”, “light hole” and “spin-orbit” bands, respectively. To each of the valence bands is associated an exciton (A, B or C), which consists in the quasi particle formed by an electron in the conduction band bound by Coulomb interaction to a hole in the considered valence band.

The major technological advantage of the III-N material system is that by alloying GaN with InN and AlN the band gap of the ternary or quaternary alloy can be tuned in a controllable fashion. Figure. 1.5 shows the band gap versus the lattice parameter a of different III-V semiconductors including the III-N materials. In principle the band

gap of III-N alloys can be varied continuously from 6.2 eV (pure AlN) to 0.7 eV (pure InN). Until recently the commonly quoted value for the optical band gap of InN was 1.89 eV, but new measurements have shown evidence of a much smaller band gap between 0.65 and 0.9 eV [18–20, and Publ. I]. The energy range from 6.2 eV to 0.7 eV covers the spectral range from deep UV to infrared. However, it is difficult to exploit the whole composition range in practice. Indeed, as the In or Al content of InGaN and AlGaN films is increased the growth of high quality material becomes more difficult due to the different optimum growth conditions of In and Al containing III-N alloys (S. Keller, 2003).

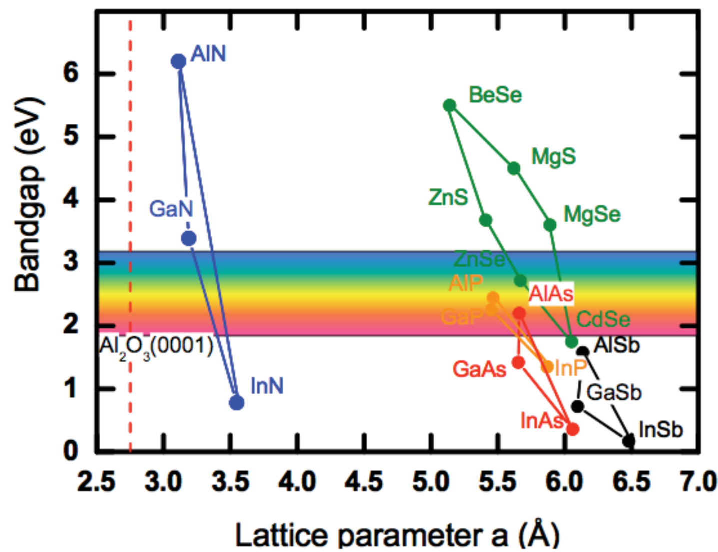

Figure 1.5. Bandgap energy as a function of in-plane lattice parameter for different semiconductor compounds.

In ternary and quaternary compounds the change of the band gap energy with composition can be described by linear interpolation with the inclusion of a bowing parameter b. The bowing parameter represents the magnitude of the second order correction to the linear dependence. The bandgap of a typical ternary III–nitride alloy, Ax B1-x N, can be expressed by the following formula:

$$E_g^{A_xB_{1-x}N}(x) = (1-x)E_g^{AN} + xE_g^{BN} - x(1-x)b$$

The variation of the band gap with temperature is given by the Varshni's law (Varshni, 1967).

$$E_g(T) = E_g(0) - \frac{\alpha T^2}{\beta + T}$$

$E_g(0)$ is the band gap energy at 0 K. The parameters α and β are tabulated in table 1.5, taking into account the electron-phonon interaction. As shown in Table 1.5, the bandgap reduction (red shift) between 0 K and 300 K is about -68, -66, -96 meV for GaN, InN and AlN respectively.

	$E_g(0)$ [eV]	α [meV/K]	β [K]	$E_g(300K)$ [eV]	Reference
GaN	3.489	0.887	874	3.421	[Leroux99]
AnN	0.69	0.414	454	0.641	[Walukievicz04]
AlN	6.126	1.799	1462	6.03	[Guo9]

Table 1.5 : Tabulated values for Eg(0) and Varshni's parameters (α and β) specifying the calculated band gap at RT

1.5 Nanowire Epitaxy

The performance and reliability of semiconductor devices strongly depends on the material quality. Therefore, a high degree of crystallinity is required and the defects should be avoided (or at least controlled). The most difficult problem faced by nitride-based devices is the lack of a lattice-matched substrate. The most commonly used substrate is sapphire where the lattice mismatch with nitrides is 14% and has a thermal expansion coefficient that is almost twice as large of GaN. As a consequence, a large density of dislocations is present degrading the performance of light emitters and limiting the response of the detectors. The lattice mismatch between GaN and Si is even greater (17%), making the growth of high-quality nitride films on Si extremely challenging.

Nanowire (NW) epitaxy involves quasi-1D growth with a NW diameter < 100 nm. At this scale, many differences compared with bulk start to appear: surface energies make a significant contribution to the total energy of the structure, and strain and defect properties are different to those of bulk. Many NWs are reported to be ideal crystals, free of defects, and may crystallize in a structure different from the stable bulk phase. Moreover, NW epitaxy offers greater freedom in the design of complex structures compared with planar epitaxy.

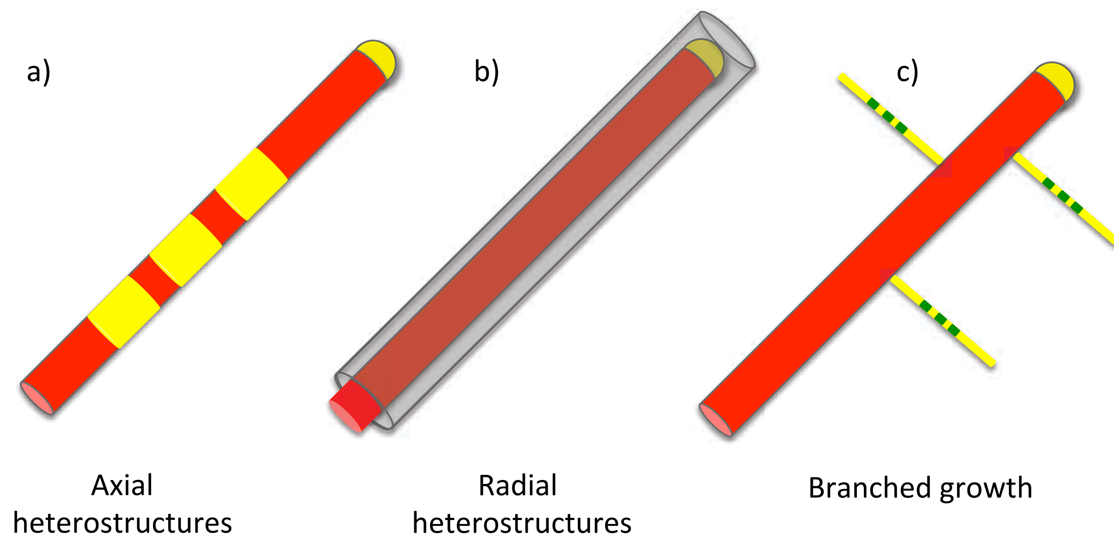

Figure 1.6 NW heterostructures and growth modes.

In Figure 1.6 three different NW structures are shown. Heterostructures, axial (a) and radial (b), are crucial for many devices. For the axial heterostructures, the NW geometry offers the possibility of new material combinations due to its small cross-section. A third type of structures, a branched NW, is shown in panel (c). From these three basic structures, more advanced building blocks can be formed, illustrating the flexibility of NW epitaxy.

Molecular beam epitaxy (MBE) and metalorganic chemical vapour deposition (MOCVD) are the most explored synthetic methods for the growth of semiconductor nanowires. These methods usually use small particles of a foreign material to assist the nanowire growth. This particular growth method is also called catalytic growth and depending on the phase of the particle (liquid or solid phase), the catalytic growth follows either the vapor-liquid-solid (VLS) or the vapor-solid-solid (VSS) mechanism.

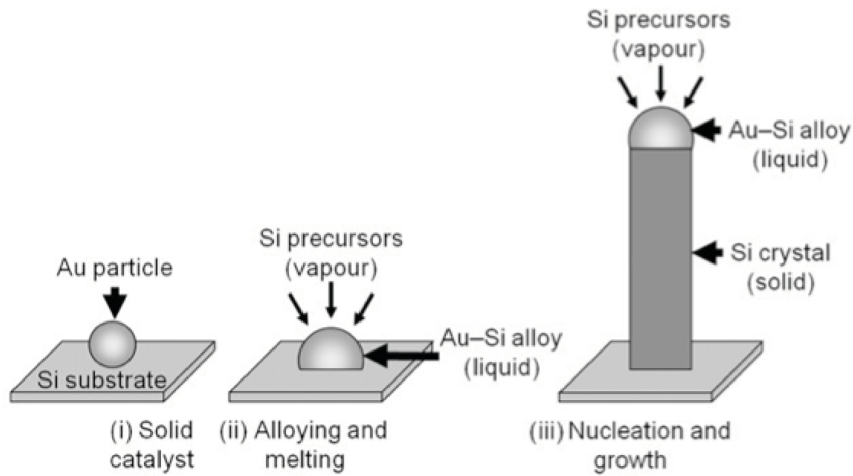

Figure 1.7 Schematic illustration of the VLS growth of Si wires using an Au catalyst particle. The grey arrow, and labels (i), (ii) and (iii) illustrate the different stages of nanowire growth

Particle-Assisted Growth

Wagner and Ellis proposed the VLS mechanism in order to explain the anisotropic growth of silicon nanowires (Wagner & Ellis, 1964). VLS mechanism is based on the properties of the gold-silicon phase diagram, and the concept of a liquid gold droplet that becomes supersaturated with Si supplied by the gas phase (figure 1.7). As the drop becomes super-saturated, Si will precipitate in solid form at the liquid/solid interface, and crystal growth will take place selectively under the Au particle. Hiruma further explored Au-assisted growth of III-V nanowhiskers in the 1990s (Hiruma et al., 1995) and at the end of the 1990s and beginning of 2000, several groups initiated work on NW synthesis employing gold particles. For III–V nanowires, this Au-assisted nanowire growth mechanism is suitable to a number of standard growth systems such as laser-assisted catalytic growth, MBE, chemical beam epitaxy (CBE), and MOCVD.

Particle-Free Growth

Foreign metal catalysts are widely used to direct the orientation and control the size of NWs, and they are intensively studied and well understood. However, contamination from catalysts and the limited selection of morphologies are the main drawbacks of the foreign-metal-catalyzed growth of NWs. Alternatively, NWs can be synthesized without using any foreign catalysts via a vapor deposition process. This offers a high lattice purity that is beneficial in many ways, such as eliminating unintentional doping and avoiding the effect of transition metals. Though this strategy has been widely used in NW synthesis, the growth mechanisms are less understood than those of metal-catalyzed NW growth. Typically, it is recognized that NWs are formed either directly from the vapor phase through a vapor-solid (VS) process or from an excess of metal adatoms through a self-catalyzed process.

Nanowire Growth of III-Vs on Si

Integration of III-V semiconductors on silicon is a field of great importance, as Si will probably remain the preferred platform for many applications for several reasons: it is available as large area wafers of extremely high purity and crystal quality, the material has good mechanical stability, it is an extremely well-characterized material, and simply because immense investments have been made in Si technology. A union between III-V and Si materials could provide standard CMOS devices with new functionalities.

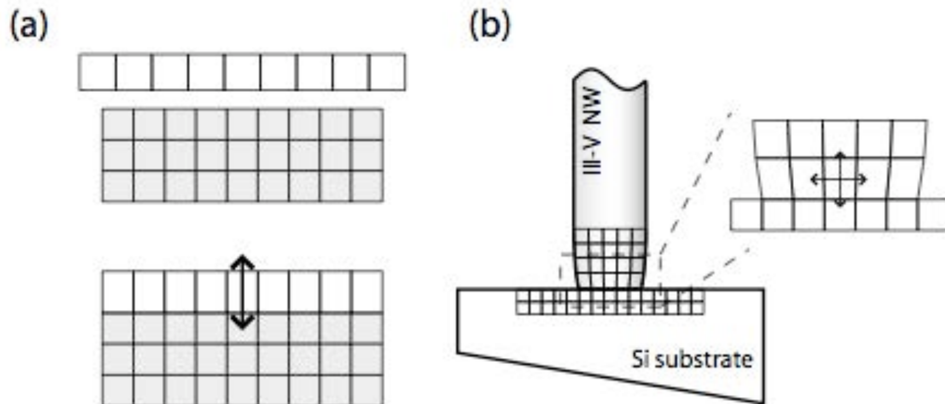

Figure 1.8 Illustration of the Si/III-Vinterface. (a) Planar growth for normal heterointerface, strain can only be relaxed along one dimension. (b) NW growth, strain can be relaxed laterally, allowing 3D strain relaxation.

However, achieving high quality growth of III-V semiconductor (and in particular III-nitride) thin films on Si is a difficult task to accomplish. The mismatch problem has less consequences on the crystal quality in nanostructures because of their small diameter allowing strain to be relaxed laterally figure (1.8 b) in contrast with the planar growth where strain can only be relaxed along one dimension (figure 1.8 a). Indeed, defect free GaN nanowire growth has been demonstrated on highly mismatched substrate such as sapphire (Yoshizawa et al. 1997), (Sekiguchi, Kishino, and Kikuchi 2008), and also low-cost substrates: Si(111) (E Calleja et al. 1999), (Tchernycheva et al. 2007) and Si(001) (Cerutti et al. 2006).

Selective area growth

Many applications of NW technology require exact position control of the NWs. There are two major means to achieve this. One option is post-growth assembly, where the NWs are removed from their original growth location and transferred for subsequent experiments or device fabrication. Several methods have been proposed to achieve this goal, for example, micromanipulation (Mølhave, 2006), Langmuir-Blodgett assembly (Whang, 2003) and random transfer with subsequent identification by a coordinate grid. However, a vertical geometry is preferred for many applications such as NW wrap-around gate FETs, LEDs and photonic crystals. To achieve organized

NW growth, the e-beam lithography can either be used to define the position of the growth seed particles, or to open up areas in a growth mask where the NWs grow particle-free (Motohisa, 2004). Mårtensson et al. reported a method to synthetized large InP nanowire arrays. The process starts with the definition of the apertures over the substrate by EBL, an Au layer (ranging from 17 to 45nm) is deposed via thermal evaporation then a liftoff is carried out. Finally the sample is transferred to a MOVPE chamber to perform the growth. Figure 1.9 shows an array consisting of hexagonal unit cells with a pitch of 250 nm.

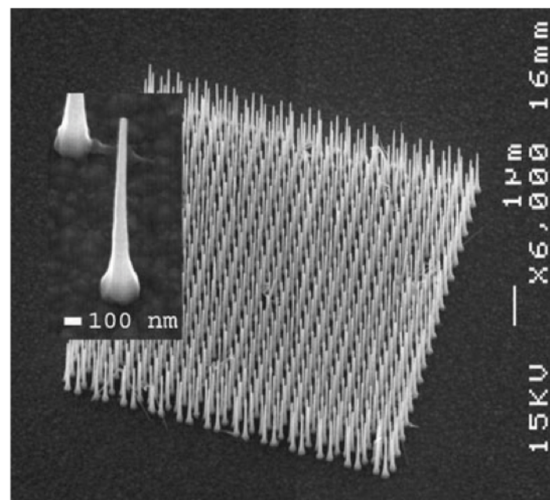

Figure 1.9 A high-density array of thin wires. The wires have a length of 3 μm and a top diameter of 50 nm while the base is thicker.

1.6 Applications

III-nitride nanowires have emerged as promising candidates for future nanoelectronic and nanophotonic devices. With the use of such nanoscale structures, nanoscale photodetectors, LEDs, lasers, and solar cells have been demonstrated. In what follows, I present a brief review of the fabrication and performance characteristics of some of such novel devices.

Photodetectors

It is well known that the presence of surfaces states in bulk semiconductors produces the so-called Fermi energy pinning causing a band bending (Garrido,1998). This phenomenon is also present in nanowires. Due to the large

surface-to-volume ratio, the effect of the surface states on the transport, optical and photoconduction properties in NWs is strongly enhanced with respect to planar structures. Surfaces states give rise to a surface space-charge layers creating a band bending of the conduction and valence band upward at the surface of the NW leading to a spatial separation of charge carriers where electrons tend to remain in the inward part of the wire while holes move to the surface. Calarco et al. show that depending on wire thickness depleted wires or wires with thin conducting channels are formed. If the wire diameter is smaller than a critical diameter (which depends of the depletion space layer, and in the case of nominally undoped GaN Is around 50-100nm) the NW will be totally depleted whereas for NWs with diameter above the critical diameter a channel for electrons is created as shown in figure 1.10a.

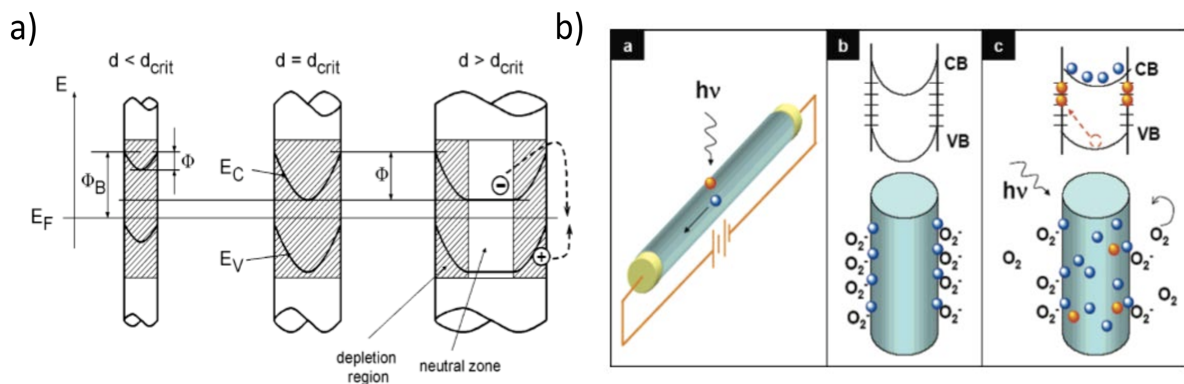

Figure 1.10 a) Dependence of the depletion region on the nanowire diameter. b) Trapping and photoconduction mechanism in ZnO nanowires.

Soci et al. reported a photoconductivity gain in ZnO nanowires as high as G~ 10^8. High photosensitivity due to high photoconductive gain has also been observed in m-axial GaN by R.-S. Chen et al.. The photoconduction mechanism that leads to such values can be explained as follows: Upon illumination electron-hole pairs are photogenerated, holes migrate to the surface (where they get trapped by the surface states) while electrons are held at the central part of the wire (figure 1.1ab). As a consequence of this spatial separation, recombination time is increased, as electrons would have to surpass the conduction band barrier at the surface for recombination. Electrons will thus make more transits trough the NW between contacts before recombining leading to an

enhancement of the photoconductive gain. In addition, the trapped holes modify the electrostatic potential and change the width of the conducting channel in the NW changing in turn the NW resistivity.

This studies indicates that the one dimensional geometry of NW photoconductors can yield a photoconductive gain at least three orders of magnitude larger than their thin films counterparts, as a result of the long photocarrier life times.

LEDs

The use of nanowires for LEDs offers significant improvements in comparison to conventional planar LEDs including high light extraction efficiency and compatibility with low cost substrates (Dick et al., 2005). In addition, defect densities and piezoelectric polarization fields in Ga(In)N nanowire heterostructures can be reduced due to the effective lateral stress relaxation as mentioned before.

Qian *et al* show that emission characteristics of nanowire LEDs can be further engineered by using core-multi-shell InGaN/GaN nanowire heterostructures. The LED structure consists of a triangular shaped n-doped GaN nanowires grown by catalyst- assisted MOCVD used as a template for the deposition of an InGaN/GaN/p-AlGaN/p-GaN shell structure (figure 1.11a). As shown in figure 1.1b the peak emission wavelengths in the range of 367 – 577 nm, were obtained by varying the indium compositions from 1% to 40%. The estimated quantum efficiencies are in the range of 3.9 to 4.8%.

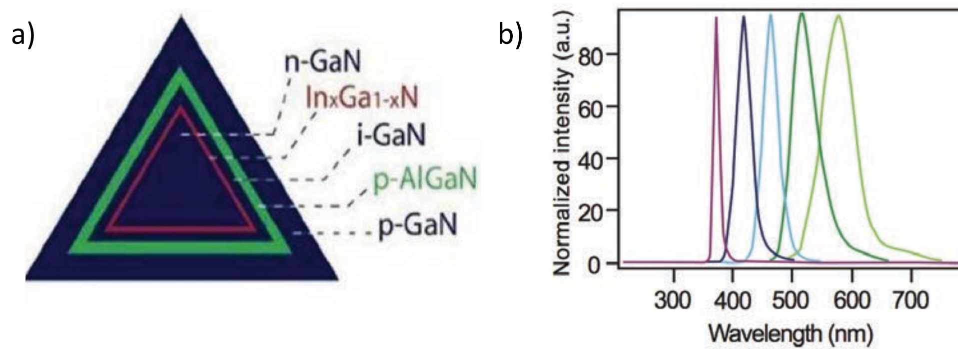

Figure 1.11 a) Schematic view of single nanowire LED structures. b) Normalized EL spectra recorded from five representative forward-biased multicolour core-multi-shell nanowire LEDs.

Green and white LEDs based on n-GaN/InGaN/p-GaN vertical nanowires grown on Si (001) substrates have been proposed by Guo, et al. PL measurements show that the emission of the nanowires can be tuned from UV to red

by varying the In composition. Nanowire LEDs were fabricated in forms of mesa (600µm x 600µm), NWs were planarized with parylene-insulated layer and cover with a transparent layer of Ni/Au to achieve top ohmic contacts on p-GaN nanowire. Electroluminescence measurements show that the emission peak centered at 520nm remains invariant in wavelength with increasing current injection.

Photovoltaic devices

Tang et al. demonstrated solar cells based on heterojunction formed by vertical p-doped GaN nanowires and n-doped silicon (111) substrate, shown schematically in Fig.1.12a with the corresponding energy diagram. The fabrication process is simple: first nanowires are covered with a transparent insulating layer of PMMA, followed by a thin metallic layer (Ni/Au) on the top of the wires, a second metallization (Ti/Au) on the backside of the Si substrate is also performed. As shown in Fig. 1.12(b), a well- defined diode behaviour with a rectifying ratio of more than 10^4 at ± 0.5 V in the dark, a short-circuit photocurrent density of 7.6 mA/cm^2, and a maximum power conversion efficiency of 2.73% under simulated AM 1.5G illumination at 1 Sun was achieved.

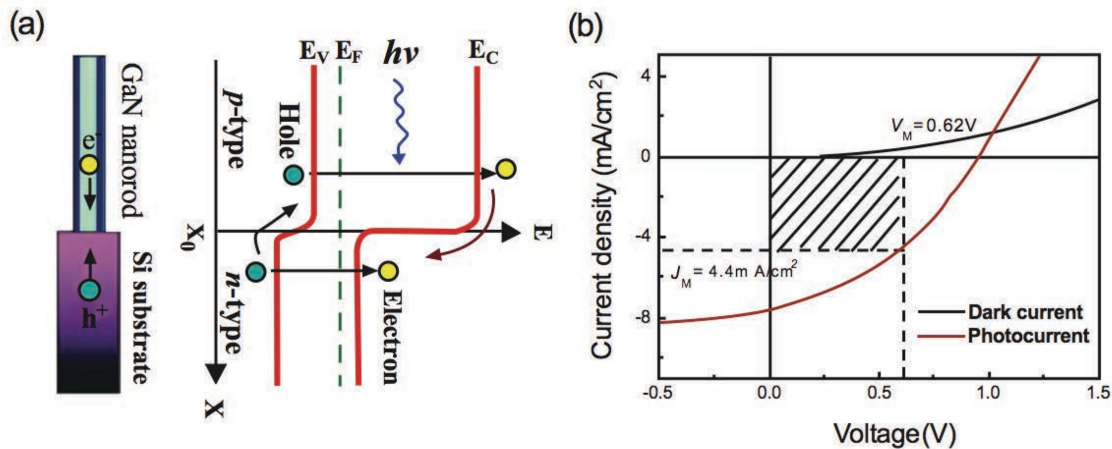

Figure 1.12 (a) Schematic energy band diagram of the solar cell heterojunction diode showing the photogenerated carrier transfer process. (b) Current density vs. voltage for the solar cell in the dark and under simulated AM1.5G illumination with an intensity of 100 mW/cm^2.

Dong et al. show that it is possible to tune the bandgap from 2.25 to 3.34 eV of single wire core shell n-GaN/i-InxGa1-xN/p-GaN structure by varying the In content in the InGaN active layer. Furthermore, open-circuit voltages

of 1.0-2.0 V and short-circuit current densities of 0.39-0.059 mA/cm^2 were achieved as the In composition was reduced from 0.27 to 0, with a maximum efficiency of ~ 0.19%. The main advantage of such core-shell-shell design is the effective carrier separation in the radial direction due to the p-i-n interface extension along the entire length of the nanowire. As a result, photogenerated carriers are able to reach the p-i-n junction with enhanced efficiencies due to a relatively short diffusion length required. The main drawback of this device is the complexity of the fabrication process due to the numerous lithography and etching steps.

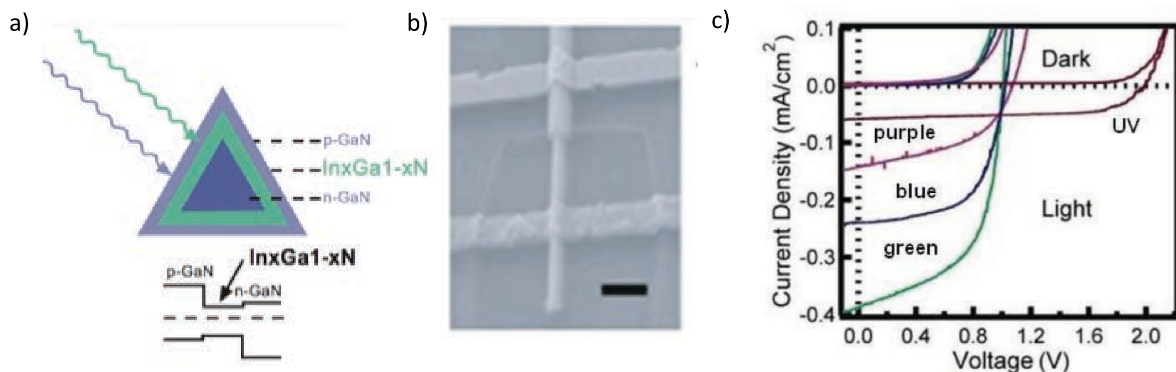

Figure 1.13 a) Schematic cross-section of n-GaN/InGaN/p-GaN core/shell nanowires and corresponding band diagram. b) Electrical contact schematic and corresponding SEM image. c) I-V curve for nanowires with different indium concentrations with and without illumination

Lasers

Chu et al. demonstrated the first electrically pumped laser diode based on ZnO nanowires. The structure consists of a homojunction of a high quality n-type layer growth by MBE and Sb-doped p-type nanowires growth by CVD encapsulated in poly-methyl-methacrylate (PMMA) etch in the tip of the nanowires and covered by an ITO layer as a top contact (figure 1.14a). Lasing action was achieved at threshold of ~ 50mA, with sharp emission lines as narrow as 0.5nm around 385nm. Figure 1.14b show that the light emission emerges from the top of the wires at high current injection.

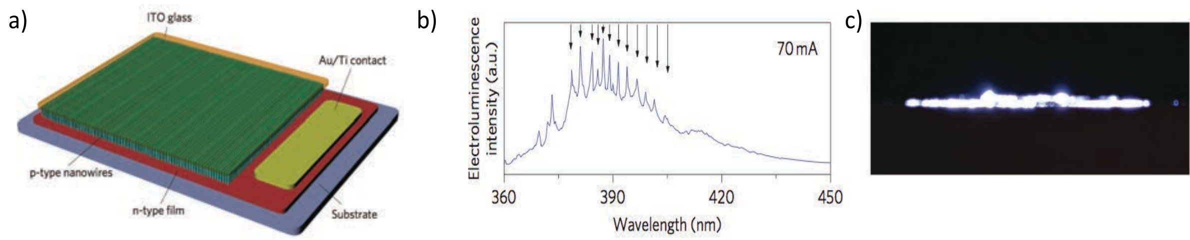

Figure 1.14 a) Schematic of the laser device, which consists of an n-type ZnO thin film on a c-sapphire substrate, p-type vertically aligned ZnO nanowires, ITO contact and Au/Ti contact. b) Electroluminescence spectra of the laser device at 70mA, arrows in the spectrum represent quasi-equidistant peaks. c) Side-view optical microscope images of the lasing device

Single nanowire lasers under optical injection have been realized using InGaN/GaN MQW core-shell nanowire heterostructures by Qian et al. The GaN core wire was grown by catalyst-assisted MOVPE growth resulting in a triangular cross section, followed by a multiple (n=26) InGaN/GaN MQW active layer (figure 1.15a) . The lasing wavelengths are at ~ 383, 420, 452, and 478 nm, depending on the In compositions. PL spectra measured at ~ 250 kW cm^{-2} and 700 kW cm^{-2}, below and above threshold, respectively for nanowire lasers are shown in figure 1.15b.

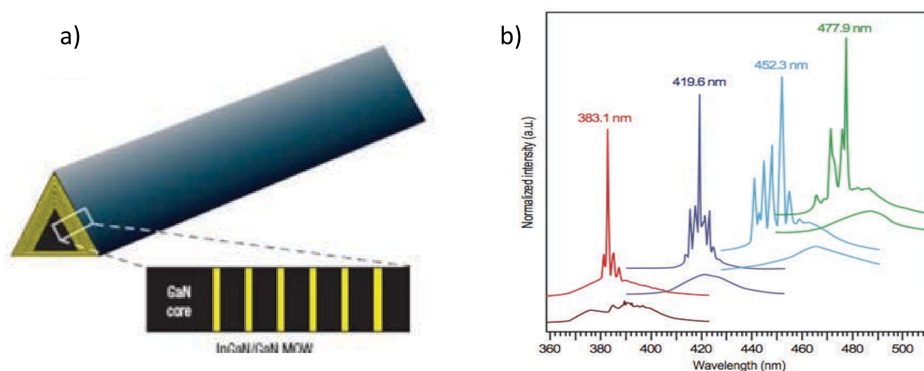

Figure 1.15 a) Schematic view of a GaN/InGaN MQW system embedded in a triangular nanowire. b) Normalized PL spectra collected from four representative 26 MQW nanowire structures with increasing In composition.

Bibliography

Bernardini, F., Fiorentini, V., & Vanderbilt, D. (1997). Spontaneous polarization and piezoelectric constants of III-V nitrides. *Physical Review B*, *56*(16), R10024-R10027. doi:10.1103/PhysRevB.56.R10024

Calarco, R., Marso, M., Richter, T., Aykanat, A. I., Meijers, R., V D Hart, A., Stoica, T., et al. (2005). Size-dependent photoconductivity in MBE-grown GaN-nanowires. *Nano letters*, *5*(5), 981-4. doi:10.1021/nl0500306

Chen, R.-S., Chen, H.-Y., Lu, C.-Y., Chen, K.-H., Chen, C.-P., Chen, L.-C., & Yang, Y.-J. (2007). Ultrahigh photocurrent gain in m-axial GaN nanowires. *Applied Physics Letters*, *91*(22), 223106. doi:10.1063/1.2817595

Chu, S., Wang, G., Zhou, W., Lin, Y., Chernyak, L., Zhao, J., Kong, J., et al. (2011). Electrically pumped waveguide lasing from ZnO nanowires. *Nature Nanotechnology*, *6*(July), 4-8. doi:10.1038/NNANO.2011.97

Dick, K. A., Deppert, K., Karlsson, L. S., Wallenberg, L. R., Samuelson, L., & Seifert, W. (2005). A New Understanding of Au-Assisted Growth of III-V Semiconductor Nanowires. *Advanced Functional Materials*, *15*(10), 1603-1610. doi:10.1002/adfm.200500157

Dong, Y., Tian, B., Kempa, T. J., & Lieber, C. M. (2009). Coaxial group III-nitride nanowire photovoltaics. *Nano letters*, *9*(5), 2183-7. American Chemical Society. doi:10.1021/nl900858v

Garrido, J. a, Monroy, E., Izpura, I., & Muñoz, E. (1998). Photoconductive gain modelling of GaN photodetectors. *Semiconductor Science and Technology*, *13*(6), 563-568. doi:10.1088/0268-1242/13/6/005

Guo, W., Zhang, M., Banerjee, A., & Bhattacharya, P. (2010). Catalyst-free InGaN/GaN nanowire light emitting diodes grown on (001) silicon by molecular beam epitaxy. *Nano letters*, *10*(9), 3355-9. doi:10.1021/nl101027x

Hiruma, K., Yazawa, M., Katsuyama, T., Ogawa, K., Haraguchi, K., Koguchi, M., & Kakibayashi, H. (1995). Growth and optical properties of nanometer-scale GaAs and InAs whiskers. *Journal of Applied Physics*, *77*(2), 447. doi:10.1063/1.359026

Motohisa, J., Noborisaka, J., Takeda, J., Inari, M., & Fukui, T. (2004). Catalyst-free selective-area MOVPE of semiconductor nanowires on (111)B oriented substrates. *Journal of Crystal Growth*, *272*(1-4), 180-185. doi:10.1016/j.jcrysgro.2004.08.118

Mårtensson, T., Carlberg, P., Borgström, M., Montelius, L., Seifert, W., & Samuelson, L. (2004). Nanowire Arrays Defined by Nanoimprint Lithography. *Nano Letters*, *4*(4), 699-702. American Chemical Society. doi:10.1021/nl035100s

Mølhave, K., Wich, T., Kortschack, A., & Bøggild, P. (2006). Pick-and-place nanomanipulation using microfabricated grippers. *Nanotechnology*, *17*(10), 2434-41. doi:10.1088/0957-4484/17/10/002

Qian, F., Hong-gyu, Dong, Y., Ding, Y., Li, Y. A. T., Cak, S. G., Wang, Z. L. I. N., et al. (2008). Multi-quantum-well nanowire heterostructures for wavelength-controlled lasers. *Materials Science*, 701-706. doi:10.1038/nmat2253

Remediakis, I., & Kaxiras, E. (1999). Band-structure calculations for semiconductors within generalized-density-functional theory. *Physical Review B*, *59*(8), 5536-5543. doi:10.1103/PhysRevB.59.5536

S. Keller and S. P. DenBaars. (2003). No Title. *J. Cryst. Growth*, 248.

Soci, C., Zhang, a, Xiang, B., Dayeh, S. a, Aplin, D. P. R., Park, J., Bao, X. Y., et al. (2007). ZnO nanowire UV photodetectors with high internal gain. *Nano letters*, *7*(4), 1003-9. doi:10.1021/nl070111x

Tang, Y. B., Chen, Z. H., Song, H. S., Lee, C. S., Cong, H. T., Cheng, H. M., Zhang, W. J., et al. (2008). Vertically aligned p-type single-crystalline GaN nanorod arrays on n-type Si for heterojunction photovoltaic cells. *Nano letters*, *8*(12), 4191-5. American Chemical Society. doi:10.1021/nl801728d

Varshni, Y. (1967). Temperature dependence of the energy gap in semiconductors. *Physica*, *34*(1), 149-154. doi:10.1016/0031-8914(67)90062-6

Vurgaftman, I., Meyer, J. R., & Ram-Mohan, L. R. (2001). Band parameters for III–V compound semiconductors and their alloys. *Journal of Applied Physics*, *89*(11), 5815. doi:10.1063/1.1368156

Wagner, R. S., & Ellis, W. C. (1964). VAPOR-LIQUID-SOLID MECHANISM OF SINGLE CRYSTAL GROWTH. *Applied Physics Letters*, *4*(5), 89. doi:10.1063/1.1753975

Weisstein, E. W. (n.d.). Solid State Physics -- from Eric Weisstein's World of Physics. Wolfram Research, Inc. Retrieved from http://scienceworld.wolfram.com/physics/SolidStatePhysics.html

Whang, D., Jin, S., Wu, Y., & Lieber, C. M. (2003). Large-Scale Hierarchical Organization of Nanowire Arrays for Integrated Nanosystems. *Nano Letters*, *3*(9), 1255-1259. doi:10.1021/nl0345062

2. Nanofabrication

The current chapter describes the technological processing to fabricate devices based on nanowire ensembles and single nanowires. The main techniques are the optical lithography and the electron beam lithography. A brief review of both techniques as well as of other processing issues and limitations is given. After a brief introduction, I describe the developed strategy to contact single nanowires by means of electron beam lithography. In particular, the influence of NW diameters on the contacting procedure is addressed. Finally, I discuss the fabrication of devices based on vertical nanowire ensembles using photolithographic techniques. The characteristics of such devices will be discussed in the following chapters.

Introduction

The term « nanofabrication » refers to the design and fabrication of devices having dimensions below 1 µm. Since the invention of the first transistor in 1947, the constant need to reduce the transistor size has been the driving force to push fabrication technologies to new dimensional limits. Following the so-called ‘‘Moore’s Law’’, the semiconductor industry was able to double the density of transistors on a unit area of silicon chip in every 18 months. Despite the fact that silicon has dominated the semiconductor industry, there is also an increasing demand for miniaturization in III-V semiconductor manufacturing. It is motivated by the need of exploiting the unique characteristics of these materials in large-scale integrated electronic and photonic devices.

Furthermore, there have been attempts to integrate the III-V materials on Si, in order to exploit the opto-electronic properties of III-Vs integrated on a CMOS platform. Nevertheless, the III-V thin film growth and technology has so far proven to be not CMOS-compatible, mainly due to the lattice mismatch between Si and III-Vs, which induces a significant amount of defects at the hetero-interface and would thus degrade the performance of the final device.

Nanofabrication finds applications in numerous fields such as nanoelectronics, nanophotonics, nanomechanics, nanomedicine, etc. requiring different materials and geometries (disks, rods, holes, pyramids, etc). The goal of nanoscience is to develop reliable ways to fabricate nanostructures, and also to achieve macroscopic systems from nanoscale components with dimensions in the submicron range. The nanofabrication tools can be classified into two categories: (i) those that precisely engineer matter (etching and depositing) and (ii) those that define the shape of the elements to be engineered (patterning, mainly lithographic techniques).

In this context, optical photolithography is the most common technique to define pattern geometry due to its large scalability, easy processing, and low cost. However, the resolution for conventional sources is limited by the wavelength of light and the optical diffraction phenomena. The range of photon wavelengths used in current optical lithography systems is typically 193–436nm. In addition, photolithography depends on other techniques for the mask fabrication. In order to achieve high resolution, recent efforts have been focused on the development of extreme UV lithography (EUVL), but the main inconvenients are the expensive light sources, scarceness of transparent refractive optics and difficulty to achieve defect-free EUVL masks.

Electron beam lithography (EBL) is an alternative process to photolithography. It is a very precise and high-resolution method since electron wavelengths are much shorter than the wavelength of visible-UV photons. Modern EBL systems use high energy electrons (up to 100keV) which can be focused onto spots of several nanometers, which is typically about one order of magnitude smaller than the pattern size employed for the realization of single nanowire devices. No physical masks are needed, patterns can be designed and optimized using a CAD software. Nevertheless, exposure times can take several hours to cover small areas, making this process not efficient for industrial manufacturing. Another drawback is that the system has to be held in a vacuum making the e-beam equipment processing more complex and expensive. In conclusion, the choice between the e-beam lithography and the photolithography depends on final product, including shape, size, length, substrate, application. Both these nanofabrication tools will be used to develop nanowire devices as described in the following.

2.1 Fabrication of single nanowire devices

In this study, I have developed a nanofabrication process to produce devices based on single nanowires. Here, the description of the technological steps is presented. In general, the fabrication process of individual nanowires consist in the following steps:

i. *Substrate preparation*
ii. *Nanowire dispersion*
iii. *E-beam lithography*
iv. *Metallization*
v. *Lift-off*

First Si/SiO_2 substrate with alignment marks are prepared by e-beam lithography. The nanowires are then transferred from their growth substrate onto the Si/SiO_2 template using either a wet or a dry dispersion method, Nanowire positions are then registered and recorded into a CAD software where contact patterns are designed. Next, the e-beam lithography followed by a metallization is performed to define the contacts on the nanowires. Finally, the excess of metal is removed by a lift-off step.

2.1.1 Substrate Preparation

A substrate is a basic component of a nanoscale device, it provides a mechanical support and partly determines the dielectric environment of the device.

In this work, silicon wafers are used as device substrates because of their availability and their relatively low cost. The silicon (100) wafers covered by a silicon oxide insulating layer of about 300 nm have been either purchased or produced in our clean rooms by a thermal oxidation of Si wafers. The role of the SiO_2 layer is to provide a good insulation preventing current leakage from the nanowire and from the metal contacts to the silicon wafer.

The cleanness of the substrate is important to achieve reproducible electrical properties of the device. The silicon wafers are prepared in clean conditions by the manufacture, however, dust particles and other impurities may contaminate the substrate surface during wafer manipulation and fabrication steps. Chemical contaminants include grease from human contact and polymers left from the previous processing steps. Grease and polymer residue can interfere with the good adhesion of the deposited metal layers. Thus, before each fabrication step, the substrate surface must be cleaned in order to keep it dust- and impurity-free.

The standard cleaning procedure is as follows:

1. 5 minutes of ultrasonication in acetone
2. 5 minutes of ultrasonication in isopropyl alcohol (IPA)
3. Blow-drying in nitrogen gas

All the organic solvent cleaning is performed inside a fume hood. The first step is ultrasonication in acetone; this step is used to shake off the particulate contaminants from the substrate. A second ultrasonication step is carried out in isopropyl alcohol. The IPA step is used to remove any remaining contaminants including acetone traces. Although IPA is a weaker solvent than acetone, IPA itself doesn't leave any residue on the surface when it dries. When all the solvent cleaning is done, a nitrogen gun is used to dry the sample completely.

Once the substrates are clean and before nanowire dispersion, a first e-beam lithography step is performed to place alignment marks on the substrate. These marks serve as a reference frame for tracking the position and orientation of the nanowires. They have been designed to easily locate the nanowire and to precisely align the electron beam within one writing field. This point will be discussed later in this section.

2.1.2 Nanowire dispersion

GaN nanowires are usually grown on silicon or sapphire substrates. In order to process single nanowire devices, nanowires have to be removed from their native substrates. There are two different approaches to transfer nanowires to an appropriate substrate, i.e. by either dry or wet techniques. As a quick method one can use a dry

transfer method. In the dry transfer method, nanowires are collected from the growth substrate with a blade and brushed onto the SiO_2/Si substrate. However, the dry transfer method tends to deposit nanowires unevenly, often glued together in bundles and it does not allow for controlling the density of the deposited nanowires. In the wet transfer method, the nanowires are detached from the substrate by ultrasonic agitation in Ethanol. One or several drops of the resulting nanowire suspension are deposited to the Si/SiO_2 substrate. The wet transfer method allows for controlling the density of the deposited nanowires by changing the volume of the solvent or the number of drops deposited onto the Si/SiO_2 substrate.

2.1.3 Electron beam lithography

Electron beam lithography (EBL) is a very precise and high-resolution technique, for forming extremely fine patterns in a layer of material. In this work we developed a method based on EBL for writing contact electrodes on single nanowires using the Raith 150 electron-beam lithography system. The Raith 150 system is capable to control and place patterns with a resolution better than 50 nm making it well suited for contacting nanowires. We can contact a nanowire either by its extremities or deposit multiple contact electrodes within the length of a nanowire.

The EBL standard configuration uses a hardware like a scanning electron microscope (SEM). First, the sample surface is coated with a thin layer of polymer – an electron-sensitive resist. The focused electron beam is guided on the surface to form patterns in the resist. The result of this exposure is to render the resist either soluble (called a positive tone resist) or insoluble (negative tone resist) in an appropriate developer solution.

A typical electron beam lithography system is shown schematically in figure 2.1. It consists of an electron gun, an electron optical column, and a vacuum chamber containing an x/y stage for positioning the substrate under the beam.

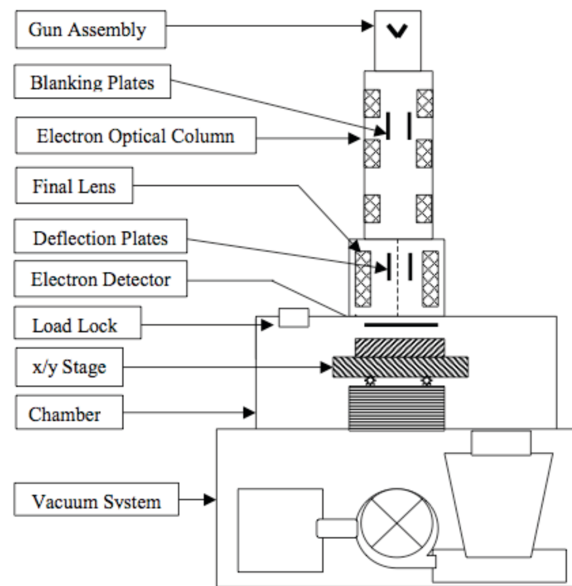

Fig. 2.1 Block diagram of a typical electron beam lithography tool.

The electron optical column is used to form and direct a focused beam of electrons onto the surface of the substrate, which is mounted on a holder and clamped to the stage. The electrons are produced in the uppermost section, which is called the electron source or gun. After the beam of electrons emerges from the gun it passes through several additional stages in the electron optical column that perform specific beam modification processes to produce a beam having the required current and spot size and correctly focused onto the substrate.

Even if EBL is capable to achieve very tiny patterns, when electrons penetrate a resist film and the substrate, they lose energy via elastic and inelastic collisions known as scattering. Electrons undergo both small-angle (inelastic or forward scatter) and large-angle (elastic or backscatter) scattering events, once they enter the resist and substrate (figure 2.2). The scattering process leads to a broadening of the beam; that is, electrons spread out while they penetrate into the solid. As a consequence, the energy is deposited within the resist layer in a region which is more extended than the cross section of the electron beam. These scattering processes have important consequences on the writing process. In particular, for adjacent patterns the exposure of one pattern contributes to the exposure of another located within the scattering range of electrons. This is known as “proximity effect”. Such phenomena impose certain restrictions of the size and shape of the relief structures that can be written in the resist, in particular for complex patterns with sub-micrometre dimensions. The total amount of energy deposited in a pattern feature depends on its size and the distance of neighbouring features. As size and space

pattern features change, proximity effects become more or less influential.

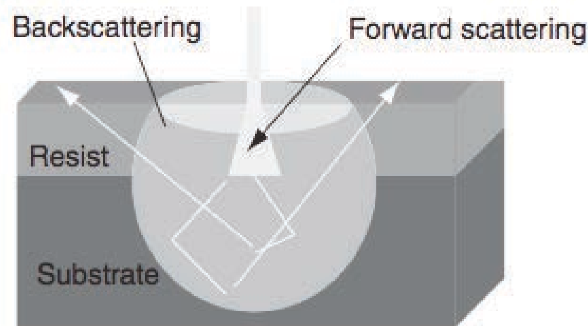

Figure 2.2 Illustration of the short-range (forward-scatter) and long-range (backscatter) interaction of electrons with resist-coated wafer

Dose calibration

As mentioned above, proximity effects are undesirable issues in EBL technique and they must be avoided. Many different schemes have been designed to minimize this drawback; the dose must be accurately calibrated before performing the lithography for single-nanowire device fabrication. In our case, to determine the optimal exposure parameters we used a method based on dose modulation. The method consists in writing a large number of identical patterns and progressively increasing the dose in each one of them. Patterns are based on different sizes, shapes and space between themes imitating the nanowire contacts. The initial dose is estimated from the resist datasheet provided by the manufacturer. The dose for the first pattern is deliberately set below the expected optimal value and the step by which the dose is increased for subsequent patterns is chosen small enough to determine the optimal value with a high precision. SEM observation after metallization and lift-off allows then for finding the optimal dose.

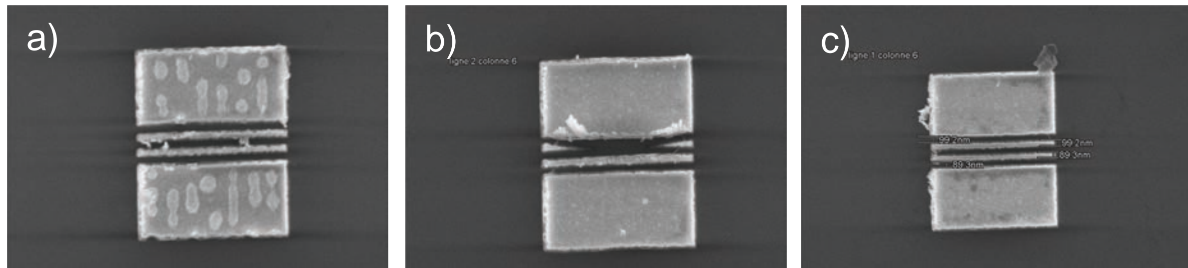

Figure 2.3 Dose modulation patterns. The surface state for a pattern a) which is not sufficiently exposed leaving "bubbles" on the exposed surface. b) which is exposed to an excessive dose resulting in an undesired variation of the patterns. c) which is exposed to an optimal dose. The pattern shape is well defined and the feature size corresponds to the mask design.

Lithography

Once the optimal dose is determined, it is possible to proceed to the lithography on single-nanowire devices. The step-by-step process of fabricating metal contacts on nanowires by electron beam lithography is shown in Figure 2.4. (a) The nanowire position with respect to the alignment marks is recorded. (b) The dedicated mask is designed using the Raith Software. (c) A layer of PMMA resist is spin-coated on the sample. (d) An electrode pattern is written by the electron beam. The resist is developed after exposer. (e) Metal is deposited. (f) The remaining resist is dissolved in acetone and only the metal electrode pattern remains after the lift-off process. (g) The chip is then wire bonded for measurements.

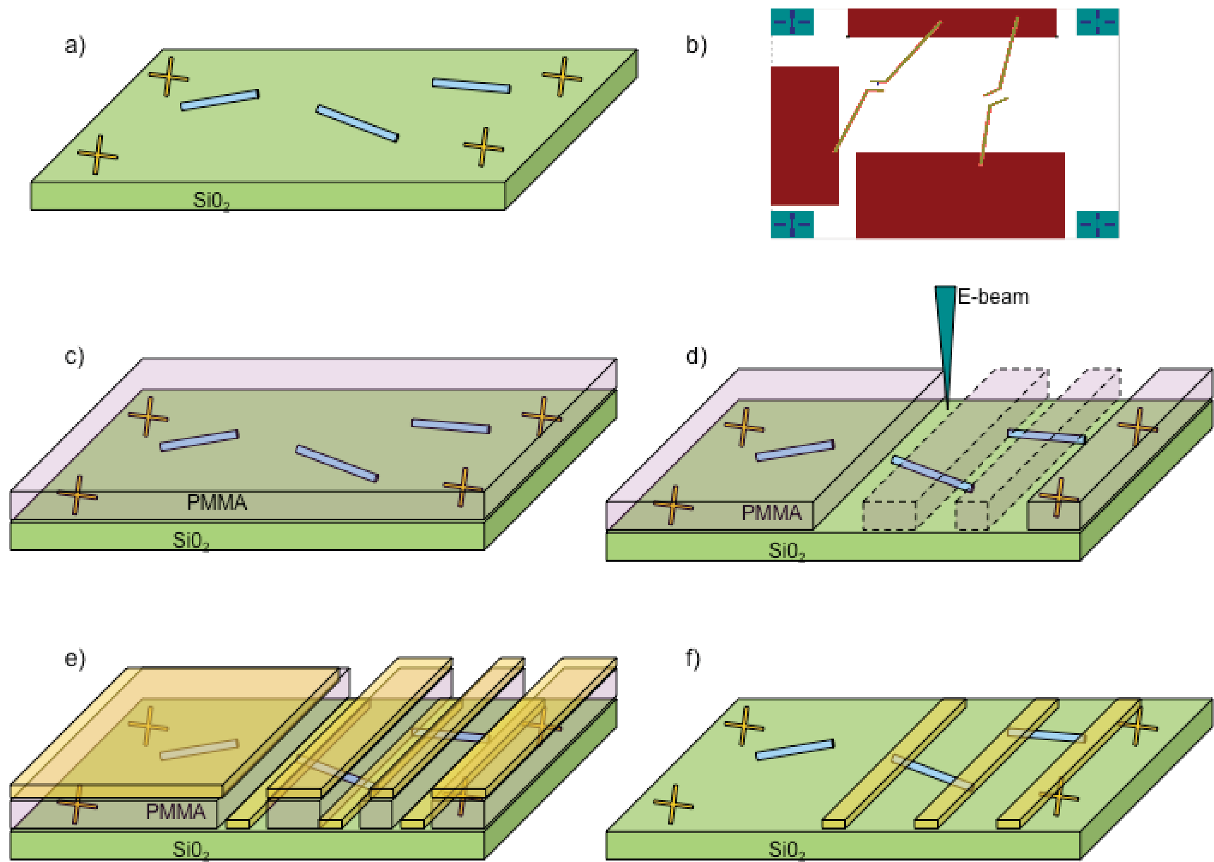

Figure 2.4 Schematic view of different fabrication stages.

Alignment marks

Alignment marks are required to locate the nanowires and to align the electron beam with a high precision. To facilitate the alignment procedure, I have chosen to use marks in the form of crosses of different sizes organized into a regular array. To allow for a rough alignment, large crosses are placed in the four corners of the global writing field with a spacing of 5 mm. Then, an array of smaller crosses with 100µm spacing is periodically repeated for each local write-field with a period of 500um. When dispersing the nanowire, we adjust the density in order to have a significant amount of wires present in each write field. One of the main advantages of the Raith 150 system is its SEM integrated system that facilitates the navigation all over the sample and the precise location of the nanowire positions.

Mask design

Nanowire positions are introduced into Raith 150 software, then a custom mask is designed to contact them. The intended pattern is created using a GDSII format layout-editor software. The typical contact width is between 100 nm and 400 nm and the spacing is between 100 nm and several microns depending on the nanowire length. We choose rectangular geometry for contacts as shown in Figs 2.6 and 2.7. One end of the contact strip covers the nanowire, while the other end is connected to the large area square contact used for macroscopic wire bonding. This latter contact can be either written using e-beam lithography with a large current or defined by optical lithography. Both strategies have been used depending on the desired application.

PMMA resist

After locating the position of the nanowires, a layer of e-beam resist is spin coated on top of the nanowires. We use Polymethyl methacrylate (PMMA A6) positive resist in this work. PMMA is a transparent polymer, which is electron-beam sensitive. When exposed to the electron beam, these complex macromolecules get broken down into simpler compounds, which can be easily dissolved in a chemical developer. The developer used is a cocktail of 3 parts IPA and 1 part methyl-isobutyl ketone (MIBK) by volume.

The contacting of nanowires with average diameters between 50 nm and 200 nm requires that the deposited metal thickness should be at least 25-100 nm to avoid discontinuities in the deposited metal electrodes. We use a recipe resulting in a 500 nm thick layer of PMMA A6 to allow for a lift-off process of metal deposition. The actual spin coating recipe is the following. Multiple drops of PMMA A6 solution are deposited on the surface until covering entirely the whole sample. The spinning rate is then set up to 4000 rpm, which is maintained for 60 seconds to uniformly coat the chip with a layer thickness of 500nm. After spinning, the sample is baked on a hot plate at 180ºC for 15 minutes to harden the PMMA layer.

E-beam writing

The Raith system utilizes the vector-scanning approach where the e-beam “jumps” from one patterned area to the next skipping over all non-patterned areas. This method of not visiting every point in the pattern makes the vector scan approach faster than raster scan for sparse patterns (figure 2.5a). Also, the vector-scan keeps the substrate stationary while the e-beam is deflected over the areas to be exposed. Mechanical vibrations may influence the writing accuracy. Even if the Raith has an anti-vibration system, samples were usually loaded 12 hours before the lithography in order to eliminate this issue.

Our write strategy consists to divide the entire sample into write fields. The maximum widths of one write field is around 800 um, however for large writing fields the precision is lower than for the small ones. As we are dealing with submicron contact features, a small writing area is desired so that the e-beam can cover it with good precision. For this reason I chose the write field size of 100um x 100um. As mentioned before, four cross-shaped alignment marks are present in each write field. After the writing of one field is finished, the stage is moved to the next write field etc (figure 2.5b).

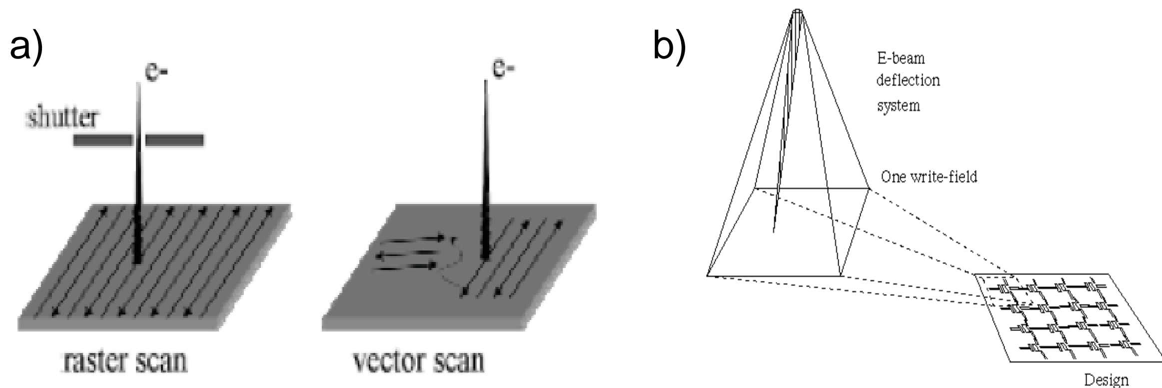

Figure 2.5 a) Comparison between raster and vector scan b) the e-beam is swept across the entire surface, write field by write field, the beam is blinked according to the pattern design.

For small beam displacements we have to calibrate the amount of beam deflection that we need in a given write field using the alignments marks. The strategy for calibration the dose is the following. We use the interferometer to drive the stage to the center of one write field, then, the computer scans a file containing the position center of

the four crosses. The resulting image is the position to what computer thinks the original spot is. Looking at the image, we correct the difference between where the beam thinks we are and where the actual original spot is, we repeat the same step for the four crosses positions; the computer will register the data in order to implement a correction for the beam deflection. In order to write a design larger than one write-field, which is often what is needed, it is necessary to write over several write-fields by putting several write-fields adjacent to each other. For accurate stitching, the sample stage is translated by a combination of servo-motors and piezo-electric actuators guided by the laser-interferometer.

Two step electron beam lithography

For applications in which two different metallizations are required, it is necessary to perform two steps of electron beam lithography. This was for instance the case for nanowire-based p-n junctions, for which two different ohmic contacts on p-GaN and on n-GaN were required. In this case the e-beam writing, metallization and lift-off are repeated twice. Figure 2.7 show a p-i-n nanowire structure (where the half of the NW side is n-type while the other half is p-type). The n- and p-type sides have been recognized by SEM observation thanks to the tapering of the nanowire, yielding a diameter on the p-type side larger than on the n-type side. This recognition process is crucial in order to achieve ohmic contacts on each side.

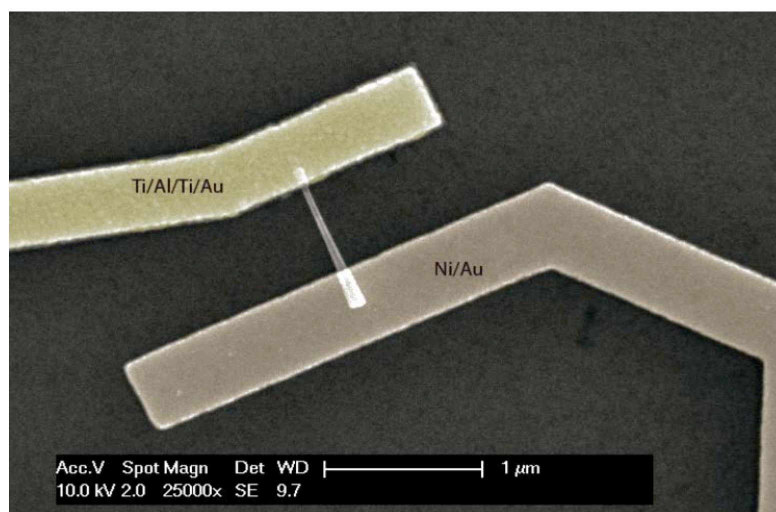

Figure 2.6 shows SEM image of a p-i-n GaN single nanowire contacted by two steps of e-beam lithography. Ti/Al/Ti/Au is deposited in the n-type region (yellow) while the p-type is covered by Ni/Au (brown).

2.1.4 Metallization

The metallization is the fabrication step in which electrical interconnects are formed by depositing selected metals. There are several methods of metallization such as thermal evaporation, magnetron sputtering and electron beam evaporation. We used e-beam evaporation; this method uses an electron beam with a high energy of 10 keV to evaporate a small spot of a source material in the crucible. In evaporation methods the pressure inside the evaporation chamber is about 10^{-6} or 10^{-7} Torr. At this low pressure, the mean free path of the evaporated atoms is of the same order of magnitude as the vacuum chamber dimensions, so these atoms travel in straight lines from the source to the substrate. The deposition is directional in opposition to sputtering technique, where a conformal coverage is obtained. The directional deposition is better adapted for lift-off process, which is one of the motivations of the choice of e-beam evaporation in this work.

Before the metal deposition, we use in-situ Ar plasma cleaning to remove residual resist beneath the contacts. The choice of the deposited metals is important for the contact resistance. For n-type GaN nanowires Ti/Au metals are sometimes used in the literature to form ohmic contact (Schmitz A.C. et al., 1996). However, the optimization of ohmic contacts performed on thin films has shown that much lower contact resistance can be achieved by employing a Ti/Al/Ti/Au metallization. In this case, Ti layer provides a thermally stable and low-resistive contact to GaN as well as a stick platform for the rest of layers. It also interacts with GaN to form TiN interface layer. TiN has a lower work function (3.74 eV) than Ti. Also, the formation of a thin TiN interfacial layer generates a nitrogen-deficient layer near the Ti/GaN interface. This phenomenon causes the GaN to be locally highly n-doped and improves the tunneling effect on the Ti/GaN interface. Al is the metal with the closest work function with n-type GaN which improves the contact resistance. A second layer of Ti plays the role of a capping layer in order to avoid Al oxidation and Al-Au intermixing. Finally, the Au layer is used to allow wire bonding. This metallization scheme, allows achieving contacts resistivity as low as 6.0×10^{-7} Ωcm^2 and $2.2.0 \times 10^{-5}$ Ωcm^2 for doping concentrations of 1.4×10^{20} cm^{-3} and 2.2×10^{18} respectively (Wang et al., 2001,)(Davydov et al., 2005).

Difficulties in achieving low-resistance ohmic contacts in p-type GaN are due to the poor carrier concentration and the absence of suitable metals with a higher work function than that of p-GaN. Ni/Au metal approach is one alterative solution to overcome this issue attaining resistivity values around 10^{-4} Ωcm^2 (Ho et al., 1999). When a thermal annealing is done under O_2 ambient the Ni diffuse to the contact surface to form NiO, resulting in the

contact structure of p-GaN/NiO/Au. The oxygen atoms incorporated during annealing promote out-diffusion of Ga atoms, producing Ga vacancies below the contact. Thus, the net hole concentration in the near-surface region increases and the surface Fermi level moves to the energy level of the Ga vacancy, leading to a drastic reduction in contact resistivity (Jang, S. Y. Kim, & J.-L. Lee, 2003).

2.1.5 Lift-off

The lift-off process removes the excess metal. The metal film on the PMMA resist is detached from the sample when the PMMA is dissolved in acetone. A thick layer of deposited metal can lead to difficulties in the lift-off process by forming a continuous metal layer across the developed area. Therefore, the metal thickness should be less than about 50% of the resist thickness to avoid a lift-off problem. To check that all the excess metal has been lifted-off, the chip can be controlled under an optical microscope. This has to be done while the sample is still wet, otherwise the excess metal will stick to the chip and won't come off. If all the excess metal has not been lifted-off, the chip can be soaked in acetone for longer time, rinsed with a syringe or put in an ultrasonication bath. However, with nanowires already present on the chip, we usually avoid using ultrasonication. When the lift-off of excess metal is completed, the sample is rinsed with isopropyl alcohol and blown dry with a nitrogen gun.

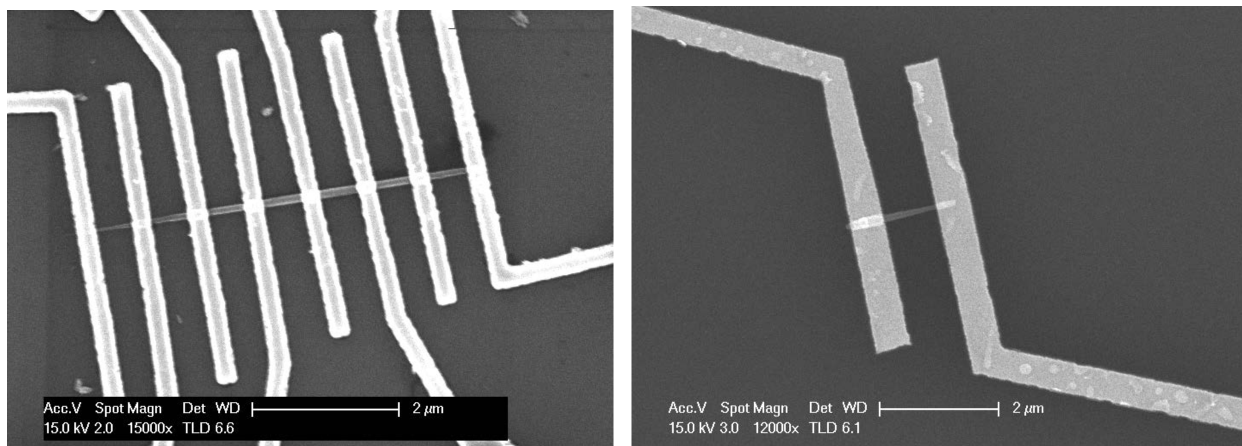

Figure 2.7 SEM images of nanowires after the whole technological process. a) Multi-contacts along an InP nanowire b) Double contact on a single GaN nanowire.

2.1.6 Contact annealing

For a good performance of photodetectors and light emitters, it is necessary to have ohmic contacts. Thanks to the Ar plasma cleaning, most of the metal contacts on the analyzed n-type GaN nanowires show ohmic behavior without any high temperature annealing step. Occasionally we used the Jipelec Jetfirst rapid thermal annealer to further reduce the contact resistivity. The annealing step for Ti/Al/Ti/Au contacts on n-GaN is done for 1 minute at 650°C in an argon-hydrogen gas atmosphere. For Ni/Au contacts to p-GaN annealing at 500°C during 5 min has been used.

2.2 Planarization

When contacting nanowire with diameters larger than the typical metal layer thickness, shadow effects appearing due to the directionality of the metal deposition can translate into a discontinuity of the deposited metal layer, as shown in Figure 2.8 a & b.

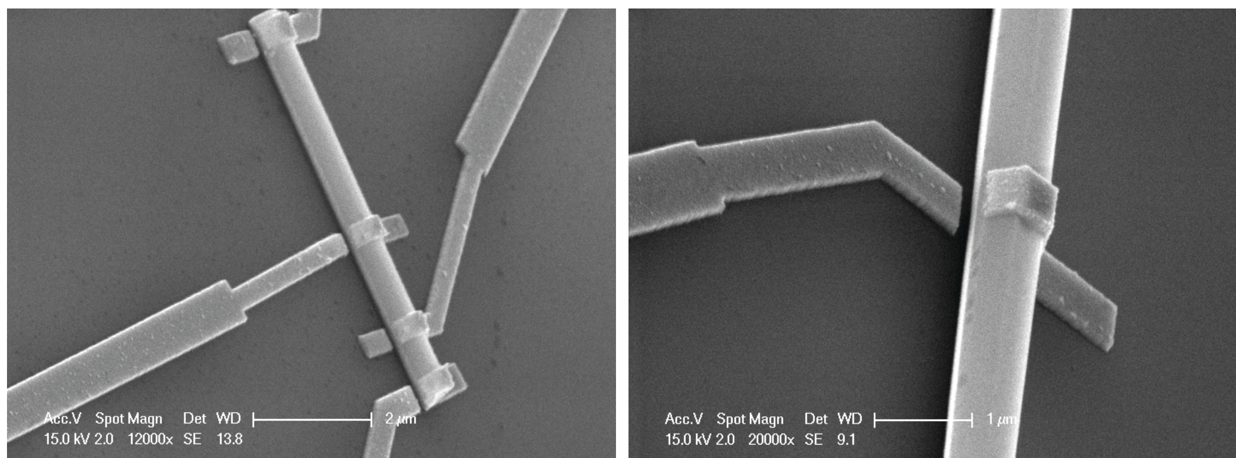

Figure 2.8 a) and b) show an SEM image of a nanowire with a diameter above 300nm contacted by a standard procedure showing the influence of shadow effect.

For nanowires with diameters above 300nm very thick metal layer is required to ensure the continuous contact.

This is inconvenient, since on the one hand processing becomes more expensive and on the other hand much thicker e-beam resist layer complicates the lift-off. In order to eliminate these shortcomings, we developed a planarization process to achieve a partial encapsulation of large diameter nanowires in a dielectric layer, which provides a support for the metal contacts and ensures the metal continuity. As a dielectric material, we chose Hydrogen Silsesquioxane (HSQ) because of its excellent gap-filling and self-planarization properties. The principles of the planarization and contacting process are illustrated in fig. 2.9, and its detailed description is given below :

a) Nanowires are transferred on to a SiO_2 substrate by wet method. b) HSQ is then spun covering the entire wire c) Either dry or wet etching is used to uncover the upper parts of the wires d) Contacts are achieved by standard e-beam lithography.

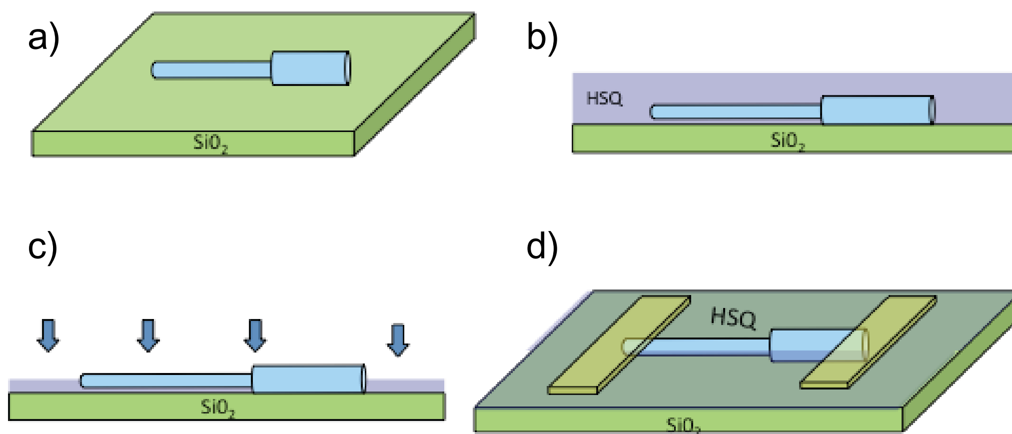

Figure 2.9 Schematic view of planarization process.

This fabrication process has been developed for large wires grown by MOVPE technique with a length in average of 20 um. These wires have a diameter varying from the bottom to the top as shown in figure 2.10. The diameter at the “top” is of the order of 800nm while the “bottom” is about 500nm.

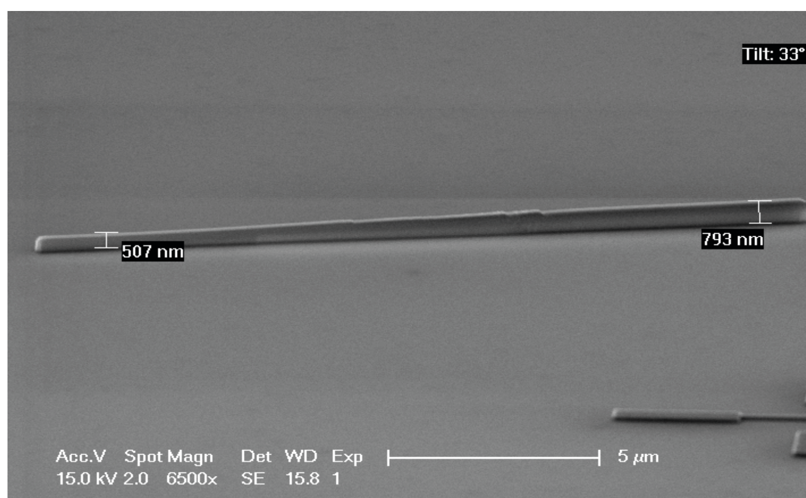

Figure 2.10 SEM image of a MOCVD-grown GaN wire dispersed on a SiO_2 substrate by wet transfer method. Diameter changes along the wire, the base diameter is smaller than the top one but both are above 300nm.

2.2.1 HSQ deposition and transformation

The planarization process begins by covering the sample with HSQ material by spin coating. HSQ is mainly used as a spin-on interlayer dielectric in the fabrication of integrated circuits (Zimmler et al., 2008). HSQ offers three primordial properties that make it a suitable alternative for planarization material: good adhesion to silicon substrates, stability at high temperatures and etch resistivity. HSQ is spun onto the substrate providing a uniform coverage of the surface (figure 2.11), the thickness of the film tends to be thinner on the top of the wires than on the bare substrate (figure 2.11 inset)

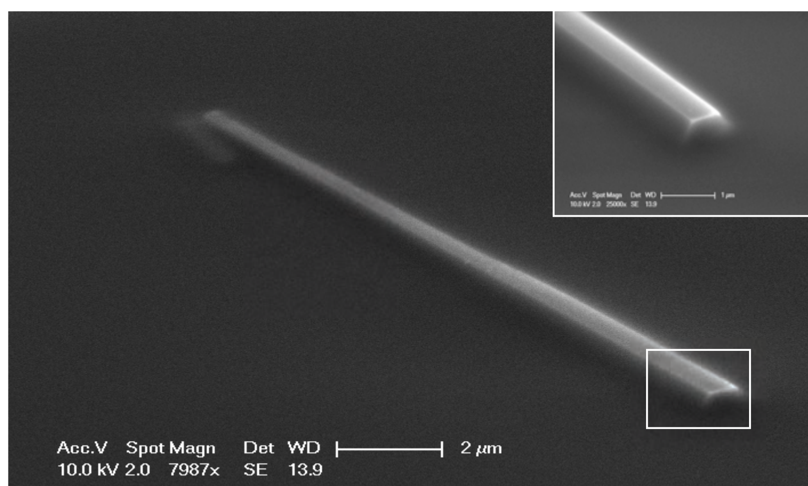

Figure 2.11. SEM image showing a wire after the spinning process. The inset confirms the presence of the planarization material around and up to the middle of the wire.

A thermal treatment is necessary to transform the HSQ chemical composition in order to achieve properties close to those of SiO_2. The thermal process leads indeed to a dissociation of Si-H bonds and creates a rearrangement and formation of SiO_2 bonds. Transformation can also be achieved by a plasma treatment. Due to the removal of hydrogen through heating reactions or plasma treatment a stress in HSQ films is induced and surface cracks may appear. Therefore, the effect of various annealing conditions was explored. A set of five samples were spun in HSQ (FoX 24) at 2000rpm (giving a nominal thickness of 300nm) and then annealed. Table 2.1 summarizes the results for this series of samples.

Temperature	Ambient	Plasma treatment	Annealing Type	Surface state
250	Air	O_2	Hot plate (5min)	Surface cracks
400	N_2	O_2	Tube (1hr)	Surface cracks
400	N_2	None	Tube (1hr)	No cracks
600	N_2	None	Tube (1hr)	No cracks
700	N_2	None	Tube (1hr)	No cracks

Table 2.1 Results of the different annealing conditions on HSQ after spin coating.

For the first sample annealed on a hot plate for 5 minutes, several cracks were found around the whole surface. Moreover, HSQ was dissolved in acetone, which indicates that the annealing was not sufficient to reach a complete hydrogen dissociation. This issue is crucial in the device fabrication because if the HSQ is removed by acetone the whole support for the contacts will be destroyed during the lift off process. We performed annealing experiments in a quartz furnace under continuous nitrogen flow (2000sccm) with a low heat rate of 5ºC/min for one hour. The sample that was firstly treated with oxygen plasma present cracks on the surface. We found that it is possible to obtain films without any surface crack formation if no plasma treatment is carried out before annealing. However, the sample annealed at 400ºC has the problem of HSQ dissolving. To achieve insoluble and crack-free HSQ layer the sample should be annealed at 600ºC or 700°C without plasma treatment.

2.2.2 HSQ etching

Etching of a controlled amount of HSQ is required to uncover the top surface of the wires. The etch depth should be carefully controlled to avoid exposing the underlying silicon substrate. We thinned down the HSQ layer via reactive ion etching (RIE) under the following conditions:

1. Gas = CF_4 30sccm
2. Pressure= 100mTorr
3. DC bias=200V
4. Power= 100W

The HSQ etch rate is roughly 50nm/minute. Figure 2.12 shows a wire after etching the sample for 3 minutes. The image shows that the HSQ covering the upper part of the wire has disappeared, leaving the rest of the surface in good homogeneity. No cracking effects are introduced by the RIE etching process.

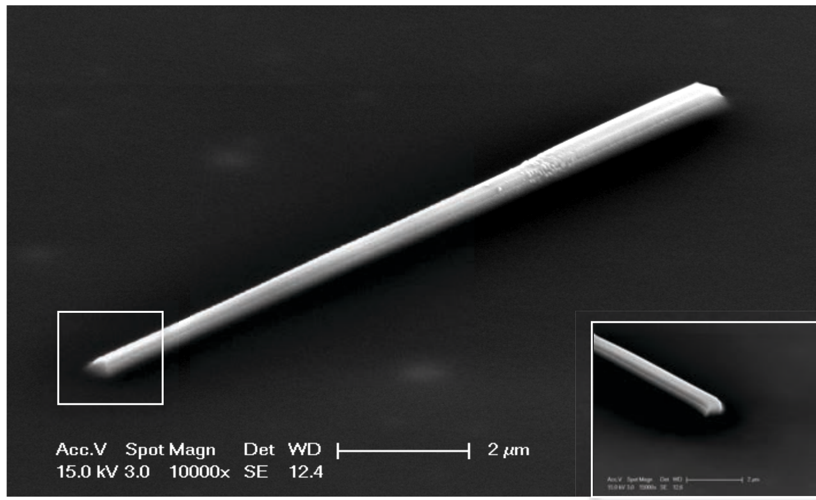

Figure 2.12 SEM image of a single wire after dry etching process.

2.2.3 HSQ removal

Due to the optical absorption of HSQ in the UV, the immersion of nanowires in a HSQ layer may be undesirable for further studies (for example, for photoluminescence or electroluminescence experiments). The effect can be minimized by a final etching step removing the HSQ layer around the nanowire except for the region beneath the contacts.

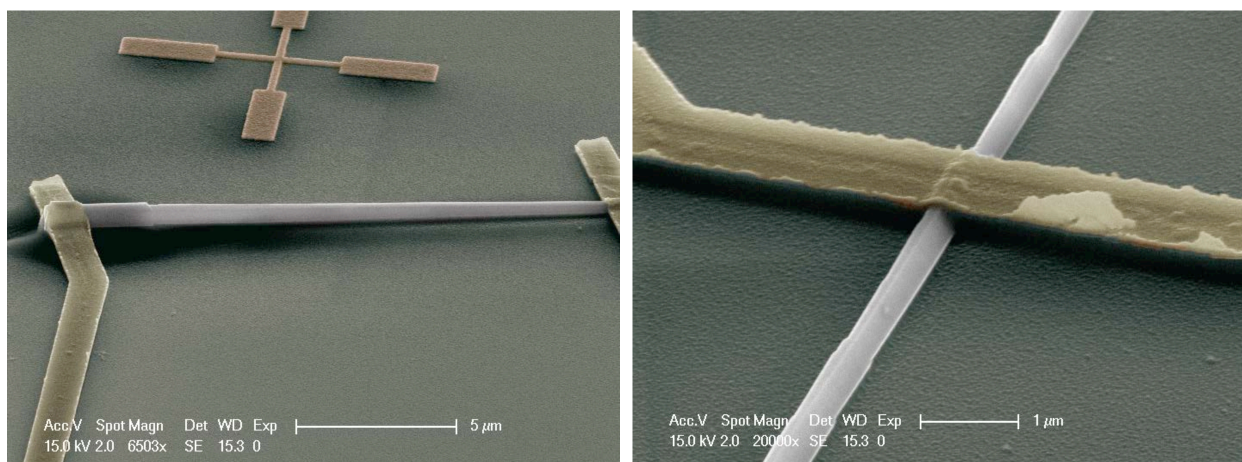

Figure 2.13 a & b. HSQ layer around the wire is removed by RIE process. The HSQ remaining under the contacts acts as support for the metal stripes.

SEM images show the result after 5 minutes CF_4 dry etching. The surface presents smooth morphology and shows no undesirable post-etch deposited material. Figure 2.13 b shows that the HSQ material is still present under the metal stripe. It acts as a support holding the wire and the contacts.

2.3 Fabrication of array nanowire devices

Most of the nanowire device demonstrations reported in the literature are limited to single nanowire devices. However, the device integration and large-scale production are important issues that need to be addressed in view of « real world » applications of nanowire devices. As I have described above, the fabrication of most single nanowire devices employs electron beam lithography as a processing method. This method is flexible and powerful for the fabrication of demonstrators, but it is slow, not scalable and expensive for the fabrication of large sets of nanowire devices. Other contacting techniques, such as the dielectrophoresis, are potential candidates to circumvent this issue.

For optical devices, the active volume required for efficient light generation/detection is often larger than what can be achieved with a single nanowire. It is therefore desirable to develop technology allowing for parallel processing of a large number of nanowires. The fabrication of ensemble nanowire devices presents different technical challenges. For example, the contacting procedure is very different.

In this work we developed a fabrication process allowing for contacting an ensemble of nanowires with a mesa architecture. The step-by-step schematic is shown in figure 2.14. 1) The process begins from the as-grown nanowires on their growth substrate. 2) The space between nanowires is filled with spin-on-glass (HSQ) by spin coating technique. 3) The excess of HSQ is removed by CF_4 dry etching to expose the nanowire tips. 4) The same CF_4 chemistry is suitable to etch down into the Si substrate, which can be used as the bottom contact. 5) The top mesa surface is covered with 200 nm of a conductive indium tin oxide (ITO) layer to contact the nanowire tips. 6) Finally, Ti (10 nm)/Au (150 nm) metallization is deposited on the Si substrate and on the top mesa surface leaving the central part of the mesa open for optical access.

In the following, we describe each step in more detail.

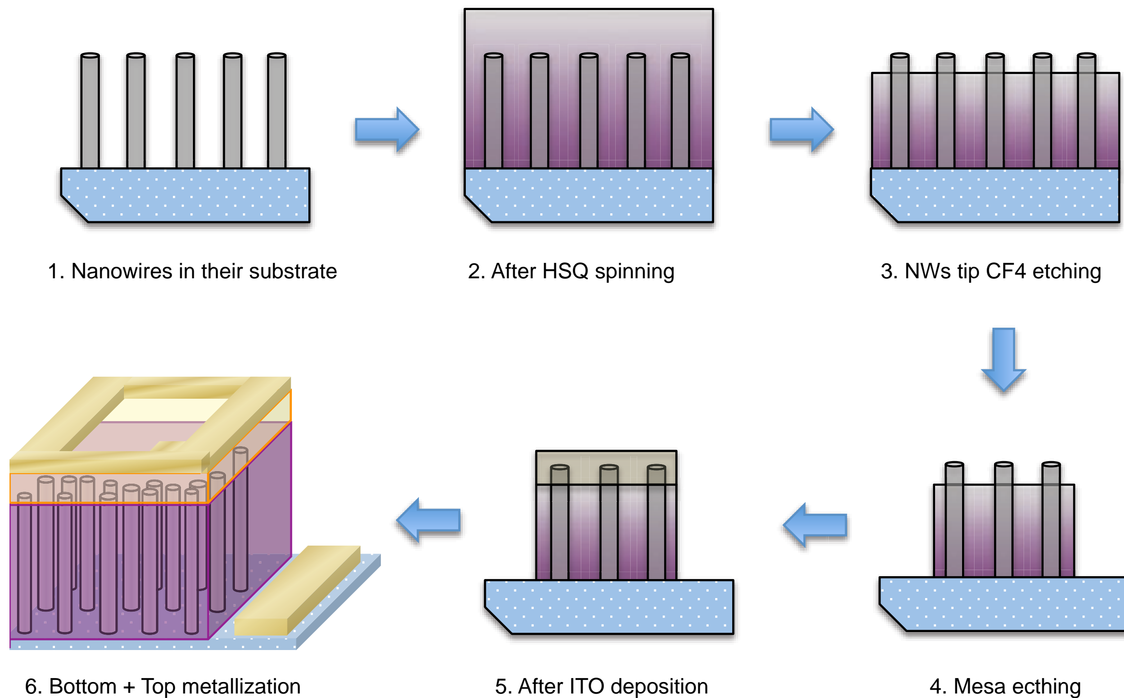

Figure 2.14 scheme of the ensemble nanowire fabrication process.

2.3.1 Encapsulation and transformation

The main idea of nanowire ensemble processing consists in taking the substrate on which the nanowires are grown as a rear electrode and the top of the NWs as the front electrode. However, to connect all the nanowires in parallel short circuits must be avoided, which makes necessary the presence of an insulating material filling the gaps between the nanowires. One of the most studied filling strategies is based on the spin on glass (SOG) materials. As discussed previously in section 2.2.1-2, HSQ provides excellent dielectric properties, ensures a good mechanical stability and enables further processing steps, such as electrical-contact deposition and wire bonding. The nanowire array is thus embedded in HSQ by spin coating at 2000 rpm by 30 seconds. The

thickness of the deposited layer is about 1 µm which is well-suited for MBE grown GaN nanowires with a typical length of about 1 µm. An example of HSQ encapsulation is shown in figure 2.15

After the encapsulation, HSQ was transformed into SiO_2 using a thermal annealing under optimal conditions established in section 2.2.1 (1h under N_2 atmosphere at 700°C).

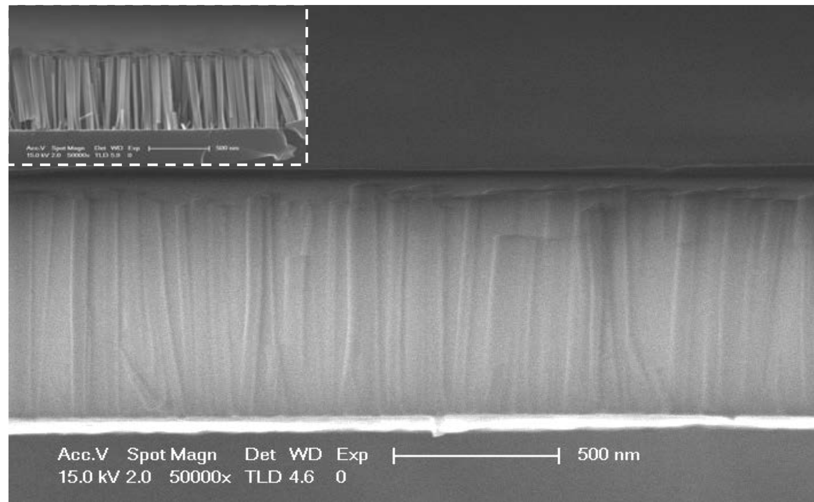

Figure 2.15 HSQ encapsulation of nanowires. The inset shows the nanowires on their substrate before the HSQ spin coating deposition.

2.3.2 RIE Etching

Etching is required to remove the filling material down to the top of the nanowires in order to achieve good metallic contacts. It is clear from images 2.16 a & b, that the 1 min RIE etching with CF_4 gas successfully uncovered the top of the nanowires. The alternative methods such as chemical-mechanical polishing have been proposed, however they generally result in delamination and surface cracking.

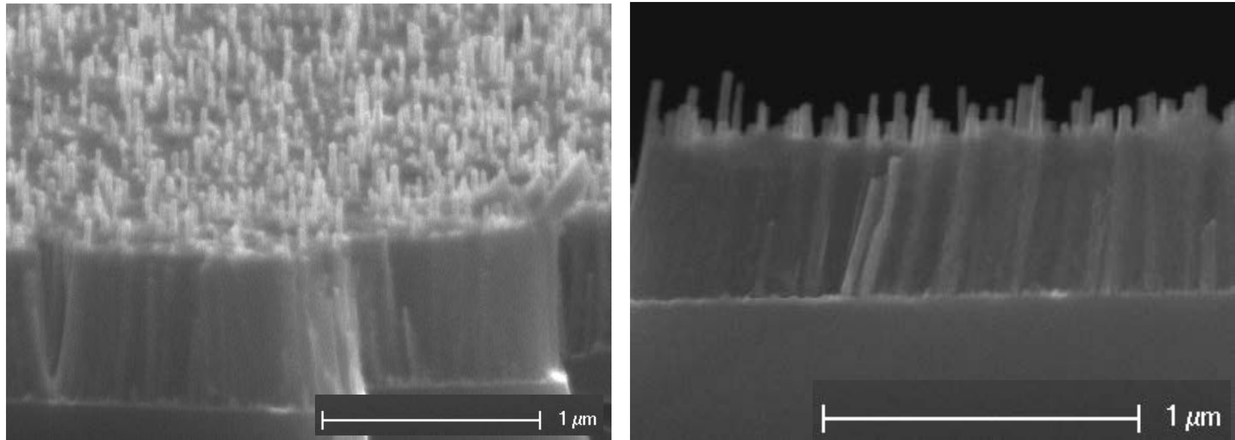

Figure 2.16 45° tilted SEM of NWs after reactive ion etching.

2.3.3 Photolithography

Optical lithography is basically a photographic process by which a light sensitive polymer, called a photoresist, is exposed and developed to form three-dimensional relief images on the substrate. In general, the ideal photoresist image has the exact shape of the intended pattern in the plane of the substrate. Thus, the final resist pattern is binary: parts of the substrate are covered with resist while other parts are completely uncovered. Figure 2.17 shows the process flow for a photolithography process:

1. The sample is spin-coated with photoresist. 2. A soft bake on a hot plate is used to ensure a good adhesion to the sample. 3. The sample is exposed to UV radiation (if necessary, an alignment step is performed before exposure). 4a In the case of positive resist, the sample is developed after UV exposure, the resist in the areas that were exposure is removed. 4b) For image reversal resists, a second bake and a flood exposure makes the resist negative. 4c) After developing, the resist in the areas exposed in step 3 remains.

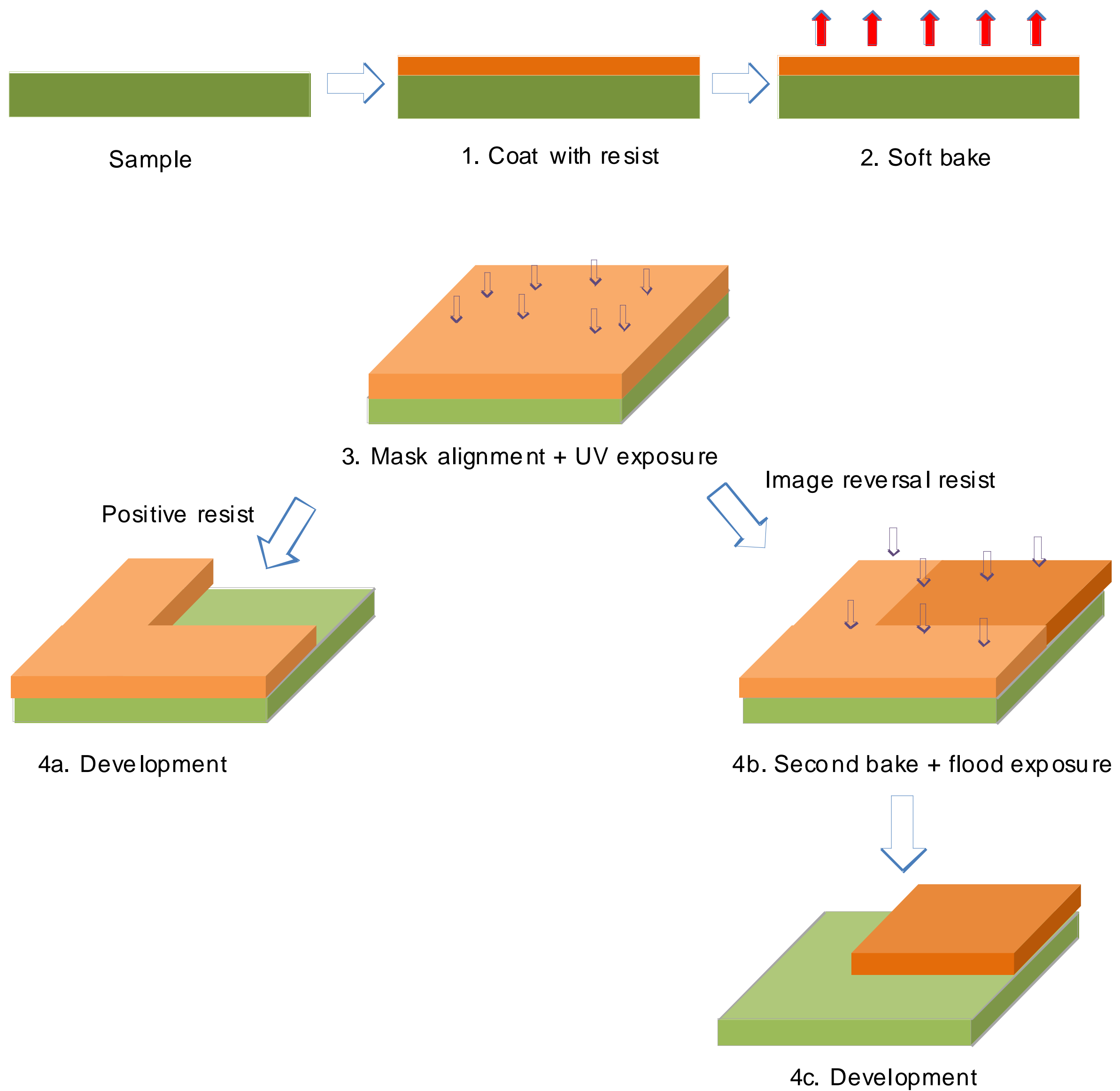

Figure 2.17 Photolithography process

The sample is first covered with a photoresist by spin coating. Then, a soft bake is carried out in order to improve the adhesion of the resist to the sample and to make the photoresist sensitive to UV light by driving away the solvent. The sample is then exposed to UV radiation through a physical mask that will produce the pattern image on the resist. The chemical properties of the resist regions struck by radiation change in a manner that depends on the resist type.

Photoresists can be divided in positive and negative. For positive resists, UV light is shone upon the area where the underlying material has to be removed. In this case, UV light changes the chemical structure of the resist so that it becomes soluble and can be then removed away by the developer solution. The parts of the substrate covered with unexposed resist will be protected from etching, ion implantation, or other pattern transfer mechanism.

Negative resists behave in just the opposite way. Exposure to the UV light causes the negative resist to become polymerized, and more difficult to dissolve. Therefore, the negative resist remains on the surface wherever it is exposed, and the developer solution removes only the unexposed portions.

It should be noted that the resulting profile is different for positive and negative photoresist. For positive photoresist, the sidewalls of the pattern form an angle larger than 90° with the substrate. For the negative resist, this angle is less than 90°, that is there is a overhang. This specific profile achieved for a negative resist facilitates the lift-off process. Therefore, negative resists are used when a material deposition and lift-off is desired.

A third class of photoresists is a reversible photoresist. It presents a large flexibility since it can be used both as a positive as well as a negative resist. For contact deposition on the nanowire ensembles, we have chosen the reversible resist. As illustrated in figure 2.17, when a reversal bake is done, exposed areas become insoluble in the developer. In this work, commercial photoresists from Shipley Microposit were used, S1818 is used as positive resist while AZ5214 is used as reversal resist.

Mesa definition

First, we define the device sizes by mesa etching. The sample is spin coated with S1818 resist at 4,000 rpm during 60 seconds, then a softbake of one minute is carried out, the sample is exposed to UV light during 7 seconds using Suss MJB4 mask aligner and developed during 20 seconds in MF319. We have designed a photo mask with multiple mesa sizes from 300um to 50um (figure 2.18a).

After photolithography, an RIE etch process is carried out using CF_4 chemistry with the same parameters described in section 2.2.2. The etching is done down into the Si substrate and allows removal of the unwanted

nanowires outside the mesas Figure 2.18b.

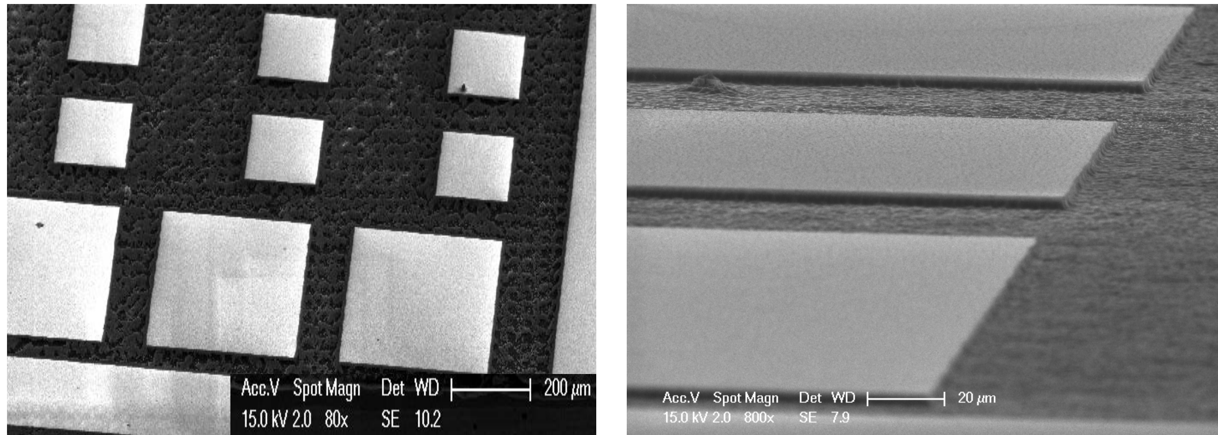

Figure 2.18. a) Definition of mesa by photolithography, the resist protects the mesa areas from RIE etching. b) The mesa etching performed by CF_4 allows taking off the HSQ and also removing the nanowires outside the mesas.

2.3.4 Indium Tin Oxide deposition

We performed a second photolithography step in order to define a top contact over the nanowires. The sample was spun in AZ5214 at 4,000 rpm then baked during one minute at 110°C. In order to avoid a short circuit, alignment between the mesas and the desired ITO layer must be done. Then the sample was again baked for two minutes at 120ºC to change resist properties and a flood exposure during 40 seconds was done. We used a AZ400K:H2O 1:4 as developer solution during 20 seconds.

Transparent conductive electrodes are important components of thin-film solar cells (Perraud et al., 2009), light-emitting diodes (Kuo et al., 2004), and other optoelectronic devices (Chu et al., 2011) such as displays (Ryu et al., 2003). Among them, indium tin oxide (ITO) is one of the most widely used materials due to its high conductivity and transparency in the UV-visible range.

The crystalline structure, tin doping level, and composition of ITO films produced by different processes vary

significantly. Resistivity, transmittance and carrier concentrations fluctuate depending on the process treatment (Morikawa, 2000)(Kamei, 2001). ITO films are prepared using different methods such as thermal evaporation, spray pyrolysis, magnetron sputtering, sol gel. In our case we used magnetron sputtering to prepare the ITO films. This technique offers high deposition rate, high-purity films, good adhesion of film, and excellent uniformity on large-area substrates.

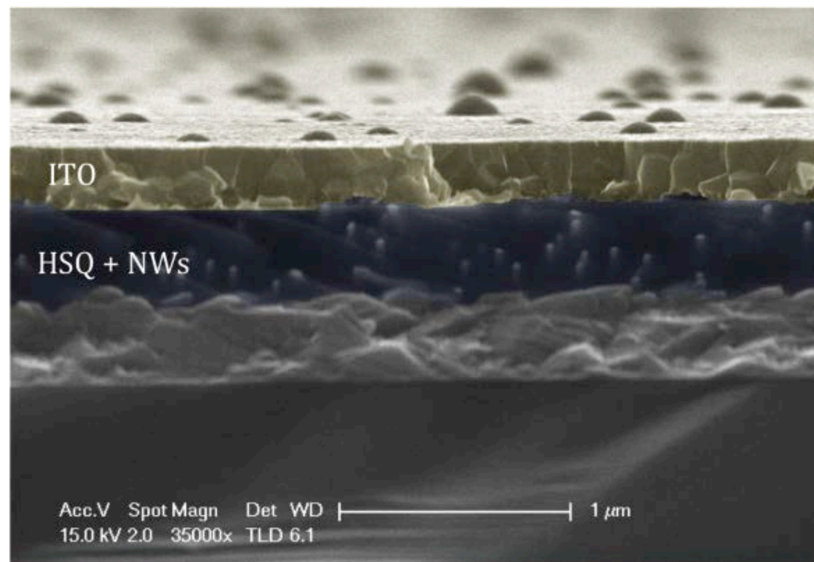

Figure 2.19 SEM image of a sample after ITO deposition and annealing

In order to explore the electrical properties of ITO, we deposited a 200nm (typical thickness required to cover the nanowire tips) ITO layer on lime glass by RF sputtering under Ar atmosphere with a RF power of 100W at room temperature. Since the ITO films are composed of small crystal grains, there are inevitably many grain boundaries that may behave as barriers for electrons and result in the high in-plane resistance of the films. Annealing is expected to have important impact on the improvement of crystallization as well as conductivity. Earlier studies (Enery & Vm, 1996),(Y. Xu, 2006) showed that when temperature is less than 150ºC the annealing effect is negligible. We performed rapid annealing for different temperatures under O_2 atmosphere during four minutes. From four-point measures we found that resistivity decreases from 22.15 $\times 10^{-4}$ Ω·cm for a temperature of 200ºC to a value of 4.71$\times 10^{-4}$ Ω·cm at 400ºC. We therefore use 400°C annealing for nitride based nanowire devices.

Top and bottom contacts

Although probe measurements are possible with a bare ITO layer, to get a better reproducibility and to allow for wire bonding a metal contact is required at the substrate and on the top mesa surface. As a final step of the process, a third photolithography has been performed to put a top and bottom contacts. The lithography was done using AZ5214 resist. The Ti/Au metallization was performed and the contacts were defined by lift-off. The final device is shown in figure 2.20. The top and bottom metallization allows for electric access to device (without damaging the ITO layer) and also provides a mechanical support for the wire bonding. Wire bonding consists in welding a fine metallic wire onto the bonding pad with ultrasonic energy. This process is used to ensure stable and low-resistance electrical connection between the device and the “outside world”. The wire is connected to external macroscopic gold pads glued by silver paint together with the device substrate on the same metallic holder. The silver paint provides also a good electrical contact to the backside silicon substrate as well as thermal contact (Dawson & Ryan, 1996).

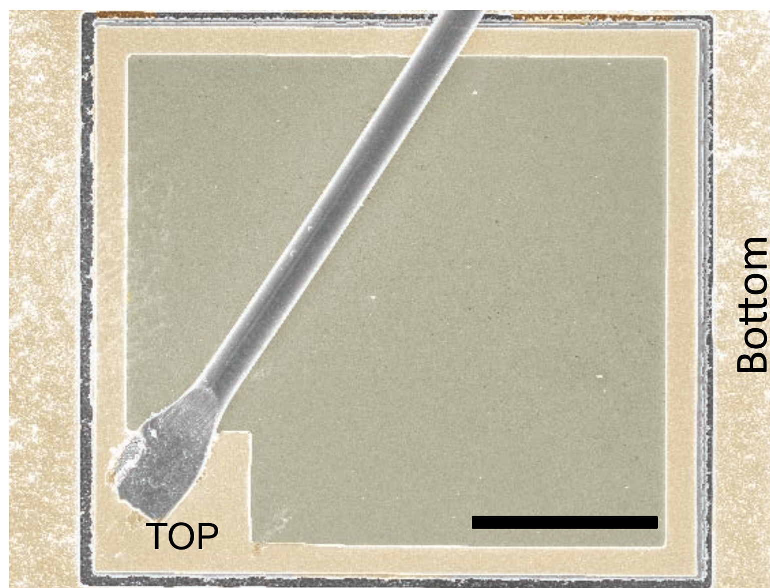

Figure 2.20 SEM top view images of the mesa device. a) The top contact is defined around the mesa structure leaving a 80x80 um^2 space for the wire bonding. The bottom contact is achieved on the Si etched substrate (the scale bar is 100um).

Conclusions

In this chapter, we have discussed the nanofabrication process for devices based on single nanowires and on nanowire ensembles.

We have developed a processing technology to fabricate single nanowire devices using electron beam lithography. We have shown that our methodology provides good reliability, high resolution patterning (multiple contacts can be achieved with a separation of 150nm) and excellent control of the positioning of the electrodes (possibility of a two step lithography with precise alignment on the p- and n- extremities of the same nanowire). For nanowires with diameter beyond 300nm an additional planarization step was developed to ensure the contact continuity.

However, this approach dedicated to single nanowire device demonstrators has certain limitations. Indeed, one by one fabrication of devices using e-beam lithography is time-consuming and expensive. Therefore, this approach is not scalable. The perspective of this work is to develop cost-effective ways to integrate single-nanowire devices on a large scale. In this context, transfer alignment methods such as fluid flows in microchannels (Dunwei Wang, Ryan Tu, 2005), Langmuir-Blodgett technique (Mai et al., 2009), blown bubble films (Yu, Cao, & Lieber, 2007) and dielectrophoresis (C. H. Lee, D. R. Kim, & Zheng, 2010) present interesting solutions to organize nanowire and to control their orientation.

The fabrication of a second category of devices based on nanowire ensembles has been successfully developed. Using encapsulation, photolithography and dry etching we can produce mesa devices based on thousands of nanowires connected in parallel. As a perspective, this approach can be further generalized to produce an array of nanowires that can be addressed individually. A prerequisite for that is to start from ordered nanowire growth and to form a mesh of cross-patterned top and bottom electrodes. This technology presents interest to produce matrices of micro-LEDs or micro-photodetectors with the resolution at the diffraction limit.

The top contact can also be further optimized. ITO has a relatively high in-plane resistivity and forms a potential barrier when put in contact with semiconductor nanowires. An alternative approach would be the use of random mesh networks of carbon nanotubes that exhibit optical transparency equivalent, and resistivity properties equivalent to ITO (J.-Y. Lee, Connor, Cui, & Peumans, 2008).

Bibliography

Chu, S., Wang, G., Zhou, W., Lin, Y., Chernyak, L., Zhao, J., Kong, J., et al. (2011). Electrically pumped waveguide lasing from ZnO nanowires. *Nature Nanotechnology*, *6*(July), 4-8. doi:10.1038/NNANO.2011.97

Davydov, a V., Motayed, a, Boettinger, W. J., Gates, R. S., Xue, Q. Z., Lee, H. C., & Yoo, Y. K. (2005). Combinatorial optimization of Ti/Al/Ti/Au ohmic contacts to n-GaN. *Physica Status Solidi (C)*, *2*(7), 2551-2554. doi:10.1002/pssc.200461605

Dawson, A. L., & Ryan, D. H. (1996). Heat capacity of silver paint. *Review of Scientific Instruments*, *67*(7), 2648. doi:10.1063/1.1147183

Dunwei Wang, Ryan Tu, L. Z. and H. D. (2005). Deterministic One-to-One Synthesis of Germanium Nanowires and Individual Gold Nano-Seed Patterning for Aligned Nanowire Arrays. *Angewandte Chemie-International Edition*, *44*, 2925-2929.

Enery, R., & Vm, N. (1996). ~ P~9am0n, *1481*(95), 205-208.

Ho, J.-K., Jong, C.-S., Chiu, C. C., Huang, C.-N., Shih, K.-K., Chen, L.-C., Chen, F.-R., et al. (1999). Low-resistance ohmic contacts to p-type GaN achieved by the oxidation of Ni/Au films. *Journal of Applied Physics*, *86*(8), 4491. doi:10.1063/1.371392

Jang, H. W., Kim, S. Y., & Lee, J.-L. (2003). Mechanism for Ohmic contact formation of oxidized Ni/Au on p-type GaN. *Journal of Applied Physics*, *94*(3), 1748. doi:10.1063/1.1586983

Kamei, M. (2001). Origin of the crystalline orientation dependence of the electrical properties in tin-doped indium oxide films. *Thin Solid Films*, *392*(2), 265-268. doi:10.1016/S0040-6090(01)01041-0

Kuo, C., Chang, S., Su, Y., Chuang, R., Chang, C., Wu, L., Lai, W., et al. (2004). Nitride-based near-ultraviolet LEDs with an ITO transparent contact. *Materials Science and Engineering B*, *106*(1), 69-72. doi:10.1016/j.mseb.2003.09.018

Lee, C. H., Kim, D. R., & Zheng, X. (2010). Orientation-Controlled Alignment of Axially Modulated pn Silicon Nanowires. *Nano letters*, 5116-5122. doi:10.1021/nl103630c

Lee, J.-Y., Connor, S. T., Cui, Y., & Peumans, P. (2008). Solution-processed metal nanowire mesh transparent electrodes. *Nano letters*, *8*(2), 689-92. doi:10.1021/nl073296g

Mai, L., Gu, Y., Han, C., Hu, B., Chen, W., Zhang, P., Xu, L., et al. (2009). Orientated Langmuir-Blodgett assembly of VO(2) nanowires. *Nano letters*, *9*(2), 826-30. doi:10.1021/nl803550k

Morikawa, H. (2000). Crystallization and electrical property change on the annealing of amorphous indium-oxide and indium-tin-oxide thin films. *Thin Solid Films*, *359*(1), 61-67. doi:10.1016/S0040-6090(99)00749-X

Perraud, S., Poncet, S., Noël, S., Levis, M., Faucherand, P., Rouvière, E., Thony, P., et al. (2009). Full process for integrating silicon nanowire arrays into solar cells. *Solar Energy Materials and Solar Cells*, *93*(9), 1568-1571. doi:10.1016/j.solmat.2009.04.009

Ryu, H., Kang, J., Han, Y., Kim, D., Pak, J. J., Park, W.-K., & Yang, M.-S. (2003). Indium-tin oxide/Si contacts with In- and Sn-diffusion barriers in polycrystalline Si thin-film transistor liquid-crystal displays. *Journal of Electronic Materials*, *32*(9), 919-924. doi:10.1007/s11664-003-0223-y

Search, H., Journals, C., Contact, A., Iopscience, M., & Address, I. P. (1996). Schottky barrier properties of various metals on n-type GaN, *1464*.

Wang, D.-F., Shiwei, F., Lu, C., Motayed, A., Jah, M., Mohammad, S. N., Jones, K. A., et al. (2001). Low-resistance Ti/Al/Ti/Au multilayer ohmic contact to n-GaN. *Journal of Applied Physics*, *89*(11), 6214. doi:10.1063/1.1350617

Xu, Y. (2006). Vacuum annealing effects on properties of ITO films prepared by reactive low voltage ion plating technique. *Proceedings of SPIE*, *6024*, 602428-602428-6. Spie. doi:10.1117/12.666953

Yu, G., Cao, A., & Lieber, C. M. (2007). Large-area blown bubble films of aligned nanowires and carbon nanotubes. *Nature nanotechnology*, *2*(6), 372-7. doi:10.1038/nnano.2007.150

Zimmler, M. a, Stichtenoth, D., Ronning, C., Yi, W., Narayanamurti, V., Voss, T., & Capasso, F. (2008). Scalable fabrication of nanowire photonic and electronic circuits using spin-on glass. *Nano letters*, *8*(6), 1695-9. doi:10.1021/nl080627w

3. Photodetectors based on nanowire ensembles

In this chapter I describe the fabrication and operation of visible blind photodetectors based on GaN nanowire ensembles. First, I give a brief overview of the different photodetector types, as well as parameters to evaluate them. Then I discuss the growth of GaN nanowires on Si (111) and the photodetector design and fabrication. I then describe the electric properties of the device, followed by an optical characterization in terms of UV optical response, photocurrent spectroscopy and operation speed. Finally, I present the results of OBIC map measurements showing the homogeneity of the detector response.

3.1 Introduction

Interest of nitride nanowires for light detection

One of the main motivations to use nitride nanowires for light detection is their high material quality. Indeed, they can be grown on cheap lattice-mismatched substrates without dislocation formation therefore reducing the device cost and improving the performance. In addition, thanks to the high surface to volume ratio, they exhibit high photoconductive gain stemming from the spatial separation of photogenerated carriers. This property demonstrated in particular in ZnO (Soci et al., 2007) and GaN (R.-S. Chen et al., 2007) single nanowires leads to an enhanced responsivity of the nanowire photodetectors. Moreover, the nanowire small size makes them good candidates for the fabrication of highly sensitive focal plane arrays with diffraction-limited spatial resolution.

III-nitride nanowires are well suited for light detection in the UV spectral range. UV photodetectors based on a p-n junction in a single GaN nanowire (Son et al., 2006) have been reported. As we will discuss later within the framework of this thesis, a UV photodetector based on a single nanowire containing GaN/AlN quantum discs has been developed. Photodetectors based on nanowire ensembles have also been demonstrated. They make use of a p-n heterojunction between two different materials in order to overcome difficulties related to p-type doping for example, n-type GaN nanowires on p-type Si substrate (Tang et al., 2008) or n-type ZnO nanowires on p-type GaN substrate (C.-H. Chen, Chang, et al., 2009).

Importance of the UV radiation detection

The ultraviolet (UV) region of the electromagnetic spectrum with wavelengths from 10nm to 400nm cannot be detected by the human eye. This spectral region is associated with high-energy electronic transitions related to radiation coming from hot bodies and combustion processes. The detection of UV radiation is important for numerous applications such as chemical sensing, flame detection, ozone hole sensing, short-range communication and biological agent detection. Military interests are also involved since missile plumes and aircraft engines emit ultraviolet radiation (Jose Luis Pau et al., 2006). UV astronomy requires UV detection to discern the chemical composition, densities, and temperatures of the interstellar medium. Ultraviolet radiation has a serious impact on human health. For example, monitoring the quantity of UV is primordial to avoid skin diseases (Zgórka & Kawka, 2001)(Caria et al., 2002)

To effectively detect the UV radiation it is important to develop photodetectors that are sensitive only to UV wavelengths and not to the visible light. These are the so-called visible blind photodetectors.

Semiconductors for UV photodetection

UV photodetection has traditionally been accomplished by photomultiplier tubes (PMTs) or thermal detectors. However, they show some limitations such as fragility, need for high power supplies, and high cost. Modern UV photodetectors are based on semiconductors since they are lightweight, small and insensitive to magnetic fields.

Due to their well-established technology, UV silicon photodiodes are the most common devices for UV photodetection. Unfortunately, these kinds of devices are damaged under long UV exposure since they are coated with an anti-reflection SiO_2 layer. Nitride semiconductors, in particular GaAlN alloy with a bandgap spanning from 3.4 to 6.2 eV, are suitable materials for ultraviolet detection. Compared to Si devices, III-nitride photodetectors present several advantages. The large band-gap provides low thermally generated dark current, chemical stability, high melting temperature and good radiation hardness. In addition, the wide bandgap is itself is an important advantage for photodetectors since it enables room-temperature operation and provides intrinsic visible-blindness. In comparison to their closest competitor SiC that presents similar characteristics, III nitrides offer different advantages such as a better spectral selectivity due to their direct bandgap, a higher absorption coefficient, and the possibility of selecting the cut-off wavelength by changing the Al content in the ternary alloy. In addition, SiC technology has some limitations, as filters are needed to stop low energy photons, and degradation becomes an issue because of the high voltage supply requirements (Stanislav I., 2009).

The main drawback of nitride photodetectors is the poor crystal quality. As discussed in chapter I, the lack or the excessive cost of high-quality lattice-matched substrates for homoepitaxy leads to a material with a high density of dislocations (up to 10^9 cm^{-2}). These dislocations can become charged and act as scattering centers, thereby degrading the photodetector performance. Most development efforts involving GaN and AlGaN UV photodetectors have been focused on the use of sapphire substrates with different strategies to reduce the defect density. The growth on Si substrates is also actively explored in view of device cost reduction and compatibility with standard Si technology. The material quality can be strongly improved by replacing thin films by nanowires as will be discussed later in this chapter.

Despite the difficulties with high quality nitride growth, considerable progress in GaN and AlGaN thin film photodetectors has been made (Monroy, 1998)(J. Pau, 2002). In the following, I present some of the important parameters of UV photodetectors followed by a brief overview of the existing types of nitride photodetectors, providing the necessary background information for further discussions.

Photodetector parameters

The performance of a photodetector is described by a set of parameters and figures of merit, that are briefly described below:

Responsivity: This parameter is defined as the photogenerated current (I_{ph}) per unit of incident optical power (P_{opt}).

$$R = I_{ph} / P_{opt} \; [A/W]$$

The responsivity can also be defined in terms of quantum efficiency η (number of electron-hole pairs generated per incident photon) and gain g (number of carriers detected per photogenerated electron-hole pair) using:

$$R = qg\frac{\lambda\eta}{hc}$$

where λ is the radiation wavelength, h is the Planck constant, c is the speed of the light, and q is the electron charge.

Response time and bandwidth: The photodetector speed may be limited by the carrier speed, by the recombination time and by charging effects (RC constant). The temporal response of a photodetector is characterized by the decay time τ_d, defined as the time in which photocurrent drops from 90% to 10% of its maximum value, when the device is excited with rectangular light pulses. The bandwidth is defined as the frequency at which photocurrent is 3dB lower than the low-frequency response.

Noise equivalent power and detectivity: The NEP is defined as the incident optical power for which the signal-to-noise ratio is equal to 1 and is given by:

$$NEP = \frac{I_n}{R}[W]$$

where I_n is the noise current and R represents the responsivity. The normalized detectivity is the most important parameter to characterize the signal-to-noise ratio performance of photodetectors. In general terms, the

photocurrent signal increases in proportion to the active optical area A, in addition, the noise current increases with the square root of the product of the active optical area with the bandwidth BW. Thus, in order to compare two photodetectors with different dimensions, the expression for normalized detectivity can be defined by the following expression:

$$D^* = \frac{R\sqrt{A \cdot BW}}{I_n} \quad \left[\frac{cm \cdot Hz^{1/2}}{W}\right]$$

UV/Vis rejection contrast: It is defined as the ratio of the photodetector responsivity at the cutoff wavelength and the photodetector responsivity at 400nm.

Types of nitride UV photodetectors

(i) Photoconductors

UV photoconductor devices have been demonstrated. They consist of a bulk semiconductor bar with ohmic contacts on top to apply a bias voltage. When light hits the semiconductor and electron-holes pairs are generated, the conductivity changes which can be detected by the current variation in the circuit. The speed of these devices depends on the minority carrier recombination time. If the lifetime of minority carriers is greater than the transit time between contacts of the majority carriers, the photoconductive gain is larger than 1. If a mechanism limiting the minority carrier recombination rate is present (e.g. a spatial separation of the photogenerated carriers) this kind of photodetector can attain very high values of photoconductive gain and responsivity. However, this also has a negative impact on the device speed, which depends on the recombination time of minority carriers.

GaN and AlGaN photoconductors have been reported (Stevens, 1995),(Monroy et al., 1999),(Monroy et al., 2001), (J. Pau et al., 2002),(Martens et al., 2011), showing high photoconductivity gain, selective spectral range and low power consumption. However, as pointed out earlier, dislocations and point defects play an important role in III-nitride photodetector properties, as they are considered to be responsible for persistent photoconductivity (PPC) effects and reduced UV/visible contrast. They are also the main low frequency noise source because of the generated electron mobility reduction (Elías Muñoz, 2007).

(ii) Schottky photodiodes

These devices are based on a metal-semiconductor junction. When a semiconductor is brought into contact with a metal, a charge redistribution is produced until the Fermi levels of both materials are lined up. During this process, a part of the semiconductor close to the junction will be depleted of charges. Thus, an electric field directed from semiconductor to metal will be formed. At equilibrium, the Fermi levels of the metal and the semiconductor attain the same value and the energy-band diagram takes the form illustrated in figure 3.1 The electric field present in the space charge region W will separate the photogenerated electron-hole pairs giving rise to the photocurrent. The width of the space charge region depends on the distribution and concentration of doping impurities and the barrier height of the metal-semiconductor junction.

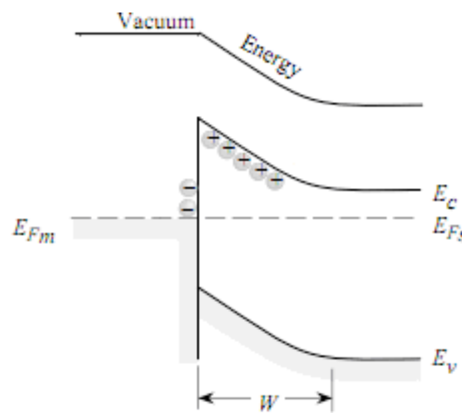

Figure 3.1 Band diagram of the metal - semiconductor Schottky junction for n-type semiconductor

One of the advantages of Schottky photodiodes is their fast response resulting from the high electric field (thus the short carrier transit time) across the junction under reverse bias. Moreover, previous works have shown the possibility of shifting the cutoff to shorter wavelengths by varying the Al mole fraction in AlGaN Schottky photodiodes due to the broadening of the semiconductor energy bandgap (Monroy et al., 2000). They present UV/Vis contrast above 10^3 and good photocurrent linearity (more than five decades). They don't require p-type doping of AlGaN (Monroy et al., 2000). Nevertheless, they exhibit low responsivity mainly due to the small optical absorption introduced by the thin Schottky metal, high leakage currents and poor noise performance.

(iii) Metal-semiconductor-metal

Metal-semiconductor-metal (MSM) devices can be described as two Schottky diodes in opposition. The typical geometry consists of two interdigitated Schottky electrodes deposited on a non-intentional doped semiconductor material. MSM photodiodes present extremely low dark current due to the high material resistivity and to the rectifying nature of the contacts. The reduction of the finger width and pitch reduces the reach-through voltage leading to an enhancement of the responsivity (Palacios, Monroy, Calle, & Omnès, 2002). However, the responsivity is reduced by the use of opaque metals to obtain Schottky contacts. Although backside illumination can be used to solve this problem, it also creates problems in optical lithography alignment, device processing and packaging. Therefore, the use of a transparent conductor for the Schottky electrode will maximize the responsivity. MSM photodiodes are particularly suitable for high-speed applications, given their intrinsically low capacitance. Their time response is usually limited by the carrier transit time.

(iv) P-I-N Photodiodes

P-n and p-i-n photodiodes are the most commonly used photovoltaic structures for radiation detection in the infrared to UV regions of the spectrum. In this case the intrinsic field due to the pn junction separates the electron hole pairs until they reach the electric contacts. These devices can operate under reverse polarization, reducing the capacitance of the device to increase its bandwidth. Moreover, they show good responsivity, linearity, high breakdown voltages and in comparison with Schottky photodiodes they present small dark currents (Osinsky, Gangopadhyay, Gaska, Williams, & Khan, 1997). However, photodetectors based on p-n structures usually work in a photovoltaic regime. The responsivity is related to the collection of charge carriers generated by photon absorption in the space charged region, so increasing the reverse polarization will lead to an increase in space charged region thickness, which will decrease the transit time of the photogenerated carriers and enhance the responsivity of the device. Another way to get the same result without the necessity of polarization is by introducing an intrinsic material between the p- and n- doped parts (p-i-n junction).

Reports on p-i-n GaN devices show high responsivity (100-159 mAW-1) at zero bias, and optical power linearity over more than five decades (Monroy et al., 2000). Even very high-speed photodiodes have been reported [car

98] with decay time below 1ns at -5V. This result was obtained by increasing the intrinsic layer thickness in order to achieve low capacitance; therefore, the RC product no longer limits the time response. The main drawback of this design is the low responsivity below 30 mAW-1.

3.2 Nanowire photodetector structure

To solve the problem of the poor material quality of thin nitride films, the active material of the photodetector can be replaced by nanowires. Indeed, the above described photodetector types such as photoconductors, Schottky diodes and p-n diodes can be implemented using these nanostructures. In this chapter I focus on the p-i-n GaN nanowire detector.

SAMPLE STRUCTURE

The photodetector design is based on an ensemble of GaN nanowires containing a p-i-n junction grown on a Si(111) substrate. The nanowires were grown on an n+ type silicon (111) substrate by molecular beam epitaxy. The growth is performed at 790ºC under nitrogen rich conditions. This procedure results in a dense ensemble of nanowires. The nanowire density is ~10^{10} cm^{-2}, giving an average substrate coverage of ~75%. The average height is 0.9±0.1 μm and the diameter is 50±20 nm. The nanowire base (0.4 μm) is n-doped with Si, it is followed by a nominally undoped GaN segment (0.1 μ m), and the nanowire top (0.4 μm) is p-doped with Mg. The resulting nanowire morphology is shown in the SEM image of Fig. 3.3. The dopant concentrations are estimated from the Hall measurements on 2D layers grown at the same growth rate and dopant flux. This measurement yields a free carrier concentration of 10^{19} cm^{-3} ($5x10^{17}$ cm^{-3}) for n-type (p-type) doping. However, it should be noted that the dopant incorporation in nanowires can be strongly different from thin films, therefore these numbers should be considered only as an estimation. The epitaxy was performed by S.-T. Chou , Y.-T. Lin and L.-W. Tu from NSYSU in Taiwan within the framework of the ANR project « Nanophotonit ».

(111)

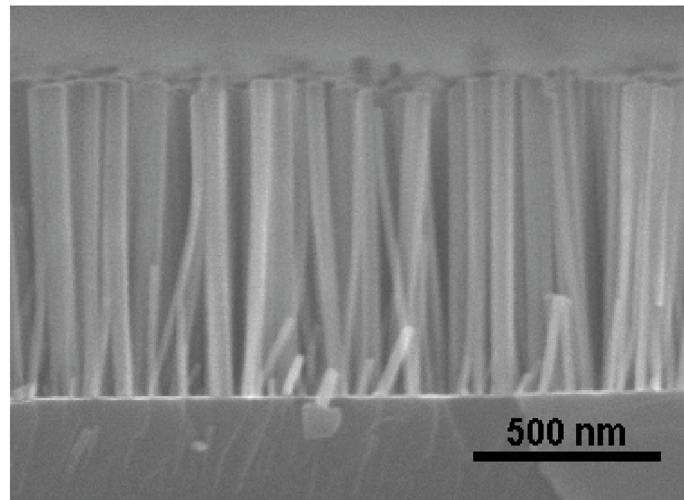

PHOTODETECTOR FABRICATION

To fabricate the photodetector based on the nanowire ensemble (see chapter 2), the GaN nanowires were first encapsulated into a spin-on glass to provide the mechanical stability and the support for the top contact. Then mesa were defined by RIE dry etching. The top mesa surface was covered with 200 nm of a conductive transparent indium tin oxide (ITO) layer to contact the nanowire tips. Ti (10 nm)/Au (150 nm) metallization was then deposited on the Si substrate and on the top mesa surface leaving the central part of the mesa open for illumination. A top view SEM image is shown in figure 3.3 as well as a scheme of the NW photodetector. The nanofabrication process of photodetectors based on GaN nanowire ensembles is presented in details in chapter II

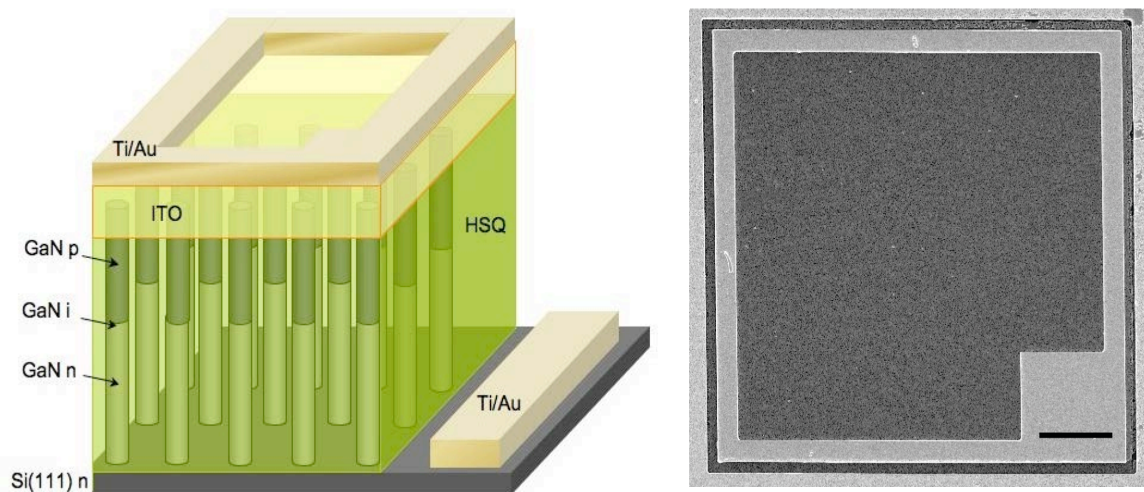

Figure 3.4 a) A schematic representation of a mesa photodetector. b) Top view SEM image of the mesa photodetector. Scale bar corresponds to 50 μm.

3.3 Electrical properties of the nanowire photodetector

The electrical properties of the fabricated mesa photodetectors were first characterized using a cryogenic probe station and a Keithley 2636 source-meter unit. Current voltage curves give important information about the device behavior. This characterization offers a rapid feedback, which allows determination of the possible failures in the nanowire growth and the fabrication process.

Figure 3.5a shows the I-V characteristic of the device at room temperature in the dark. It exhibits a well-defined rectifying behavior characteristic of a p-n junction, with a current turn-on voltage of 1V. The room temperature dark resistance at zero bias is 36 MΩ. The current turn-on voltage is lower than what can be expected for a GaN p-i-n diode (the turn-on voltage should be comparable to the bandgap 3.5V). The reduction of the turn-on voltage in nanostructured photodiodes has already been observed in etched p-i-n GaN nano pillar arrays. This effect has been tentatively attributed to the surface leakage in the junction region (J. L. Pau, Bayram, Giedraitis, McClintock, & Razeghi, 2008). In addition, it should be noted that the p-doping in the p-GaN part can be lower than the nominal value.

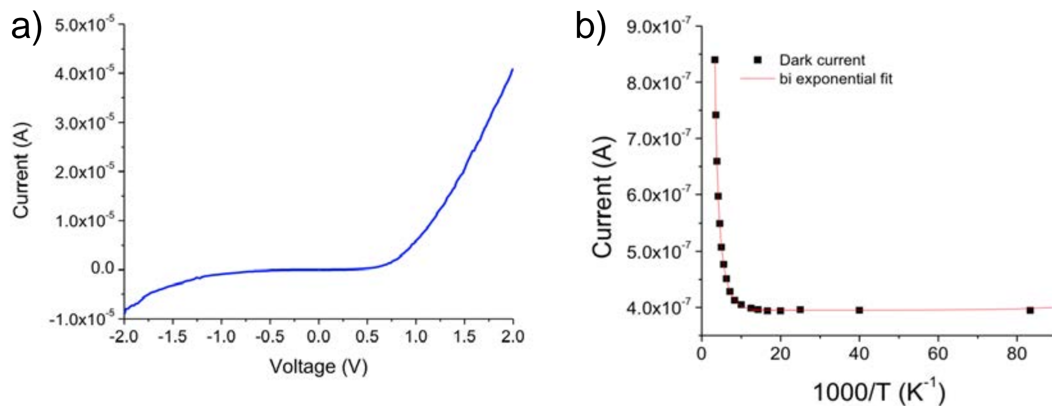

Figure 3.5 a) Room-temperature current-voltage characteristic, b) evolution of the dark current at −1 V with temperature; the black squares represent experimental data, the red curve is a bi-exponential fit.

The reverse leakage current at -1 V is $8x10^{-7}$ A. In thin film p-n diodes, the dark current under reverse bias mainly originates from carrier hopping through defect states in the space charge region, believed to be associated with

dislocations (Kuksenkov, Temkin, A. Osinsky, Gaska, & M. A. Khan, 1998). Since nanowires are dislocation-free structures, we expect a different origin for the leakage current. We attributed the observed current to the conductivity by the nanowire surface states (Y. S. Park et al., 2008). Taking into account the nanowire density, the leakage current per nanowire is ~90 fA at -1V. Transport studies on single p-n junction GaN nanowires report a much higher reverse current per nanowire (~0.3 nA at -1 V (Y. S. Park et al., 2008) and ~80 nA at -1 V (M. Son et al., 2006)). The reduction of the leakage current in our case may be due to the partial passivation of the surface states induced by the HSQ encapsulation.

One way to study electrically active defects is to analyze the activation energy of the leakage current present in the p-i-n junction. In order to obtain information on the energy of generation centers in the depletion region of the photodetector, we have measure the dark current I_D as a function of temperature, where the activation energy is derived from the Arrhenius equation

$$I_D = Ae^{\frac{Ea}{KT}}$$

Here, Ea is the activation energy, k is Boltzmann's constant, A is a proportionality constant and T is the absolute temperature. Figure 3.5b displays the Arrhenius plot illustrating the evolution of the dark current at -1 V bias with temperature. The dependence is well approximated by a bi-exponential fit. The activation energies deduced from the Arrhenius plot are 45 meV and 160 meV, respectively. This exponential dependence implies a thermally activated mechanism of the dark current. Chen et al. have reported a similar activation energy (56 meV) for the temperature-dependent transport in thin homogeneous GaN nanowires (H.-Y. Chen, Chen, et al., 2009), which has been attributed to the activation of deep surface states. This hypothesis of hopping through surface states can also be applied in the present case to the transport in the depleted region of the p-i-n junction. However, we cannot exclude the possibility that the 45 meV activation energy in our case is related to the potential barrier in the conduction band between n-doped GaN nanowire base and n-doped Si substrate. As discussed in the next paragraph, this barrier is predicted to be of the order of 50 meV. The second activation energy of 160 meV could be tentatively attributed to a contribution of a discrete deep level observed in photocurrent deep level optical spectroscopy measurements on GaN n-type nanowires (Armstrong et al. 2009),(Armstrong, Li, Lin, Talin, &

Wang, 2010). It should be noted that we didn't observe an activation energy corresponding to the potential barrier between p-type GaN and the ITO contact, which is expected around 0.8 eV (Su, Juang, & Chen, 2003) probably because it is too high to have an impact in the studied temperature domain.

To understand the electrical and electro-optical behavior or the device, it is important to analyze the band diagram. Figure 3.6 shows a schematic band profile for the p-i-n GaN nanowire and the Si substrate. It should be noted that the band offset between Si and GaN is not well known. The band alignment of two semiconductors across a heterojunction can be estimated by several methods (Kroemer, 2001). The most common approximation to deduce the band offsets is to use the difference between the electron affinities of the two materials. This is often referred to as the electron affinity rule. Based on the electron affinities of Si (4.05 eV) and GaN (4.1 eV) (Arulkumaran, Egawa, Ishikawa, Jimbo, & Umeno, 1998), the conduction band offset between Si and GaN is expected to be small (of the order of 50 meV). This diagram shows that there is almost no potential barrier for photogenerated electrons to be collected by the Si substrate.

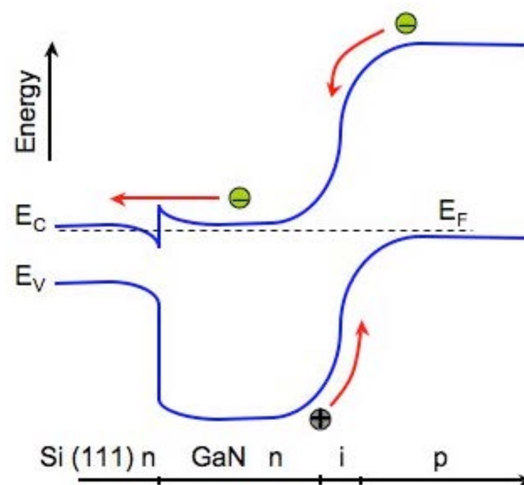

Figure 3.6 Band alignment scheme along the nanowire growth direction.

3.4 Electro-optical response

Under UV illumination, the electron-hole pairs generated in the p-i-n junction are separated by the built-in field and are collected by the top ITO p-contact and the bottom Si n-contact. The room temperature detector responsivity

was calibrated at -1V using UV illumination, an optical fiber source centered at 356 nm and focalized on the mesa, representing an incident power of 1.6μW and a power density of $1.8x10^{-3}$ W/cm^2. The resulting photocurrent is $7.5x10^{-7}$ A, giving the detector responsivity of 0.47 A/W. It should be pointed out that the measured responsivity is higher than that of thin film AlGaN photodiodes (0.1-0.2 A/W) (Monroy et al., 1998)

In order to explore the response of the photodetector device over the whole voltage range, we have carried out electrical measurements under identical UV illumination conditions. Figure 3.7 shows the dark I-V curve at room temperature and the I-Vs under illumination measured at different temperatures. The reverse current increases under illumination by almost two orders of magnitude due to electron-hole pair generation in the p-i-n junction. The I-V curves shift towards positive voltage under illumination as a result of the photovoltage generated in the nanowires. This shift increases at low temperatures following a linear law, which is typical for photovoltaic devices (Al Kuhaimi, 1998). It should be noted that the photovoltage is lower than what can be expected for wide-bandgap semiconductor such as GaN. We attribute this low value to a partial shunting of the nanowires by the surface conduction.

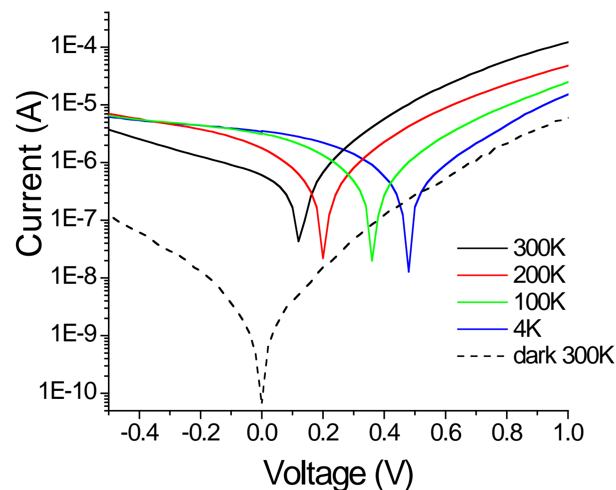

Figure 3.7 Current–voltage characteristics under UV illumination at 300, 200, 100 and 4 K. Dashed lines show the dark I –V and the I –V under illumination at λ=500nm light at RT.

3.5 Operation speed

The speed of a photodetector is limited by two different constraints: first the intrinsic properties of the semiconductor nanowire, in which the speed depends on the carrier recombination time, and second the limitation due to extrinsic properties, such as the series resistance and capacitance of the device.

To characterize the operation speed of the device, RT photocurrent transients were measured by following the detector response to a 60 ms long square light pulse (λ =356 nm) shown in figure 3.8. The photocurrent builds up following a bi-exponential dependence with time constants t_1=2.5 ms and t_2=22 ms. The relaxation after the illumination is stopped also exhibits a bi-exponential decay with characteristic times t_1=6.2 ms and t_2=105 ms. The photodetector -3dB cut off is ~100 Hz. As mentioned in section 3.1, surface related phenomena play a significant role in nanowire properties and in particular affect the operation speed of the nanowire photodetector. The hole trapping/release on the surface states is a slow phenomenon, which explains the characteristic response time in the millisecond to second range. It should be noted that these unwanted surface-related phenomena limiting the operation speed of the nanowire photodetectors can be reduced by a dedicated surface passivation (Simpkins, Mastro, Eddy, & Pehrsson, 2009).

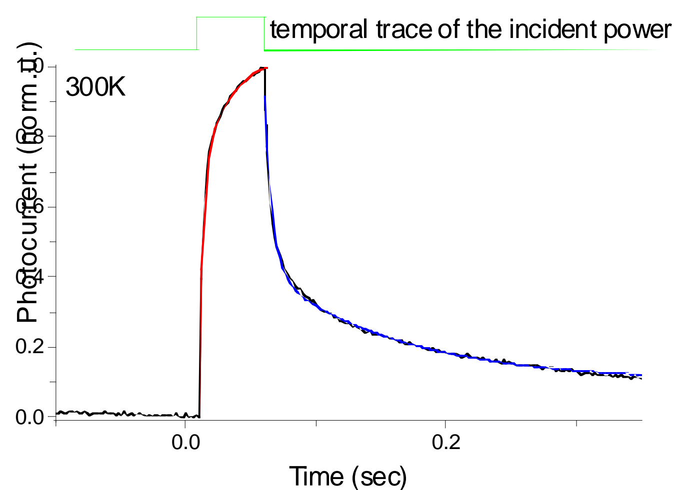

Figure 3.8 Temporal response of the photocurrent.

3.6 Photocurrent spectroscopy

To characterize the spectral response of the device, photocurrent spectroscopy has been performed in the visible to UV range. Photocurrent spectra were recorded by using a tunable vis-UV light source focused on the mesa, consisting of a Xe lamp coupled with a spectrometer. The photocurrent spectrum has been re-normalized to the flux of incident photons, in order to eliminate from the spectrum the features due to the Xe source. This has been done after verifying the linear response of the device under the illumination conditions used during the experiment (see section 3.7)

Photocurrent spectroscopy is a well-known method of optical characterization, giving information about the absorption and the transport from the excited states. The absorption coefficient α is proportional to the joint density of states in the semiconductor that can absorb the light at a specific energy. For direct band gap bulk material, the joint density of states and the absorption coefficient depends on the photon energy E as

$$\alpha \propto \sqrt{E - E_g}$$

where E_g is the semiconductor bandgap. Therefore, for photon energies below the bandgap, there is no absorption and thus the onset of the measured absorption (and photocurrent) is a measurement of the bandgap. In the case of a photoconductor, it is necessary to apply a bias to the sample in order to create an electric field in the material that separates the optically excited electrons and the holes. However, in the case of our p-i-n photodiode the built-in electric field allows to measure the photocurrent without applying any bias voltage (photovoltage effect). We use this effect to measure the photocurrent in a short-circuit configuration.

The spectrum under zero applied bias is shown in Figure 3.9. It presents the following important features. The photocurrent appears at ~3.27 eV and increases by more than two orders of magnitude between 3.3 and 3.4 eV. The resulting rejection ratio between the UV and the visible photocurrent is ~2×10^2. The photocurrent reaches its maximum value at 3.46 eV and then slightly decreases at higher energies. This decrease is due to light absorption in the ITO contact layer, which has good transparency in the near UV range, but starts to absorb at energies higher than 3.5 eV (Leung et al., 2010). The photocurrent onset at an energy slightly lower than the GaN

bandgap (3.27 eV compared with 3.42eV) can be explained by the Franz-Keldysh effect due to the lateral band bending in nanowires (Cavallini et al., 2007). Another interpretation was proposed by Armstrong et al. (Armstrong et al., 2009),(Armstrong et al., 2010) attributing the sub-band-gap onset of the photocurrent to a photoionization of a deep bandgap state.

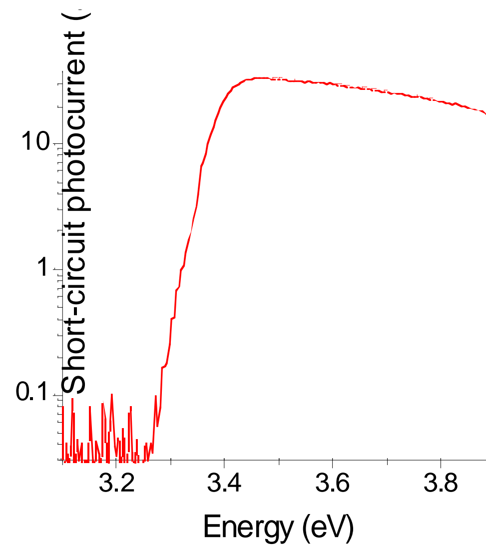

Figure 3.9 RT photocurrent under zero applied bias.

It should be noted that contrary to photodetectors based on ZnO nanowires on Si substrate (Z. Guo et al., 2008), no spectral contribution at the Si bandgap energy was observed neither under direct nor under reverse bias. This demonstrates that the photocurrent in the present device is related to the absorption in the GaN nanowires and not in the substrate. Contrary to the ZnO photodetector (Z. Guo et al., 2008), the potential barrier created by the p-i-n junction prevents the substrate contribution to the photocurrent.

3.7 Dependence on the incident power

Linearity with respect to the incident power is another very important feature for a photodetector. We have studied the signal output of the photodetector as a function of the incident light intensity. Figure 3.10 shows the variation of photocurrent with the incident power. The detector was illuminated with a light-emitting diode at λ=356 nm and the power was changed over four decades using a calibrated attenuator. At power levels lower than 0.6 μW

(corresponding to the power density of $6x10^{-4}$ W/cm^2), the detector response is linear with the incident power. However, at higher power levels, the response deviates from linearity and almost saturates above 10 µW reaching a maximal responsivity of 0.15A/W. The power linearity of the nanowire photodetector is degraded with respect to its thin film counterparts, for which the response is linear up to 0.2 W/cm_2 (Monroy et al., 1998) . This degradation may be due to the photogenerated carrier trapping/release at the nanowire surface.

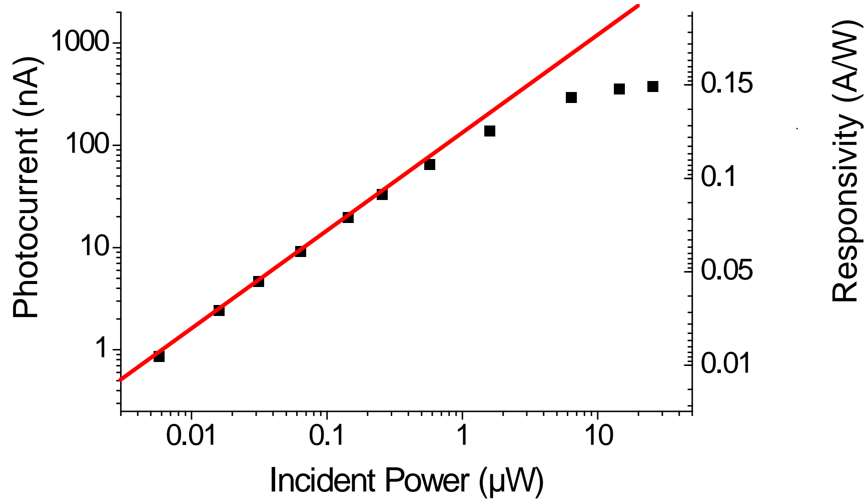

Figure 3.10 RT photocurrent as a function of the incident power.

3.8 Optical Beam Induced Current

Optical beam-Induced Current (OBIC) is a non-invasive optical analysis consisting in scanning a laser beam on the surface of a contacted sample. The locally photogenerated carriers may be collected by the contacts. This procedure generates thus spatially resolved photocurrent images. This technique is commonly used to detect and localize failures on integrated circuits and defects in semiconductors (Wilson, 1987). To probe the surface homogeneity of the photoresponse, we performed OBIC measurements using a UV laser at 244nm focused onto a spot of ~4µm diameter.

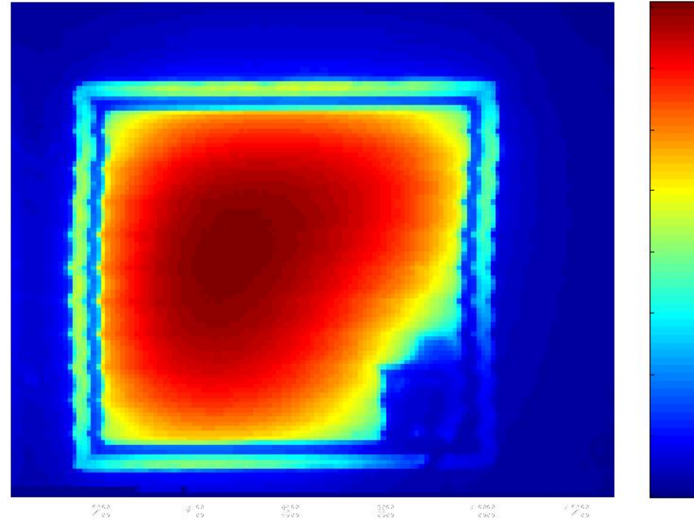

Figure 3.11 OBIC map acquired at V_{bias}= 0. The mesa size is 300x300 μm^2.The scale is linear from 0 to the maximum PC recorded.

Figure 3.11 shows the OBIC map of the mesa. Ti/Au contacts can be easily recognized in the regions of OBIC map where the PC signal drops. We can also note in the bottom left corner of the mesa the area for the wire bonding. The measured photocurrent signal is mostly localized within the central part of the mesa, while a negligible photocurrent signal is generated outside the mesa. This is consistent with the photocurrent spectroscopy, confirming that the photocurrent originates from the absorption in the nanowires and not in the Si substrate. Furthermore, it demonstrates that the nanowire ensemble has a nearly uniform carrier generation capacity and that the ITO contact provides a good current spreading. The OBIC signal is zero outside the mesa.

Conclusions

In this chapter, we have discussed the design, fabrication and characterization of a visible blind UV photodetector based on p–i–n GaN nanowire ensembles on Si(111).

The photodetector shows a peak responsivity of 0.47 A/W at -1V at room temperature exceeding that of thin film AlGaN p-i-n photodetectors and a UV-to-visible rejection ratio of $2x10^2$.

Due to the high density of surface states, a relatively high leakage current of 8.10^{-7} A at -1V was observed. Surface-related phenomena also limit the operation speed of the photodetector (−3 dB cut-off at f =100 Hz), which is, however, still compatible with many UV imaging applications. This situation can be improved by reducing the surface state density using a dedicated passivation. Two approaches can be proposed:

- To apply chemical treatment or to change the filling material. Some works have shown that parylene is a promising candidate to get full surface passivation (W. Guo, Banerjee, Zhang, & Bhattacharya, 2011).

- To grow a large band gap shell around the nanowires (AlGaN shell around GaN nanowires). In this way the surface states are separated by a potential barrier from the charge carriers confined in the core. The core-shell layout also introduces an additional degree of freedom in the design of nanowire devices.

Bibliography

Al Kuhaimi, S. A. (1998). Electron Affinity Difference in CdS/Si Solar Cells. *Japanese Journal of Applied Physics*, *37*(Part 1, No. 9A), 4850-4853. doi:10.1143/JJAP.37.4850

Armstrong, a., Li, Q., Bogart, K. H. a., Lin, Y., Wang, G. T., & Talin, a. a. (2009). Deep level optical spectroscopy of GaN nanorods. *Journal of Applied Physics*, *106*(5), 053712. doi:10.1063/1.3211317

Armstrong, a., Li, Q., Lin, Y., Talin, a. a., & Wang, G. T. (2010). GaN nanowire surface state observed using deep level optical spectroscopy. *Applied Physics Letters*, *96*(16), 163106. doi:10.1063/1.3404182

Arulkumaran, S., Egawa, T., Ishikawa, H., Jimbo, T., & Umeno, M. (1998). interfaces with low interface state density. *Applied Physics Letters*, *73*(6), 809-811.

Caria, M., Barberini, L., Cadeddu, S., Giannattasio, a., Rusani, a., Sesselego, a., Lai, a., et al. (2002). Gallium arsenide photodetectors for imaging in the far ultraviolet region. *Applied Physics Letters*, *81*(8), 1506. doi:10.1063/1.1497996

Cavallini, A., Polenta, L., Stoica, M. R., Calarco, R., Meijers, R. J., Richter, T., & Lth, H. (2007). Franz − Keldysh Effect in GaN Nanowires. *Nano Letters*, *7*(7), 2166-2170. doi:10.1021/nl070954o

Chen, C.-H., Chang, S.-J., Chang, S.-P., Li, M.-J., Chen, I.-C., Hsueh, T.-J., & Hsu, C.-L. (2009). Novel fabrication of UV photodetector based on ZnO nanowire/p-GaN heterojunction. *Chemical Physics Letters*, *476*(1-3), 69-72. doi:10.1016/j.cplett.2009.06.007

Chen, H.-Y., Chen, R.-S., Chang, F.-C., Chen, L.-C., Chen, K.-H., & Yang, Y.-J. (2009). Size-dependent photoconductivity and dark conductivity of m-axial GaN nanowires with small critical diameter. *Applied Physics Letters*, *95*(14), 143123. doi:10.1063/1.3213556

Chen, R.-S., Chen, H.-Y., Lu, C.-Y., Chen, K.-H., Chen, C.-P., Chen, L.-C., & Yang, Y.-J. (2007). Ultrahigh photocurrent gain in m-axial GaN nanowires. *Applied Physics Letters*, *91*(22), 223106. doi:10.1063/1.2817595

Guo, W., Banerjee, A., Zhang, M., & Bhattacharya, P. (2011). Barrier height of Pt–In[sub x]Ga[sub 1−x]N (0≤x≤0.5) nanowire Schottky diodes. *Applied Physics Letters*, *98*(18), 183116. doi:10.1063/1.3579143

Guo, Z., Zhao, D., Liu, Y., Shen, D., Zhang, J., & Li, B. (2008). Visible and ultraviolet light alternative photodetector based on ZnO nanowire/n-Si heterojunction. *Applied Physics Letters*, *93*(16), 163501. doi:10.1063/1.3003877

Kroemer, H. (2001). Nobel Lecture : Quasielectric fields and band offsets : teaching electrons new tricks *. *Rca Review*, *73*(July).

Kuksenkov, D. V., Temkin, H., Osinsky, a., Gaska, R., & Khan, M. a. (1998). Low-frequency noise and performance of GaN p-n junction photodetectors. *Journal of Applied Physics*, *83*(4), 2142. doi:10.1063/1.366950

Leung, Y. H., He, Z. B., Luo, L. B., Tsang, C. H. a., Wong, N. B., Zhang, W. J., & Lee, S. T. (2010). ZnO nanowires array p-n homojunction and its application as a visible-blind ultraviolet photodetector. *Applied Physics Letters*, *96*(5), 053102. doi:10.1063/1.3299269

Martens, M., Schlegel, J., Vogt, P., Brunner, F., Lossy, R., Würfl, J., Weyers, M., et al. (2011). High gain ultraviolet photodetectors based on AlGaN/GaN heterostructures for optical switching. *Applied Physics Letters*, *98*(21), 211114. doi:10.1063/1.3595303

Monroy, E., Calle, F., Pau, J. L., Muñoz, E., Omnès, F., Beaumont, B., & Gibart, P. (2001). AlGaN-based UV photodetectors. *Journal of Crystal Growth*, *230*(3-4), 537-543. doi:10.1016/S0022-0248(01)01305-7

Monroy, E., Calle, F., Pau, J. L., Sánchez, F. J., Muñoz, E., Omnès, F., Beaumont, B., et al. (2000). Analysis and modeling of Al[sub x]Ga[sub 1−x]N-based Schottky barrier photodiodes. *Journal of Applied Physics*, *88*(4), 2081. doi:10.1063/1.1305838

Monroy, E., Hamilton, M., Walker, D., Kung, P., Sánchez, F. J., & Razeghi, M. (1999). High-quality visible-blind AlGaN p-i-n photodiodes. *Applied Physics Letters*, *74*(8), 1171. doi:10.1063/1.123960

Monroy, E., Muñoz, E., Sánchez, F. J., Calle, F., Calleja, E., Beaumont, B., Gibart, P., et al. (1998). High-performance GaN p-n junction photodetectors for solar ultraviolet applications. *Semiconductor Science and Technology*, *13*(9), 1042-1046. doi:10.1088/0268-1242/13/9/013

Muñoz, Elías. (2007). (Al,In,Ga)N-based photodetectors. Some materials issues. *Physica Status Solidi (B)*, *244*(8), 2859-2877. doi:10.1002/pssb.200675618

Osinsky, A., Gangopadhyay, S., Gaska, R., Williams, B., & Khan, M. A. (1997). p- -n. *October*, *71*(October), 2334-2336.

Palacios, T., Monroy, E., Calle, F., & Omnès, F. (2002). High-responsivity submicron metal-semiconductor-metal ultraviolet detectors. *Applied Physics Letters*, *81*(10), 1902. doi:10.1063/1.1504492

Park, Y. S., Park, C. M., Lee, J. W., Cho, H. Y., Kang, T. W., Yoo, K.-H., Son, M.-S., et al. (2008). Electrical transport properties of a nanorod GaN p-n homojunction grown by molecular-beam epitaxy. *Journal of Applied Physics*, *103*(6), 066107. doi:10.1063/1.2896636

Pau, Jose Luis, Anduaga, J., Rivera, C., Navarro, A., Alava, I., Redondo, M., & Muñoz, E. (2006). Optical sensors based on III-nitride photodetectors for flame sensing and combustion monitoring. *Applied optics*, *45*(28), 7498-503. Retrieved from http://www.ncbi.nlm.nih.gov/pubmed/16983439

Pau, J. L., Bayram, C., Giedraitis, P., McClintock, R., & Razeghi, M. (2008). GaN nanostructured p-i-n photodiodes. *Applied Physics Letters*, *93*(22), 221104. doi:10.1063/1.3041641

Pau, J., Monroy, E., Sanchezgarcia, M., Calleja, E., & Munoz, E. (2002). AlGaN ultraviolet photodetectors grown by molecular beam epitaxy on Si(111) substrates. *Materials Science and Engineering B*, *93*(1-3), 159-162. doi:10.1016/S0921-5107(02)00051-X

Simpkins, B. S., Mastro, M. a., Eddy, C. R., & Pehrsson, P. E. (2009). Surface-Induced Transients in Gallium Nitride Nanowires. *The Journal of Physical Chemistry C*, *113*(22), 9480-9485. doi:10.1021/jp901122k

Soci, C., Zhang, a, Xiang, B., Dayeh, S. a, Aplin, D. P. R., Park, J., Bao, X. Y., et al. (2007). ZnO nanowire UV photodetectors with high internal gain. *Nano letters*, *7*(4), 1003-9. doi:10.1021/nl070111x

Son, M., Im, S., Park, Y., Park, C., Kang, T., & Yoo, K. (2006). Ultraviolet photodetector based on single GaN nanorod p–n junctions. *Materials Science and Engineering: C*, *26*(5-7), 886-888. doi:10.1016/j.msec.2005.09.089

Stanislav I. Soloviev, Alexey V. Vert, Jody A. Fronheiser, P. M. S. (2009). Solar-Blind 4H-SiC Avalanche Photodiodes. *Materials Science Forum*, *615-617*, 873-876. doi:10.4028/www.scientific.net/MSF.615-617.873

Stevens, K. S., Kinniburgh, M., & Beresford, R. (1995). Photoconductive ultraviolet sensor using Mg-doped GaN on Si(111). *Applied Physics Letters*, *66*(25), 3518. doi:10.1063/1.113783

Su, Y.-K., Juang, F.-S., & Chen, M.-H. (2003). GaN Metal-Semiconductor-Metal Visible-Blind Photodetectors with Transparent Indium-Tin-Oxide Contact Electrodes. *Japanese Journal of Applied Physics*, *42*(Part 1, No. 4B), 2257-2259. doi:10.1143/JJAP.42.2257

Tang, Y. B., Chen, Z. H., Song, H. S., Lee, C. S., Cong, H. T., Cheng, H. M., Zhang, W. J., et al. (2008). Vertically aligned p-type single-crystalline GaN nanorod arrays on n-type Si for heterojunction photovoltaic cells. *Nano letters*, *8*(12), 4191-5. doi:10.1021/nl801728d

Wilson, T., & McCabe, E. M. (1987). Theory of optical beam induced current images of defects in semiconductors. *Journal of Applied Physics*, *61*(1), 191. doi:10.1063/1.338853

Zgórka, G., & Kawka, S. (2001). Application of conventional UV, photodiode array (PDA) and fluorescence (FL) detection to analysis of phenolic acids in plant material and pharmaceutical preparations. *Journal of pharmaceutical and biomedical analysis*, *24*(5-6), 1065-72. Retrieved from http://www.ncbi.nlm.nih.gov/pubmed/11248502

4. GaN/AlN single nanowire photodetectors

In this chapter I present the study of single-wire UV photodetectors based on GaN/AlN quantum discs embedded in single nanowires and compare them to a GaN binary sample. Two different QDisc structures have been studied. These differ by the QDisc thickness and by the presence of a lateral GaN shell formed during the growth and surrounding the QDisc region. The presence of the lateral shell is evidenced by means of TEM and HAADF STEM characterizations. Spectral contributions above and below the GaN bandgap originating from QDiscs are revealed by PL experiments and confirmed by the spatially resolved cathodoluminescence experiments. The dependence of the emission energy on the QDisc thickness evidences the presence of an electric field inside the QDiscs, giving rise to the quantum-confined Stark effect. Then an electrical transport study was carried out that revealed a significant influence of environmental conditions on the nanowire conduction in the case of nanowires surrounded by a GaN shell. The conduction measurements showed a reproducible negative differential resistance in nanowires where the GaN shell was absent. Finally, the spectral range of operation of the photodetector is studied by means of photocurrent spectroscopy revealing a sub-band-gap peak attributed to the hh1-e1 absorption in the large QDiscs.

Introduction

As pointed out in the previous chapter, III-V semiconductor nanowires are promising materials for light detection. Numerous studies have focused on the photoconduction properties of single GaN and ZnO nanowires where the high surface-to-volume ratio has a strong impact on the wire photoconduction(Soci, 2007)(R.-S. Chen , 2007). Due to the Fermi level pinning, the bands bend towards the lateral surface and create a region depleted of electrons. The extension of the depleted region changes the nanowire conduction. The band bending also induces a Franz-Keldysh effect responsible for sub-band-gap photocurrent in binary GaN nanowires (Cavallini, 2007) Moreover, the same band bending causes a physical separation of electrons and holes, leading to a significant enhancement of the photoconductive gain. All these studies have been focused on binary materials, contrary to the results presented in this chapter.

The possibility of including quantum disc heterostructures in GaN nanowire has been demonstrated by different authors (Ristić, 2003)(Kikuchi,2004), opening new prospects for quantum devices. Especially for photodetection applications, heterostructure systems enable the possibility to cover a wide spectral range by making use of the interband and intersubband absorptions in the quantum discs.

4.1 Nanowire structure

The operation principle of the nanowire photodetector is illustrated in Fig. 4.1. The photodetector consists of an n–i–n structure, where the isolating region corresponds to the n-doped GaN/AlN QDiscs. When the nanowire is exposed to UV illumination, carriers are generated in the QDiscs. The polarization discontinuity between GaN and AlN results in a fixed charge density at the heterostructure interfaces. This charge density will thus generate an internal electric field and also induce a band bending along the axial direction in the QDisc region. The presence of band bending helps extracting photogenerated carriers from the QDiscs. In addition, the presence of the GaN/AlN heterostructure is expected to lower the dark current with respect to a photodetector based on a homogeneous GaN nanowire.

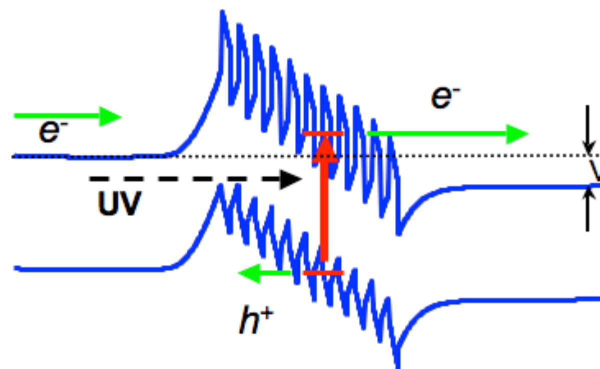

Figure 4.1 Operation principle of a single nanowire photodetector containing AlN/GaN QDiscs.

The studied nanowires were grown by radio frequency plasma-assisted molecular beam epitaxy (PA-MBE). The nanowire growth was performed by R. Songmuang at CEA Grenoble. Two heterostructured nanowire samples containing QDiscs of different thickness were analyzed and compared to a reference binary n-i-n GaN nanowire sample. The sample structures and STEM images are shown in figure 4.2.

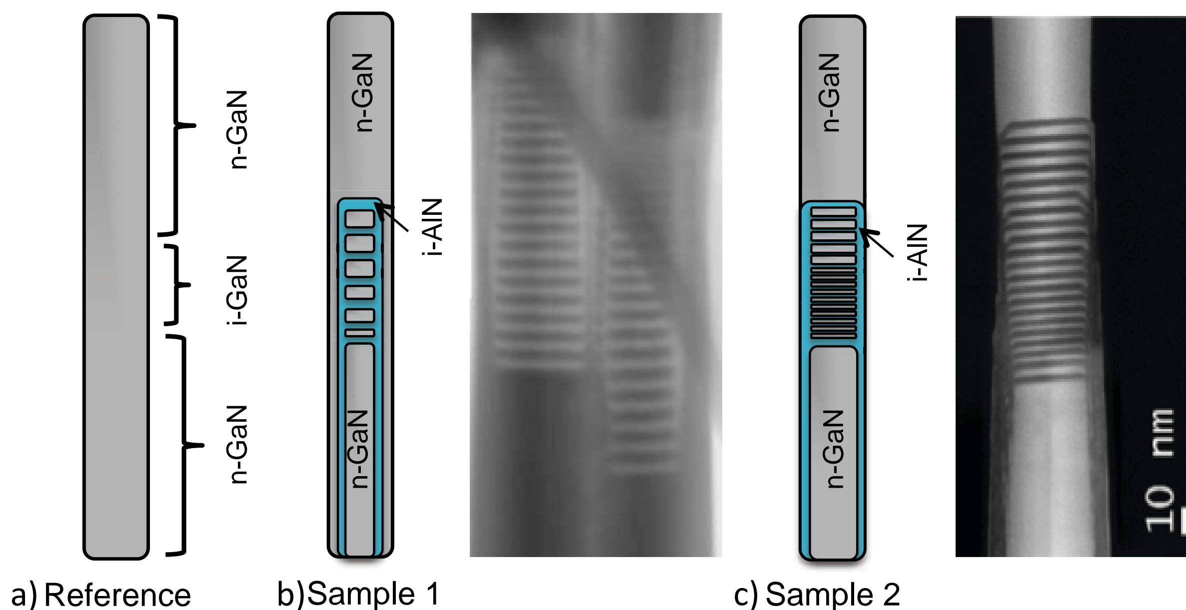

Figure 4.2. Schematic representation of the three samples and STEM images of nanowires from E1857 and E1862.

Catalyst-free GaN nanowires were grown on Si(111) substrates under N-rich atmosphere at 790 °C. The nanowire length is approximately 1.2 μm and the diameter is 25-80 nm. For heterostructure nanowires, a stack of 20 AlN/GaN QDiscs was inserted in the middle of Si-doped GaN nanowires, as schematically shown in Figure 4.2. Quantum discs were formed by switching from Ga to Al flux without any growth interruption. The reference sample containing n-i-n GaN binary nanowires was grown using similar conditions; the length of the nominally undoped segment is 100 nm.

The STEM analyses (Figure 4.2 b,c) show that the thickness of AlN barriers is 2-3 nm for both samples and the QDisc thickness varies from 3-5 nm in the case of E1857 and 1-3 nm for E1862. STEM images reveal an inhomogeneity of QDiscs thickness along the wire, which tends to increase progressively toward the nanowire top. An AlN shell of about 5-10 nm is formed around the lower nanowire part due to lateral growth (Tchernycheva, 2007).

For E1857, an additional GaN shell of 5-15 nm surrounding the QDisc region and the lower nanowire part was formed (Figure 4.2b). The formation of the GaN shell was avoided in E1862 (Figure 4.2c) by increasing the growth temperature by 20 °C during the deposition of the GaN cap. Previous studies performed on MBE-grown GaN nanowires have shown that the lateral growth can be reduced by increasing the substrate temperature (Meijers, 2006). It should be noted, however, that the formation of the lateral GaN shell depends on the diffusion

of Ga adatoms, which is affected not only by the growth temperature but also by the strain state of the underlying AlN layer. Detailed investigations of the growth conditions allowing control of the lateral growth of GaN are underway in CEA Grenoble.

4.2 Micro photoluminescence spectroscopy

The optical properties of the three samples described above were first characterized by photoluminescence spectroscopy (PL). This non-destructive method provides information on the electronic structure of the material. In the present set of photoluminescence experiments, electrons and holes are created by an optical excitation at a photon energy above the GaN bandgap. The optically generated electrons and holes rapidly thermalize and relax to the band edges. The charge carriers can diffuse in the nanowire and are captured by the QDiscs. The PL energy depends on the internal electric field and on the thickness of the Qdiscs in the nanowires. In this way, we can study and determine the presence of the Qdiscs embedded in the nanowires and compare the results with those from structural characterization (STEM, TEM).

For PL measurements, samples were placed in a liquid He cooled cryostat mounted on an x-y-z stage. The excitation was provided with a continuous wave frequency-doubled Ar2+ laser (λ =244 nm) focused on the sample, with a spot size of ~3um. The luminescence signal was collected by the microscope objective, filtered to remove the scattered laser light and injected in a Jobin Yvon HR460 spectrometer equipped with a CCD camera. An additional camera was used to image the sample and to locate single nanowires by their luminescence spot.

Nanowire ensembles

The PL spectra of the nanowire ensembles of the reference sample and the heterostructured samples E1857 and E1862 are shown in figure 4.3. The measurements were performed at room temperature with an excitation at normal incidence onto the substrate. The main peak at 3.41 eV observed in all samples corresponds to the GaN near band edge (NBE) emission at 300 K. For E1857 a broad peak is present between 2.75 and 2.9 eV, while the spectra from E1862 shows a peak centered at 3.19 eV. Both samples show low-energy peaks below the band gap that are attributable to the embedded QDiscs. The difference in the peak energy can be explained by the thickness of the QDiscs in each sample. The spectral shift of the QDisc peaks below the GaN bandgap demonstrates the presence of the quantum-confined Stark effect (QCSE) due to the internal field in the QDiscs. However, as mentioned above, the excitation of the nanowire ensembles and the collection of the PL signal are perpendicular to the substrate. In this geometry the upper GaN part of the nanowires absorbs most of the laser excitation and also the spectral contribution of the luminescence with energy above the GaN bandgap originating from thin QDiscs. As a result, only the GaN near-band edge and the thick QDisc produce a significant PL signal.

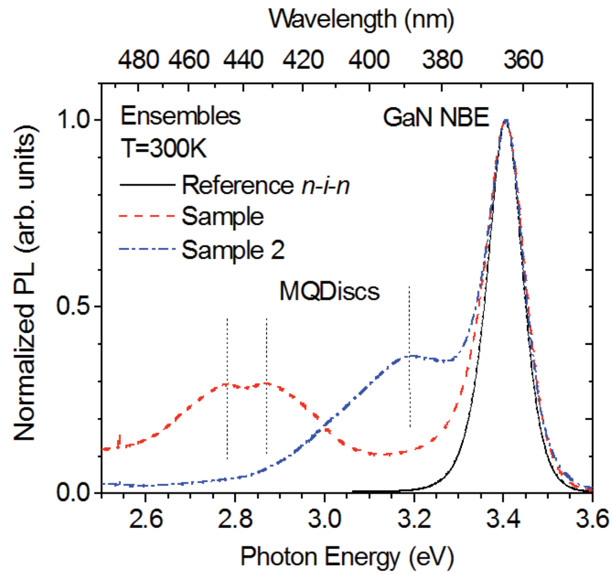

Figure 4.3 Room temperature PL spectra of the nanowire ensembles of the three samples: reference n-i-n sample (black solid line), E1857 (red dashed line) and E1862 (blue dash-dotted line).

Single nanowire photoluminescence

For micro-photoluminescence experiments on single nanowires, the nanowires were removed from their native substrate by ultrasonic bath in ethanol and dispersed on a SiO_2 substrate. Both the excitation and collection are perpendicular to the nanowire axis. This configuration facilitates the observation of high-energy contributions from the QDiscs. The low-temperature PL of single nanowires is shown in figures 4.4a (left) and 4.4b (right). In both cases the emission is broad as a consequence of the high doping level and of the inhomogeneous strain distribution. The samples show a main peak located at E=3.53-3.58 eV. This peak is attributed to the GaN near-band edge (NBE) emission. Its energy shift with respect to the PL energy of relaxed GaN (E=3.478 eV) can be explained by the presence of a surrounding AlN shell that produces a compressive strain on the GaN core of the lower part of the wire (Rigutti, 2011).

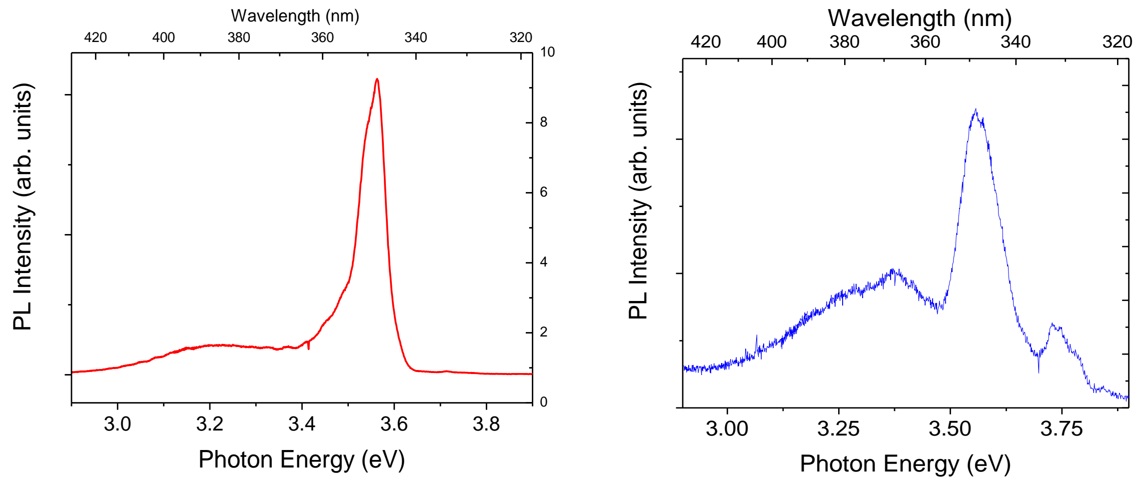

Figure 4.4 Micro-PL spectra from individual nanowires from E1857 (left) and E1862 (right) at 4K. Both samples show a contribution under the band gap attributed to the presence of QDiscs, however, E1862 has also a high-energy peak possibly related to thin QDiscs.

A sub-band-gap contribution is present in both spectra and can be ascribed to the emission from QDiscs as in the case of the ensembles. However, spectra from E1862 exhibit an additional above-band-gap contribution related to the emission of thinner QDiscs. The dependence of the emission energy of GaN/AlN QDiscs on the QDisc thickness is the consequence of the quantum-confined Stark effect, as reported previously (Julien Renard, 2008). Finally, it should be noted that the low-energy peak emission overlaps with the energy typical for donor-acceptor (DAP) luminescence. Nevertheless, the PL peak energy decreases from E1857 to E1862, thereby ruling out the attribution of the PL peak to DAP transitions.

4.3 Cathodoluminescence

Although photoluminescence has proven to be a sensitive technique for the study of quantum semiconductor structures, the lack of spatial resolution limits the assignment of optical transitions related to individual nanostructures (QDiscs). Cathodoluminescence (CL) is an alternative approach that relies on the detection of radiation emitted when a sample is excited by an electron beam. This technique has been extensively used to study the luminescence of semiconductors (Jain, 2000).

A precise control of the size (as small as several nanometers) and position of the electronic beam in the electron microscope allows acquiring a CL spectrum from a nanoscale region. For this technique the spatial resolution is determined by the diffusion of excess carriers in the material; it is not limited by diffraction in the collection and excitation optics as in the PL experiments. Additionally, the use of CL in scanning transmission electron microscopy offers the advantage of enabling the direct correlation of optical properties with the morphology of the heterostructures.

The CL characterization was carried out in order to clearly identify the spectral contribution of the QDiscs embedded in the nanowires and in order to support photoluminescence data. The measurements were made in collaboration with the group of M. Kociak at the Laboratoire de Physique des Solides (LPS) and performed by Luiz F. Zagonel. CL experiments were performed in a custom-made optimized set-up mounted in a Scanning Transmission Electron Microscope (VG-STEM) HB-501. In this STEM system, an electron source focused on a sample interacts with it both quasi-elastically (giving rise to the High Angle Annular Dark Field (HAADF) signal) and inelastically (giving rise to the CL signal). During the experiment, the sample temperature was kept at about 150 K by the use of a liquid nitrogen cooled sample stage. The stage induces small drifts (typically of about 1 nm per minute), which need to be accounted for in the image treatment.

The results of the CL measurements are shown in figure 4.5. The HAADF image is acquired simultaneously with the CL specrum-image giving access to the main optical properties (peak energy, intensity, full width at half maximum). It can be seen that the nanowire GaN end surrounded by the AlN shell (left part) emits strongly at 346.6 nm. This wavelength is slightly smaller than the bulk GaN emission wavelength. The AlN-free GaN side (right part) of the nanowire has a much weaker signal with an energy corresponding to the value reported in the literature for the near band edge line at 150K both in GaN epitaxial layers and in binary GaN nanowire ensembles (Furtmayr, 2008). The slight blue shift of the NBE in the GaN end surrounded by AlN is attributed to the compressive strain (Chuang & Chang, 1996) exerted by the AlN shell, as discussed before in PL results (Rigutti, 2011).

a)

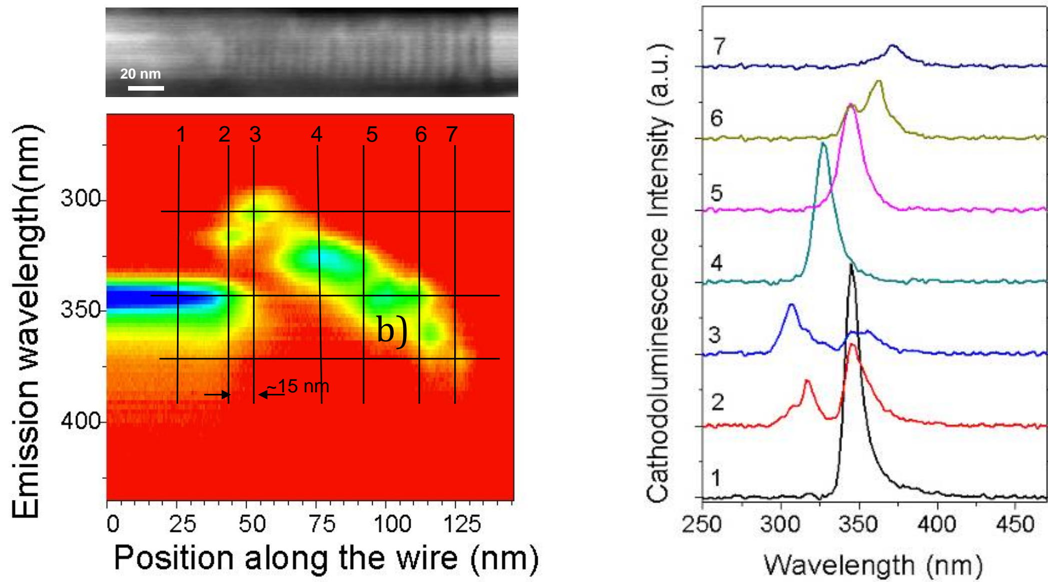

Figure 4.5 Spectral imaging of a GaN/AlN NW with 20 QDiscs. (a) Top -- the HAADF image of a GaN/AlN nanowire (scale bar is 20 nm). Bottom -- CL spectral mapping of the E1862 nanowire. (b) CL spectra recorded from the seven points of the 2D map.

Figure 4.5a bottom shows a 2D CL map combining the spatial and spectral information. The CL map can be easily related to the position within the QDisc structure through the HAAF image (fig 4.5 a top) acquired simultaneously with the CL spectra. Figure 4.5b present the CL spectra recorded from 7 points of the map starting from the GaN surrounded by the AlN shell (1), passing through the QDiscs region (2-6) and ending with the unstrained bulk GaN (7). The general tendency is that as the QDisc thickness increases (from the bottom towards the top) so does its emission wavelength. It is seen that the strained GaN (position 1) emits at a shorter wavelength (346.6 nm) than the shell-free GaN (position 7). This spectral shift is due to the compressive strain exerted by the AlN shell as discussed before.

4.4 Electronic transport

The study of electronic transport properties of nanowires is important for nanowire characterization, electronic device applications, and the investigation of unusual transport phenomena arising from one-dimensional quantum effects. Conductivity of binary GaN single nanowires has been the object of many studies (Polenta, 2008)(Calarco, 2005)(Sanford, 2010). It has been pointed out that the nanowire surface has a strong impact on the effective conduction cross-section. Due to the Fermi level pinning, the bands bend close to the lateral surface and create a region depleted of electrons. If the depleted region becomes comparable with the nanowire diameter, the wire resistance drastically increases. The thickness variation of the depletion region has a strong impact on wire conductivity (B. S. Simpkins, 2008). All the above-mentioned conductivity studies have focused on binary GaN nanowires. In this section I present the results of an extensive electrical characterization of GaN nanowires containing GaN/AlN quantum discs.

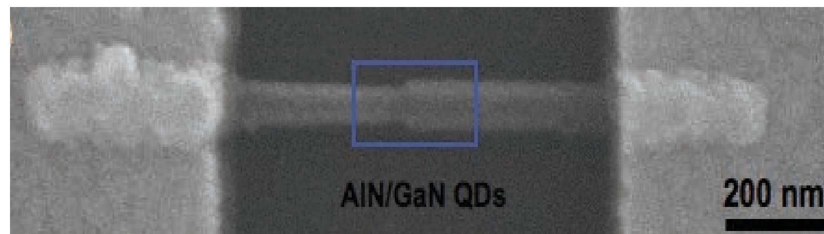

Figure 4.6 (a) SEM image of a single nanowire contacted by e-beam lithography leaving the AlN/GaN QDiscs free for light excitation.

In order to fabricate single nanowire photodetectors and to carry out transport studies, several nanowires from the three samples were contacted by e-beam lithography using techniques described in chapter 2. To reduce the dispersion related to nanowire diameter, nanowires with a diameter in the range of 40 to 60 nm were selected. An ohmic metallization was deposited on the nanowire doped extremities leaving the QDisc region unmetallized. Figure 4.6 displays a scanning electron microscopy image of a single contacted nanowire. The nanowire current–voltage characteristics were tested using a cryogenic probe station and a Keithley 2636 source-meter unit. The I–V characteristics of single nanowires from the reference sample and from the two heterostructured samples are shown in figure 4.7.

The nanowire resistance of the three studied samples is very different. It should be noted that in samples containing QDiscs, the I–V curves are asymmetric with respect to the bias sign, especially in E1862. This asymmetry can be due to the presence of the QDisc region. In addition, in E1862 the contact on the base side of the nanowire is deposited on the AlN shell, therefore, the contact can have a Schottky behavior increasing the asymmetry of the I-V curve.

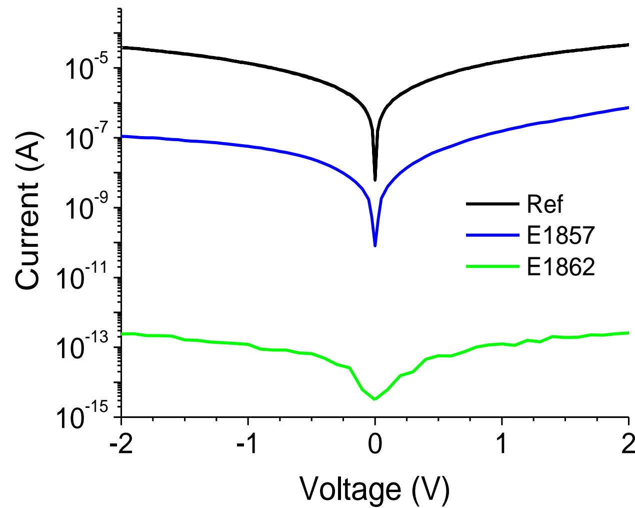

Figure 4.7 The I –V characteristics at T = 300 K in ambient atmosphere of a nanowire from the reference sample with nanowire diameter dNW = 50 nm (black line), from E1857 with dNW = 55 nm (blue line), and from E1862 with dNW = 60 nm (green line).

While the reference n-i-n sample presents a small resistance at zero bias Ro ~ 0.4 x 10^5 Ω, the resistance of nanowires of E1857 increases to ~3±1 x10^7 Ω and gets even larger in the case of E1862 ~ 1 x10^{12} Ω. In case of the reference sample, as expected in binary GaN nanowires, the conduction takes place through the entire nanowire cross-section except for a narrow depletion region close to the lateral surface (Calarco, 2005). On the other hand, for samples E1857 and E1862, the increase of the resistance is related to the presence of the QDisc heterostructure. In nanowires from E1857, the heterostructure only partially blocks the current because of the presence of the surrounding GaN shell. However, the GaN shell is absent in E1862 and the current is forced to flow through the multiple AlN barriers, which drastically increases the resistance.

4.4.1 Influence of environmental conditions

Because of the enhanced surface to volume ratio of nanowires, their transport behavior may be modified by changing their environmental conditions. The samples were characterized by comparing the conduction in vacuum (< 10^{-4} mbar) and in ambient atmosphere. The I–V curves for nanowires from the three samples are displayed in figure 4.8. It can be seen from the conduction measurements made in air/vacuum that nanowires from E1857 present a higher sensitivity to the environmental conditions than those from the reference sample and from E1862. When going from ambient pressure to vacuum, the current only slightly increases for the reference sample but changes significantly in E1857 (a factor of 6.6 at 3 V). Interestingly, nanowires from E1862 exhibit the opposite behavior, as their conductivity in vacuum decreases with respect to their conductivity in air (by a factor of 1.3 at 3 V).

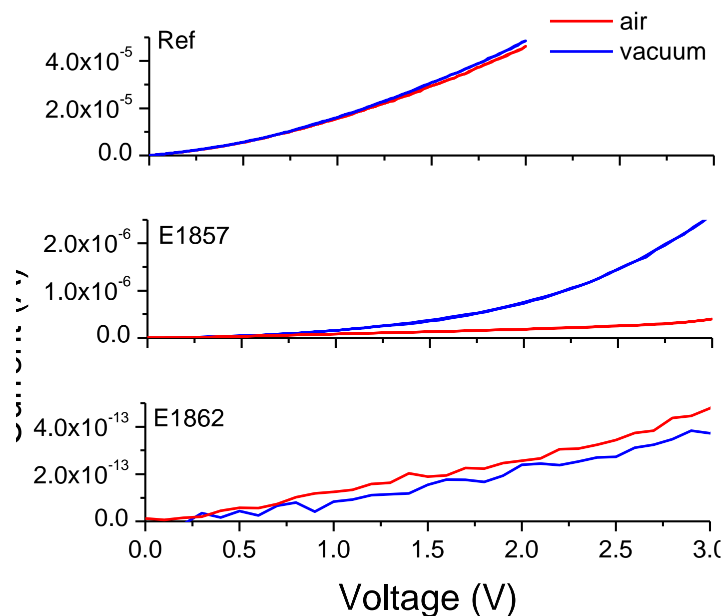

Figure 4.8 The dark I –V curves at RT in vacuum (blue line) and in air (red line) for a single wire from a reference sample (nanowire diameter dNW = 50 nm), E1857 sample (dNW = 55 nm), and E1862 sample (dNW = 60 nm).

The response to the environmental conditions can be understood in terms of the nanowire structure. It has been pointed out for ZnO nanowires (Soci, 2007) that the presence of adsorbed negative oxygen molecules on the nanowire surface increases the depletion region close to the nanowire sidewalls. These molecules are desorbed in vacuum, the depletion region is reduced and the conductivity increases. Similar effects of modulation of the surface depletion region by adsorbates are expected in GaN nanowires.

In the reference sample this effect is relatively weak because the conduction takes place almost through the whole nanowire cross-section. On the contrary, in E1857 as described above, the insertion of QDiscs blocks the current through the central part and the conduction is mainly restricted to the outer GaN shell. In this case the variation of the depletion width has a stronger impact on the nanowire resistance. Furthermore, electron transport can be efficiently confined close to the nanowire surface by using a core–shell heterostructure.

In E1862 there is no GaN shell, the conduction takes place by tunneling through the AlN multiple barriers and the resistance of the QDisc region governs the total nanowire resistance. In this case the lateral surface is partly covered not by GaN but by AlN, which probably has a different interaction with the adsorbates and also modifies the lateral band profile.

4.4.2 Resonant tunneling

III-nitrides are excellent candidates for the fabrication of high temperature THz quantum cascade lasers (QCLs) thanks to their high LO phonon energy (92 meV in GaN) (Bellotti, 2009). This application requires a precise control of vertical transport in III-nitride heterostructures necessary for the fabrication of injector/extractor regions. Tunneling effects and intersubband absorption in AlN/GaN superlattices or double-barrier structures have been the subject of many investigations (Baumann, 2005)(Hofstetter, 2009). However, the results of the transport studies are either controversial or irreproducible (Vashaei, 2010). This is attributed to the presence of a large density of threading dislocations in the 2D nitride layers grown on lattice-mismatched substrates. These dislocations degrade the optical emission efficiency in light-emitting devices and also act as deep traps (Klein, 2003) and parasitic conduction channels (Hsu, 2002) in intersubband devices relying on vertical transport. The I–V measurements of 2D resonant tunneling diodes show bistability and current hysteresis, with a negative differential resistance disappearing during the backward sweep of the I –V curve (Golka, 2006)(Sakr, 2011).

As the conduction of nanowires from E1862 takes place through the QDisc region, it allows for the observation of tunneling-related features. Figure 4.9 shows the I–V curves measured at different temperatures for a nanowire from E1862. A negative differential resistance (NDR) is observed for positive bias at temperatures below 250 K. The peak is perfectly reproducible, appearing both during the forward and the backward I–V sweep, and is independent of the measurement speed. The peak-to-valley ratio for the studied nanowires varies from 1.1 to 1.75. Finally, there is almost no hysteresis loop between the forward and backward sweeps.

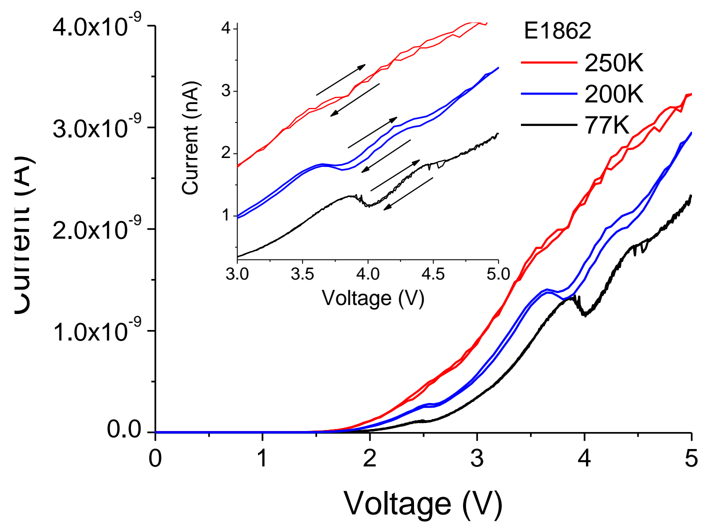

Figure 4.9 The I-V curves of a nanowire from E1862 at T=77K (black line), T=200K (blue line) and T=280K (red line). The inset shows a close-up of the NDR region (curves are vertically shifted for clarity).

The variation of the peak-to-valley ratio with temperature is shown in figure 4.10. With increasing temperature, the peak-to-valley ratio decreases from the maximum value of 1.19 at T=100 K and the NDR is no longer visible for T > 250 K. The position of the peak gradually shifts from 3.83 V at T =77 K to 3.63 V at T = 250 K. When the temperature is increased, the tunneling transport mechanism competes with other thermally activated mechanisms, which increase the background conductivity. The reduction of the peak-to-valley ratio and the disappearance of NDR above 250 K can be related to the electron–LO phonon interaction destroying the coherent transport.

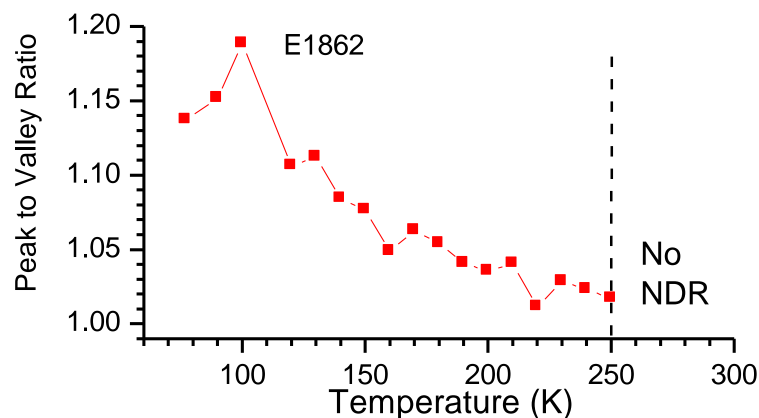

Figure 4.10. The evolution of the peak-to-valley ratio in E1862 with temperature

The observed reproducible NDR represents a demonstration of tunneling transport through the GaN/AlN QDisc structure. However, the interpretation of the NDR remains difficult because of the complexity of the structure. Most likely, tunneling occurs through a subset of AlN barriers at the top part of the heterostructure with the creation of electric field domains within the multi-QDisc system (Kwok, 1994).

Contrary to the observations by Chu et al (Chu, 2009) the binary nanowires from the reference sample do not show any NDR. The TEM studies of the nanowire structure have revealed a perfect wurtzite crystalline structure with no stacking faults so that the defect-related tunneling mechanism proposed by these authors cannot take place in our samples. The nanowires from E1857 do not show any NDR in the studied temperature range. This can be explained by the current leakage through the lateral GaN shell that masks the tunneling current. It should be pointed out that the NDR was observed on only 25% of the studied nanowires from sample E1862 due to the morphology variation of the wires.

4.5 Optical response and photocurrent spectroscopy

To explore the photoresponse of the nanowire devices, we carried out electrical measurements under UV illumination. The measurements have been carried out on several nanowires from each sample. In the following, we show the results from representative single-nanowire devices. Figure 4.11 shows the dark I-V characteristics and the I-Vs under UV illumination at λ=300 nm with a power density of 5 mW/cm^2. The reference n-i-n sample shows only a weak dependence on the illumination. Its photosensitivity factor at -1 V (defined as a ratio of photocurrent over the dark current) is only I_{ph}/I_{dark}=0.05. The photosensitivity factor increases in E1857 to I_{ph}/I_{dark}~ 2 and in E1862 it reaches 5x10^2. In E1857, the generated photocurrent has the same order of magnitude as the dark current (1.7 x10^{-7}A). It could be related to the carrier generation in the QDiscs but also in the outer GaN shell and in the GaN extremities. In nanowires from E1862 the photocurrent is about two orders of magnitude higher than the dark current (5.2 x 10^{-14}A), which illustrates the efficiency of the heterostructures as an electron a dark current blocking layer. Finally, it should be noted that for all samples the illumination with visible light (λ=500 nm) does not produce photocurrent.

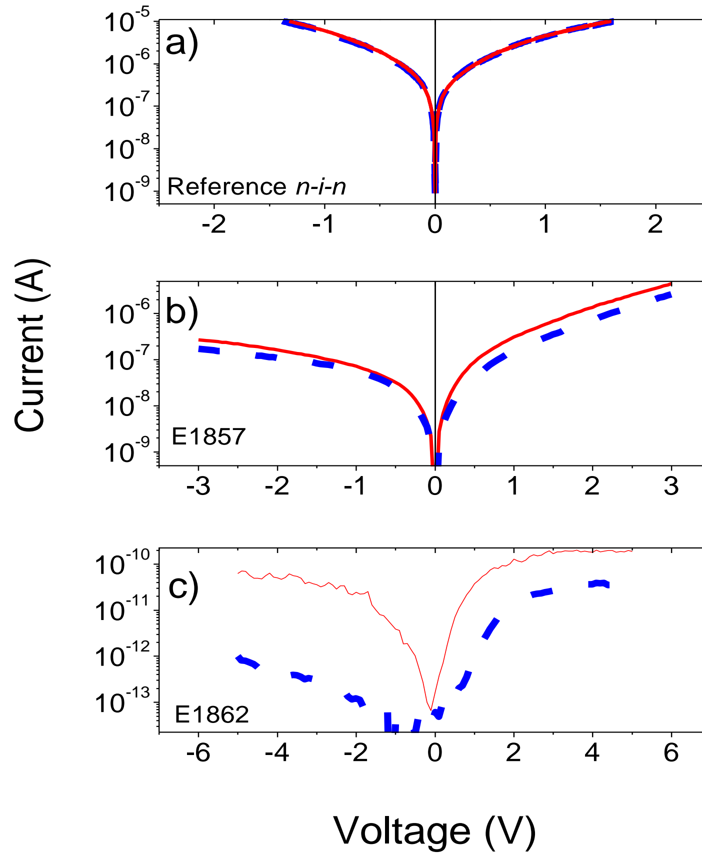

Figure 4.11 a) reference sample, (b) E1857, and (c) E1862. The blue dotted lines correspond to the dark current; the red solid lines correspond to illumination with the continuous 300 nm light with 5 mW/cm² power density.

In order to determine the spectral range of operation, the photocurrent spectra were measured from the visible to the UV domain using a tunable visible-UV light source as described in the previous chapter. The room-temperature photocurrent spectra of nanowires from the three studied samples are reported in Figure 4.12. The spectra have been divided by the photon flux from the spectral illuminator, consisting of a Xe lamp coupled to a Jobin Yvon Triax180 monochromator, and subsequently normalized to the maximum.

The recorded photoresponse of the n-i-n reference sample shows a photocurrent onset at ~3.25 eV that is slightly lower than the GaN bulk absorption. The photocurrent onset below the GaN band gap may be attributed to either bandtails in the gap due to the high Si doping level or to the Franz-Keldysh effect due to the lateral band bending (Cavallini, 2007). A similar behavior was seen in the nanowire spectrum from E1857 but a change of the slope above the GaN band gap is present. This could be related to the contribution of the strained GaN lower nanowire part. Moreover, one should expect an additional contribution related to the Qdiscs, but the presence of the GaN shell around the entire nanowire causes a high background current masking the possible photocurrent contribution of the Qdiscs.

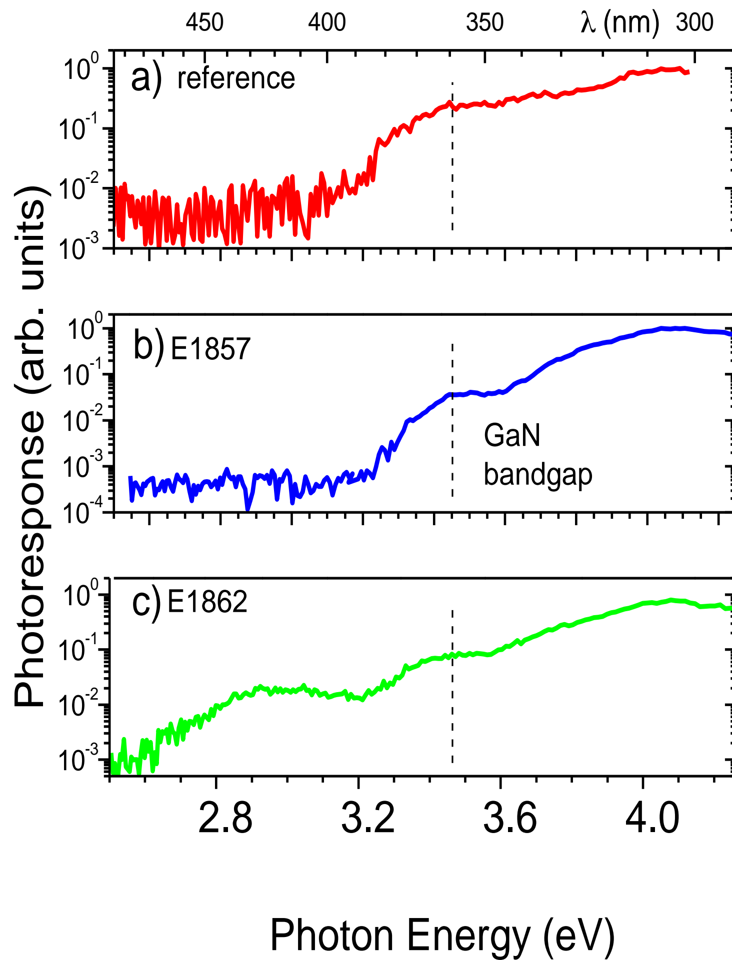

Figure 4.12. Normalized photocurrent spectra of single nanowires from (a) reference sample, (b) E1857, and (c) E1862 collected at RT under bias -3 V.

Unlike the two previous spectra, E1862 shows a significant contribution under the GaN band gap. The signal starts at~2.6-2.8 eV and can be attributed to the fundamental hh1-e1 absorption in the large Qdiscs. The low-energy Qdisc contribution is located at 2.9-3.1 eV depending on the investigated nanowire because of the fluctuation of the QDisc size from wire to wire. The onset of the photocurrent is in agreement with the PL data and gives further evidence that the mechanism responsible for the sub-band-gap photocurrent is the interband absorption in the QDisc region. The broadening of the low-energy peak is due to the contribution of QDiscs of different thicknesses within the same wire.

The responsivity at 2.9 eV corresponding to the contribution of large QDiscs is estimated to be 13 A/W (assuming that the active detector area is equal to the exposed surface of the QDisc region). This value is weak compared to the responsivity at high energies (2×10^3 A/W at 4.1 eV). This is due to the low efficiency of the carrier extraction

from the ground state of large QDiscs, which lies at a much lower energy than the barriers. Photocurrent at energies higher than the GaN band gap should be mainly generated by the fundamental absorption in narrow QDiscs and by excited transitions in large QDiscs, for which carriers have a stronger extraction probability. However, a contribution of the GaN nanowire extremities cannot be excluded.

Temperature and bias dependence

When carriers are created in the nominally undoped region of an n-i-n structure by optical illumination, they are either swept out by the electric field to generate a photocurrent, or they recombine. In a multiple quantum disc n-i-n structure, with the quantum discs in the intrinsic region, the sweep-out process is blocked by the barriers that form the quantum discs. Two main mechanisms allow the carriers to escape from the discs and generate a photocurrent: thermal emission and tunneling.

The importance of the contribution of thermal escape to the overall photocurrent is confirmed by comparison of the photocurrent spectra collected at different temperatures (figure 4.13a left). The photocurrent spectra at RT and at 10 K of a nanowire from E1862 show that the photocurrent is reduced when lowering the temperature and the spectral shape is also changed. The photocurrent onset is shifted to higher energies at low temperature according to the band gap increase. Finally, the sub-band-gap contribution of the large QDiscs is strongly reduced and is almost masked by the background noise at 10 K. This strong temperature dependence of the sub-bandgap photocurrent demonstrates that the photogenerated carrier extraction from the QDiscs is thermally assisted.

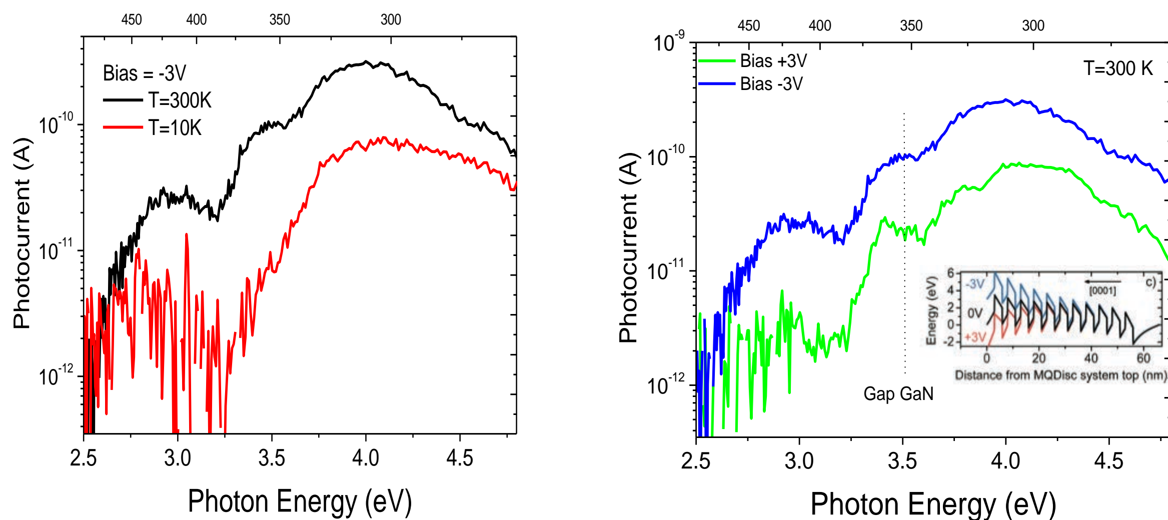

Figure 4.13. (Left) Photocurrent spectra of a nanowire from E1862 collected at RT (black dashed line) and at 10 K (red solid line). (b) RT photocurrent spectra of the same nanowire under -3 V (blue dashed line) and +3 V (green solid line) applied bias (right). The inset shows the simulation of the conduction band profile along the nanowire axis for different applied bias (-3 V, blue line; 0 V, black line; +3 V, red line).

Figure 4.13b (right) reports the photocurrent spectra of the same nanowire for -3 V and +3 V applied bias. For positive bias the photocurrent over the whole spectral range is weaker than that for negative bias. In particular, the sub-band-gap contribution of large Qdiscs is reduced. The origin of the non-symmetrical electrical response of the photodetector is the band bending induced by the polarization discontinuity at GaN/AlN interfaces in the Qdisc region.

To better understand these experimental results, the conduction band profile along the nanowire axis was simulated using a one-dimensional effective mass approximation. The simulation result is shown in the inset to figure 4.13b. It shows that at zero bias there is a band tilting across the Qdisc region as expected in GaN/AlN heterostructures. For negative bias the external voltage drop adds up with the band tilting which enhances the extraction and the transport of photogenerated carriers through the Qdisc region. For positive bias, the external voltage is opposed to the band tilting so that the effective voltage drop across the heterostructure region is reduced, thus lowering the extraction of carriers from the Qdiscs.

Conclusions

In this chapter, I have discussed the design and provide an extensive characterization of a UV photodetector based on GaN/AlN quantum discs in a single nanowire.

Structural analysis from HAADF STEM revealed that the Qdiscs thickness varies along the nanowires from samples E1857 and E1862. In the case of E1857 a lateral GaN shell surrounding the Qdisc region was formed while the formation of the outer GaN lateral shell was avoided in E1862 by changing growth conditions. The photoluminescence from nanowire ensembles showed a low energy contribution below the band-gap due to the presence of large Qdiscs (as a result of the quantum-confined Stark effect). In single dispersed nanowires from E1862, an additional high-energy peak above the band gap was found. The previous results were corroborated with two-dimensional cathodoluminescence spectral imaging with nanometer spatial resolution. It was shown that it is possible to identify the origin of the spectral features and in some cases determine the emission from individual Qdiscs in combination with high-resolution imaging.

Transport studies revealed a strong difference between the studied samples. As a consequence of the GaN shell which confines the electrons into a narrow surface region, the conduction in nanowires from E1857 showed a strong dependence on the environmental conditions. This core-shell structure is very promising for fabrication of high-sensitive chemical or biological nanowire-based sensors. In E1862 where no GaN shell is present, electron transport through the QDisc structure occurs by tunneling, thereby giving rise to a negative differential resistance in the I–V curves of a subset of the processed single-wire devices. The negative differential resistance is reproducible and persists up to 250K.

The spectral response of the photodetectors is in the UV domain. While the photocurrent from the reference sample does not show any contribution besides the GaN absorption, photocurrent from E1862 presents a sub-band-gap peak related to the interband absorption between the confined states in the large Qdiscs. On the other hand, the surrounding GaN shell in E1857 has a negative impact since it provides a channel for a high dark current, masking any contribution from the Qdiscs. The inclusion of the Qdiscs in samples E1857 and E1862 reduces significantly the dark current with respect to the reference GaN sample.

Future efforts in this area must address the design and conception of intersubband photodetectors based on the absorption between electronic confined states in the conduction band. The expected response lies in the mid and near infrared spectral range.

BIbliography

Baumann, E, Giorgetta, F. R., & Hofstetter, D. (2005). Tunneling effects and intersubband absorption in AlN / GaN superlattices. *Applied Physics Letters*, (032110), 1-3.

Bellotti, E., Driscoll, K., Moustakas, T. D., & Paiella, R. (2009). Monte Carlo simulation of terahertz quantum cascade laser structures based on wide-bandgap semiconductors. *Journal of Applied Physics*, *105*(11), 113103. doi:10.1063/1.3137203

Calarco, Raffaella, Marso, M., Richter, T., Aykanat, A. I., Meijers, R., V D Hart, A., Stoica, T., et al. (2005). Size-dependent photoconductivity in MBE-grown GaN-nanowires. *Nano letters*, *5*(5), 981-4. American Chemical Society. doi:10.1021/nl0500306

Cavallini, A., Polenta, L., Stoica, M. R., Calarco, R., Meijers, R. J., Richter, T., & Lth, H. (2007). Franz − Keldysh Effect in GaN Nanowires. *Nano Letters*, *7*(7), 2166-2170. doi:10.1021/nl070954o

Chen, R.-S., Chen, H.-Y., Lu, C.-Y., Chen, K.-H., Chen, C.-P., Chen, L.-C., & Yang, Y.-J. (2007). Ultrahigh photocurrent gain in m-axial GaN nanowires. *Applied Physics Letters*, *91*(22), 223106. doi:10.1063/1.2817595

Chu, W.-H., Chiang, H.-W., Liu, C.-P., Lai, Y.-F., Hsu, K.-Y., & Chung, H.-C. (2009). Defect-induced negative differential resistance of GaN nanowires measured by conductive atomic force microscopy. *Applied Physics Letters*, *94*(18), 182101. doi:10.1063/1.3130728

Chuang, S., & Chang, C. (1996). k·p method for strained wurtzite semiconductors. *Physical Review B*, *54*(4), 2491-2504. doi:10.1103/PhysRevB.54.2491

Furtmayr, F., Vielemeyer, M., Stutzmann, M., Laufer, A., Meyer, B. K., & Eickhoff, M. (2008). Optical properties of Si- and Mg-doped gallium nitride nanowires grown by plasma-assisted molecular beam epitaxy. *Journal of Applied Physics*, *104*(7), 074309. doi:10.1063/1.2980341

Golka, S., Pflügl, C., Schrenk, W., Strasser, G., Skierbiszewski, C., Siekacz, M., Grzegory, I., et al. (2006). Negative differential resistance in dislocation-free GaN∕AlGaN double-barrier diodes grown on bulk GaN. *Applied Physics Letters*, *88*(17), 172106. doi:10.1063/1.2199445

Hofstetter, Daniel, Baumann, E., Giorgetta, F. R., Théron, R., Wu, H., Schaff, W. J., Dawlaty, J., et al. (2009). Photodetectors based on intersubband transitions using III-nitride superlattice structures. *Journal of physics. Condensed matter : an Institute of Physics journal*, *21*(17), 174208. doi:10.1088/0953-8984/21/17/174208

Hsu, J. W. P., Manfra, M. J., Molnar, R. J., Heying, B., & Speck, J. S. (2002). Direct imaging of reverse-bias leakage through pure screw dislocations in GaN films grown by molecular beam epitaxy on GaN templates. *Applied Physics Letters*, *81*(1), 79. doi:10.1063/1.1490147

Jain, S. C., Willander, M., Narayan, J., & Overstraeten, R. V. (2000). III–nitrides: Growth, characterization, and properties. *Journal of Applied Physics*, *87*(3), 965. doi:10.1063/1.371971

Kikuchi, A., Kawai, M., Tada, M., & Kishino, K. (2004). InGaN/GaN Multiple Quantum Disk Nanocolumn Light-Emitting Diodes Grown on (111) Si Substrate. *Japanese Journal of Applied Physics*, *43*(No. 12A), L1524-L1526. doi:10.1143/JJAP.43.L1524

Klein, P. B., Mittereder, J. A., Binari, S. C., Roussos, J. A., Katzer, D. S., & Storm, D. F. (2003). Photoionisation spectroscopy of traps in AlGaN/GaN high electron mobility transistors grown by molecular beam epitaxy. *Electronics Letters*, *39*(18), 1354. doi:10.1049/el:20030836

Kwok, S. H., Merlin, R., Grahn, H. T., & Ploog, K. (1994). Electric-field domains in semiconductor superlattices: Resonant and nonresonant tunneling. *Physical Review B*, *50*(3), 2007-2010. doi:10.1103/PhysRevB.50.2007

MEIJERS, R., RICHTER, T., CALARCO, R., STOICA, T., BOCHEM, H., MARSO, M., & LUTH, H. (2006). GaN-nanowhiskers: MBE-growth conditions and optical properties. *Journal of Crystal Growth*, *289*(1), 381-386. doi:10.1016/j.jcrysgro.2005.11.117

Polenta, L., Rossi, M., Cavallini, A., Calarco, R., Marso, M., Meijers, R., Richter, T., et al. (2008). Investigation on localized states in GaN nanowires. *ACS nano*, *2*(2), 287-92. American Chemical Society. doi:10.1021/nn700386w

Renard, Julien, Songmuang, R., Bougerol, C., Daudin, B., & Gayral, B. (2008). Exciton and biexciton luminescence from single GaN/AlN quantum dots in nanowires. *Nano letters*, *8*(7), 2092-6. doi:10.1021/nl0800873

Rigutti, L., Jacopin, G., Largeau, L., Galopin, E., De Luna Bugallo, a., Julien, F., Harmand, J.-C., et al. (2011). Correlation of optical and structural properties of GaN/AlN core-shell nanowires. *Physical Review B*, *83*(15), 1-7. doi:10.1103/PhysRevB.83.155320

Ristić, J., Calleja, E., Sánchez-García, M., Ulloa, J., Sánchez-Páramo, J., Calleja, J., Jahn, U., et al. (2003). Characterization of GaN quantum discs embedded in AlxGa1-xN nanocolumns grown by molecular beam epitaxy. *Physical Review B*, *68*(12), 1-5. doi:10.1103/PhysRevB.68.125305

Sakr, S., Warde, E., Tchernycheva, M., Rigutti, L., Isac, N., & Julien, F. H. (2011). Origin of the electrical instabilities in GaN/AlGaN double-barrier structure. *Applied Physics Letters*, *99*(14), 142103. doi:10.1063/1.3645011

Sanford, N. A., Blanchard, P. T., Bertness, K. A., Mansfield, L., Schlager, J. B., Sanders, A. W., Roshko, A., et al. (2010). Steady-state and transient photoconductivity in c-axis GaN nanowires grown by nitrogen-plasma-assisted molecular beam epitaxy. *Journal of Applied Physics*, *107*(3), 034318. doi:10.1063/1.3275888

Simpkins, B. S., Mastro, M. A., Eddy, C. R., & Pehrsson, P. E. (2008). Surface depletion effects in semiconducting nanowires. *Journal of Applied Physics*, *103*(10), 104313. doi:10.1063/1.2932072

Soci, C., Zhang, a, Xiang, B., Dayeh, S. a, Aplin, D. P. R., Park, J., Bao, X. Y., et al. (2007). ZnO nanowire UV photodetectors with high internal gain. *Nano letters*, *7*(4), 1003-9. doi:10.1021/nl070111x

Tchernycheva, M., Sartel, C., Cirlin, G., Travers, L., Patriarche, G., Harmand, J.-c, Dang, L. S., et al. (2007). Growth of GaN free-standing nanowires by plasma-assisted molecular beam epitaxy : structural and optical characterization, *18*, 1-7. doi:10.1088/0957-4484/18/38/385306

Vashaei, Z., Bayram, C., & Razeghi, M. (2010). Demonstration of negative differential resistance in GaN/AlN resonant tunneling diodes at room temperature. *Journal of Applied Physics*, *107*(8), 083505. doi:10.1063/1.3372763

5. InGaN/GaN single wire photodetectors and light emitters

Introduction

Nanoscale crystals are often free from extended crystal defects such as threading dislocations, which can degrade the optical performance of the material by acting as non-radiative recombination centers. Thus, “nano-LEDs” are essentially free of defect-related non-radiative recombination centers and offers high internal quantum efficiency are of great interest. In this chapter I present the study of GaN wires grown by MOVPE containing an InGaN/GaN multiple quantum well (MQW) system as promising candidates for photodetection and light emission applications. The MQWs cover the top part of the wire while in the bottom part only GaN core is present. STEM analysis reveals the presence of both nonpolar radial (on the wire facets) and polar axial (on the top wire facet) MQW systems. Photoluminescence experiments show a strong dependence of the emission on the excitation position in the wire. The wires used as photodetectors exhibit a photocurrent contribution below the GaN band gap arising from InGaN QWs in agreement with PL measurements. Moreover, OBIC measurements demonstrate that the photocurrent signal is located exclusively in the immediate neighborhood of the NW top, in correspondence with the unintentionally doped MQW region. Finally, the temperature and injection current dependence of the electroluminescence (EL) from the wire-based LEDs was studied. Cathodoluminescence (CL) and EL experiments reveal that polar QWs emit at lower energy than nonpolar QWs; the low energy EL contribution is observed at room temperature and at a low injection current level, while the higher energy peak becomes dominant at higher injection current, and is the only peak observable at low temperature.

5.1 GaN/InGaN QW structure

The InGaN QW is the radiative recombination region of electron-hole pairs in blue LEDs and laser diodes. By changing the In-concentration in the alloy, the light emission wavelength can be shifted in principle from the near UV into the infrared spectra. The energy band gap Eg of $In_xGa_{x-1}N$ over $0 \le x \le 1$ can be expressed by the following expression:

$$E_{In_xGa_{1-x}N} = xE_{InN} + (1-x)E_{GaN} - b_{InGaN}x(1-x)$$

where E_{GaN} and E_{InN} are the band gap energies of GaN and InN respectively while b_{InGaN} denotes the bowing parameter of InGaN.

Table 5.1 show some commonly used values for b_{InGaN} in hexagonal III-N alloys are listed in Table 5.1.

b_{InGaN} (eV)	Reference
1.782	Liou, 2005
1.0	Nakamura, 1995
2.5	Davydov, 2002

Table 5.1 Band bowing parameters bx InGaN.

The InGaN lattice parameter increases with x leading to strain between the GaN quantum barrier and the InGaN quantum well.

The quantum well (QW) has been an effective structure for efficient light emission from III-nitride semiconductors since Nakamura et al. (S. Nakamura, 1998) succeeded in making a high-quality InGaN multi quantum-well (MQW) structure on the polar *c*-axis of the wurtzite crystal structure using (0001) sapphire substrates. Although the *c*-plane is known as one of the stable planes in GaN, $In_xGa_{1-x}N$ devices grown on c-plane GaN suffer from large internal electric fields due to the discontinuity of the spontaneous polarization across the hetero-interfaces

and to the buildup of a piezoelectric polarization field in the strained heterostructure films. These electric fields result in a separation between the electron and hole wavefunction in the quantum wells (Figure 5.1b) and limit their radiative recombination efficiency [Berkowicz00].

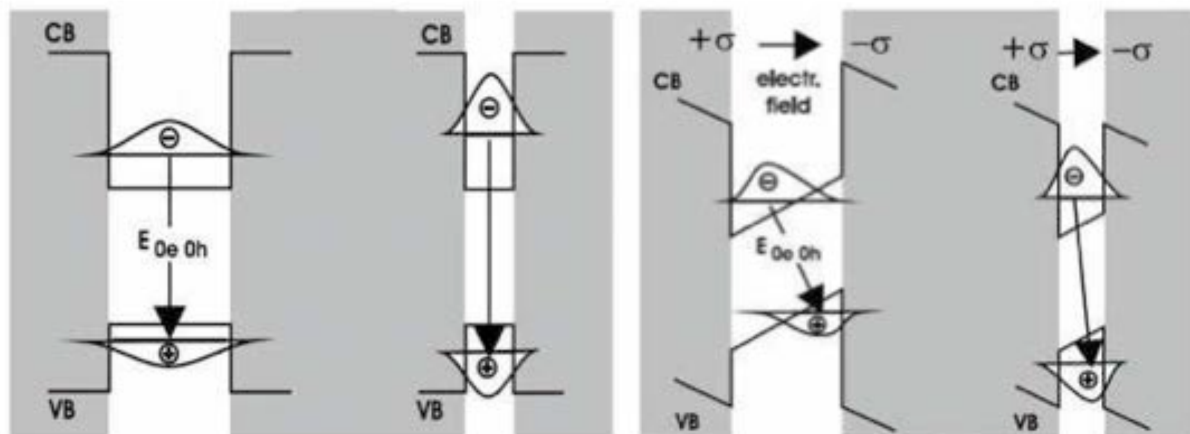

Figure 5.1 Schematics of the energy band in a QW without (left) and with an internal electric field (right) and illustration of the impact of the QW thickness.

As discussed in Chapter 4, due to the quantum-confined Stark effect (QCSE), the accumulation of electrons and holes at the opposite sides inside the QW causes a shift in the emission energy with respect to the field-free case. Since the QCSE strongly depends on the crystal orientation, it can be avoided by growing GaN films along nonpolar directions, such as the m-plane direction, which leads to a more efficient recombination across the entire well of a QW structure as illustrated in figure 5.1a. Previous studies of planar InGaN/GaN LEDs prepared on non-polar oriented planes have shown an enhanced light emission efficiency (Fasol, 2001)(S. Nakamura, 1998)(Jain, 2000).

The nanowire architecture has potentially significant differences compared to planar heterostructures beyond that of dimensionality. In particular, as nanowire synthesis allows designing axial or radial heterostructures without dislocations originating from the lattice mismatch between GaN and InGaN, a significant reduction of nonradiative recombination with respect to planar structures is expected. However, for core-shell nanowires, there is a critical radius for which stress relaxation cannot be done laterally. This depends on the length of the nanowire and the lattice mismatch with the substrate. (Glas, 2006).

The approach used in this study is to take advantage of the MOVPE synthesis technique to grow non-polar radial InGaN/GaN multiple quantum well heterostructures on the sidewall of c-axis GaN wires and demonstrate their potential in photodetectors and LED applications.

5.2 Wire structure of an n-i-n junction: the T929 sample

The wire growth was carried out using catalyst-free MOVPE on sapphire substrates and performed by Xiaojun Chen at the Institut de Nanoscience et Cryogénie (INAC). INAC colleagues were also in charge of the structural characterization. The growth procedure for c-oriented GaN wires is the following. First, SiN_x thin film is deposited on the sapphire substrate (Koester, 2010)(X. J. Chen, Perillat-Merceroz, Sam-Giao, Durand, & Eymery, 2010). Then the stem of the wires is grown at 1000 °C using trimethylgallium and ammonia with a silane addition to get n+ doping. The silane flux is then switched off to grow unintentionally doped GaN at the top of the wires. Finally, GaN wires are coated at their top with five unintentionally doped radial InGaN/GaN quantum wells. InGaN wells and GaN barriers are grown at 730 °C and 840 °C, respectively, using trimethylindium and triethylgallium as III-precursor sources. For photodetection applications, the last GaN quantum barrier is n-doped type with silane forming an n-i-n junction. The In concentration in the QWs estimated by time-of-flight secondary ion mass spectrometry is about 16% (±4%).

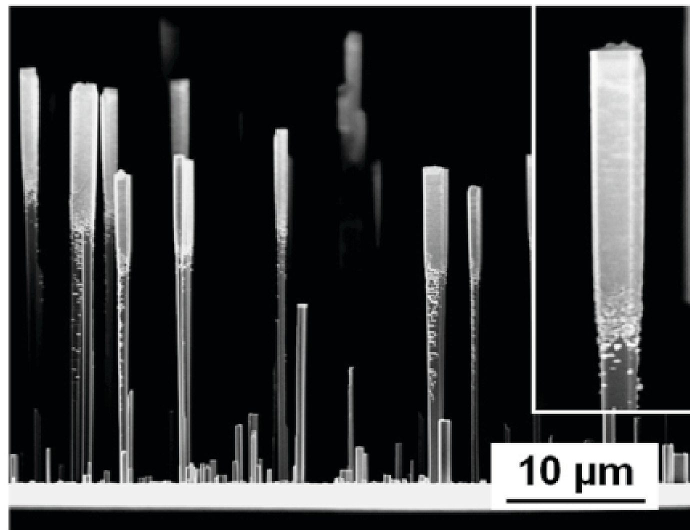

Figure 5.2 SEM image corresponding to InGaN/GaN MQW (5x) grown on GaN wires. The inset shows a detailed view of a MQW structure.

The result of the growth reveals a match-like structure where the five InGaN/GaN MQWs are located at the upper part of the wires. Fig. 5.3a shows the SEM image of sample T929. The wires have a length between 15 and 30 μm and a diameter range of 500 nm to 1 μm. The radial overgrowth is smooth and continuous at the top, but becomes more irregular toward the bottom where small grains related to In clusters are observed. Scanning transmission electron microscopy (STEM) measurements were performed to investigate the MQW heterostructures in single wire cross sections orthogonal to the c-axis. The wires were thinned by Focused Ion Beam (FIB) and transferred into the SEM equipment. Images from figure 5.3b,c show clearly the core/shell geometry and demonstrate a good structural quality of the InGaN/GaN superlattice grown on the m-plane sidewall facets. From the HAADF images (5.3b,c), the dark contrast corresponds to the GaN core while the bright contrast belongs to the InGaN shell; the thickness measurements give 1 nm for the wells and 8 nm for the barriers.

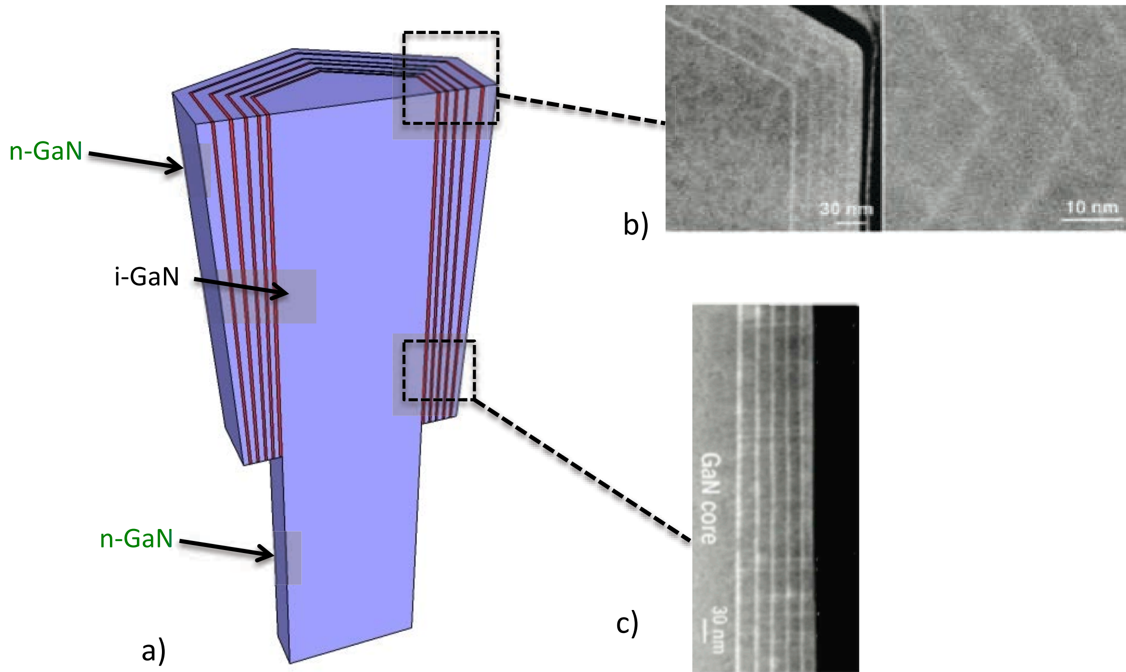

Figure 5.3 a) Diagram of the core-shell MQW structure b) HAADF STEM images of the InGaN MQW cross-section orthogonal to the wire length direction show a hexagonal shape with m-plane facets c) HAADF STEM image of a cross-section of a wire parallel to the growth direction taken along the [1120] zone axis.

5.2.1 Micro photoluminescence spectroscopy

Nanowires were dispersed on a SiO_2 substrate to carry out micro-photoluminescence experiments. Figure 5.4a shows the uPL spectra of a single wire of sample T929 performed at 4K. It should be noted that the PL signal varies significantly as a function of the excitation position of the laser along the wire (figure 5.4a). When the spot is focused on the base-middle of the wire, the spectra present a unique contribution between 3.45 and 3.6eV related to the n-GaN near band edge. The broad emission is a result of the high doping level $1x10^{20}cm^{-3}$. Moving forward to the top, the emission from the n–GaN NBE peak starts decreasing while a sub-band gap contribution centered at 3.05eV associated to the MQWs begins to appear. Finally, when the spot hits the higher part of the wire, a strong signal coming from the InGaN/GaN QWs is present and the GaN contribution disappears. This is also illustrated in Fig 5.4b, which shows the integrated spectral intensity around 3.05 eV and around 3.5 eV as a function of the excitation position.

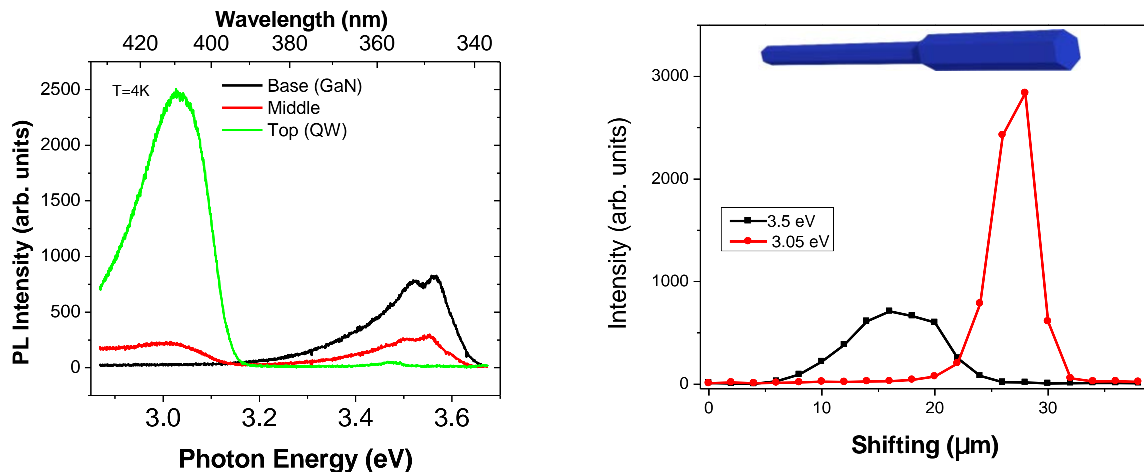

Figure 5.4 a) PL spectra collected at T=4K moving the laser spot along a wire from the base-middle (black), middle top (red) and top (green); b) intensity integral of the emissions around 3.05 eV (red, QWs) and 3.5 eV (black, GaN).

5.2.2 Electrical characterization and optical response

Single-wire photodetectors were fabricated following the technological process described in chapter 2; an SEM image of the processed device is shown in figure 5.5a. Electrical transport measurements were performed using a probe station and a Keithley 2636 source-meter. The typical I-V curves of one representative device, labeled W1, are reported in Fig.5.5b. Measurements were done at RT in ambient air under different illumination conditions. The curves are symmetries with respect to positive and negative biases and exhibit a quasi-ohmic behavior, with a dark resistance at zero-bias R_0=20 kΩ.

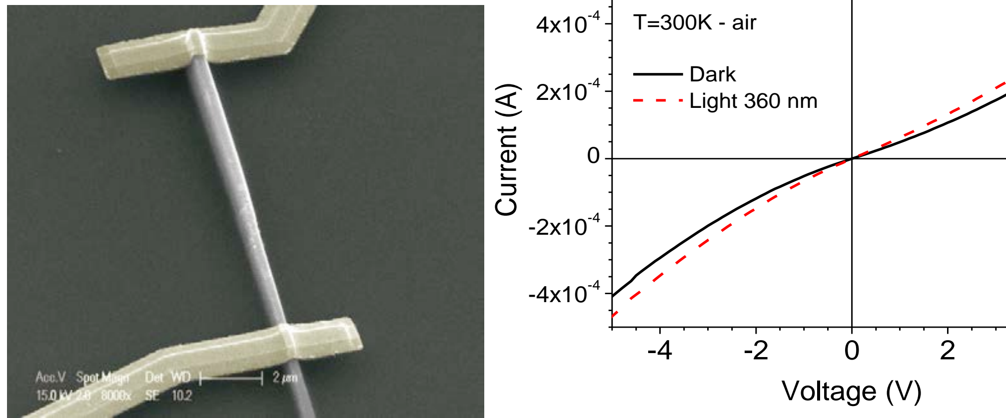

Figure 5.5. a) SEM image of a contacted wire. b) I-V curves of a single-nanowire (labeled W1) device at RT, in the dark (black solid line), and under illumination at λ = 360 nm (red dashed line).

The photoresponse of the W1 device was studied under two types of illumination; the first one corresponding to the GaN NBE (λ =360 nm) and the second one below the GaN NBE (λ =400 nm) with an incident power density of P_{inc}=30 mW/cm^2 and a bias of 5 V. For both cases the conductivity of the NW increases. It should be noted that no change in the I-V characteristics occurs under vacuum or when illuminating with light at λ =520 nm.

Upon illumination at a wavelength λ =360 nm, the photocurrent is I_{PC}=5x10^{-5} A when biased at 5 V. Taking into account the wire exposed area where the lateral overgrowth occurred, this corresponds to a responsivity and photoconductive gain of R=2.5x10^4 A/W and G= 9.2x10^3 (at λ =360 nm and bias=5 V) respectively. As the device is an *n-i-n* junction, the photocurrent is generated through a photoconductive mechanism, with the production of excess carriers within the undoped region (Monroy, 2003).

For illumination under the GaN band gap (λ =400 nm), we obtain a responsivity R=1.6x10^4 A/W and a gain G=5.2x10^3. This gain value G>>1 suggests that a spatial separation mechanism strongly suppresses the recombination of the photogenerated e-h pairs (Soci et al., 2007)(Calarco et al., 2005)(R. S. Chen, 2009) as discussed in previous chapters. However, in these radial junctions the carrier separation mechanism must be different since the device geometry is different. In the present core-shell photodetector, the mechanism is most likely related to the presence of an upward band bending along the NW axis. The resulting electric field attracts the photogenerated holes toward the top polar surface, and separates them from electrons in the active region, as

in the case of bulk GaN-based n-i-n photoconductors (Garrido,1998). Moreover, holes may be trapped at the top surface yielding a diminution of the surface space charge region, thus contributing to the increase in the device conductivity (Garrido,1998).

5.2.3 Operation speed

The speed of the W1 device was characterized by measuring the rise and decay current transients at room temperature under UV illumination (λ =360 nm). The transients may be fitted by the expression $I = I_0 + Ae^{\left[-(t/\tau)^{\alpha}\right]}$ with α =0.35, the time constant τ is ~10 s for the rising time and 3000 s for the decay time. Similar results showing persistent photocurrent have been previously reported on bulk GaN UV photodetectors (H. M. Chen & Chen, n.d.)(Katz, 2004) and GaN nanowire detectors (Sanford, 2010).

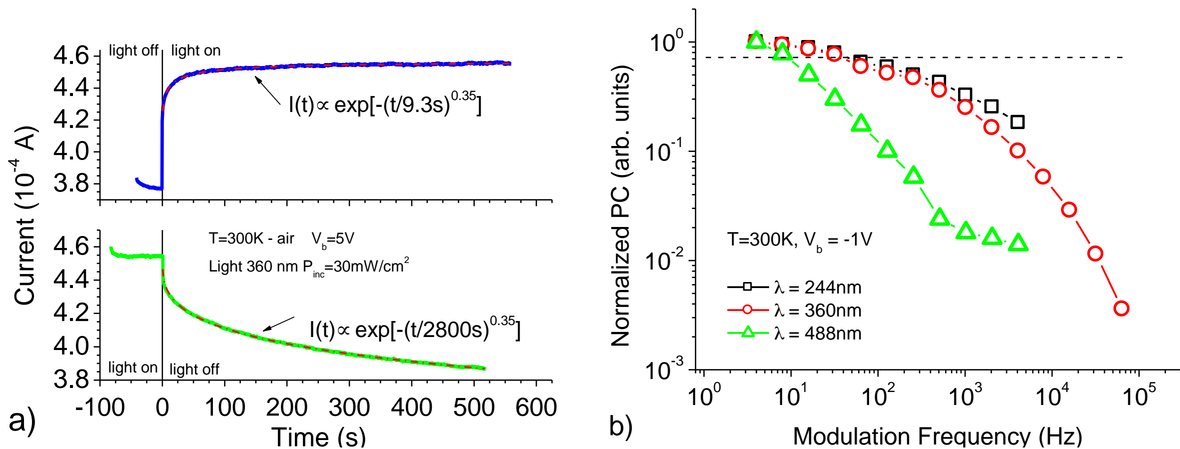

Figure 5.6 a) Time response of the W1 device polarized at *Vb=5* V to light steps. b) Normalized frequency response of the detector to modulated light at λ=244 nm (black squares), at λ=360 nm (red circles) and at λ=488 nm (green triangles).

To identify the fast component, the response to modulated light was analyzed using three different sources: 1) the frequency-doubled 244nm Ar laser 2) the 350nm LED used for the PL visualization system and 3) the 488nm Ar laser. The results, illustrated in Fig. 5.6b, show that for the two UV wavelengths the -3 dB cutoff of the detector is at f_T~50 Hz, corresponding to the fast component characteristic time ~3 ms. The cutoff drops to f_T~20 Hz for light at λ =488 nm. The observed persistent PC behavior can be explained keeping into account the spatial separation

of carriers and the modulation of the surface space charge width by hole trapping (Garrido, 1998). However, the difference in the cutoff frequency for UV and visible light indicates that the hole trapping mechanism may be different in the case of the GaN and QW excitation, respectively.

5.2.4 Photocurrent spectroscopy

The spectral response of the MQW wire-based photodetector was measured using a tunable visible-UV light source, consisting of a Xe lamp coupled with a Jobin Yvon Triax 180 spectrometer and normalized by the incident power of the monochromatized light. For comparison, photocurrent measurements were also performed on wires with the sample morphology but without the insertion of the InGaN QWs (sample T629). A typical PC spectrum from the W1 device (green) recorded at RT in air and under bias Vb =1 V is shown in Fig. 5.7a.

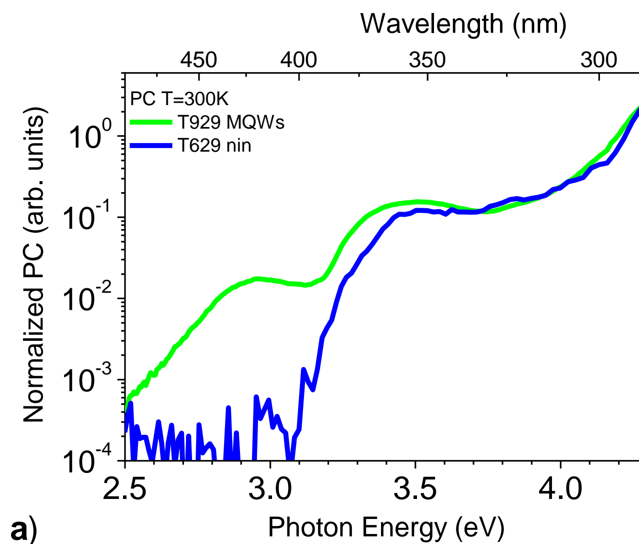

Figure 5.7 normalized photocurrent spectra from the MQW sample T929, device W1 (green curve) and from one wire from the n-i-n reference sample T629, containing no heterostructure (blue curve).

The step-like structure of the photocurrent spectra has an onset at 2.5 eV for W1 device. A first significant sub bandgap contribution is located at 3.0 eV, a second PC onset at 3.3 eV close to the GaN NBE is present, then the signal extends to the deep UV range. It should be pointed out that the PC spectrum from sample T629 (blue) does not exhibit any sub bandgap signal comparable to that of sample T929.

The PC spectrum from sample T929 can also be compared to its microphotoluminescence spectrum excited at the top of the wire (Fig.5.4). Based on this comparison, we can attribute the sub-bandgap PC contribution to transitions taking place within the radial MQW system. The PC onset at 3.3eV is most likely related to photogeneration in the unintentionally doped GaN barriers in the MQW region. Finally, the slight redshift with respect to the GaN band gap can be explained by band tailing effects.

5.2.5 Optical beam induced current

In order to know where the photocurrent is generated, we have investigated the spatial distribution of PC generation by means of spatial PC microscopy (SPCM) also known as optical beam-induced current (Wilson & McCabe, 1987). The sample was illuminated with a laser light either at λ =488 nm or at λ =244 nm focused by a 20x objective lens with 0.4 numerical aperture.

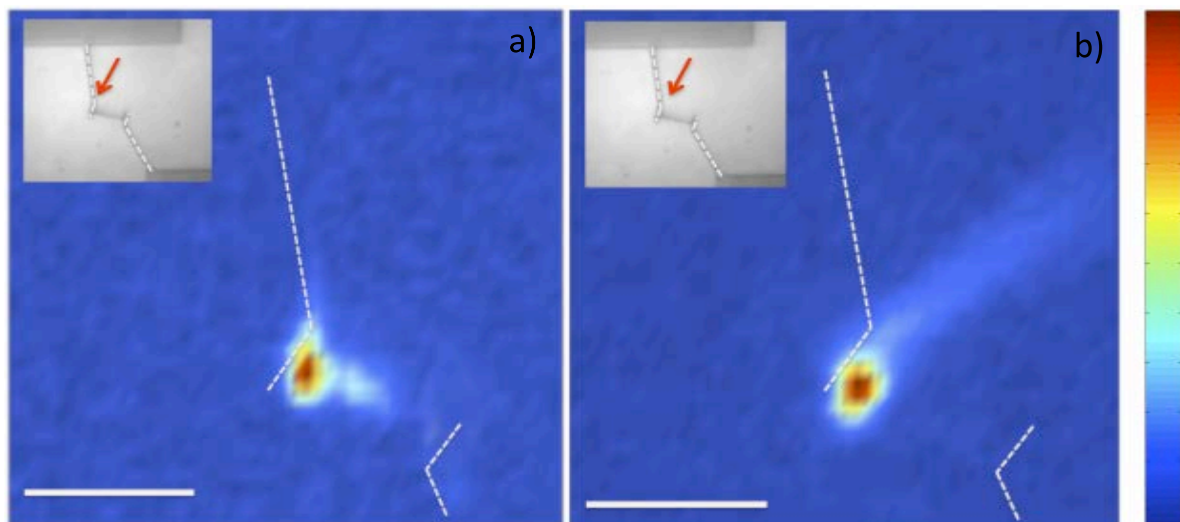

Figure 5.8 SPCM images collected while exciting the sample with laser light a) at λ= 488 nm and b) λ= 244 nm. The inset image is a UV micrograph visualizing the area containing the contacted wire analyzed by means of SPCM. The red arrow points to the NW top. The white scale bar corresponds to 20 μm. The scale reported on the right-hand side is linear from 0 to the maximum PC recorded within each image.

Figures 5.8a (488 nm) and 5.8b (244 nm) show the photocurrent maps for both excitation wavelengths. It is clearly seen that most of the PC is localized on the top of the wire. For a sub bandgap (488 nm) excitation the origin of the PC signal is attributed to the excitation of the unintentionally doped MQW region. The PC signal from the NW body is very weak, confirming that the PC is generated in the intrinsic region even for an excitation above the GaN (244nm) band gap as expected for a radial n-i-n junction. The overall device conductivity indeed increases only when the resistivity of the undoped portion drops because of the generation of free electron-hole pairs.

5.3 InGaN/GaN nanowire LEDs

The operation principle of an LED is based on a p–n junction are shown in Figure 5.9. In a p–n junction, the diffusion of free electrons from the n-side into the p-side, and the diffusion of holes in the opposite direction, creates a built-in electric field due to the ionized dopants left behind. This built-in electric field creates an energy barrier for the majority carriers, of height eV_D, where V_D is often denoted the diffusion voltage. At thermal equilibrium, few majority carriers have enough energy to pass the diffusion voltage barrier (Fig. 5.9a). However, if a forward bias V is applied, it reduces the barrier height to $e(V_D - V)$, and more majority carriers will have enough energy to pass the barrier (Fig. 5.9b). Electrons injected into the p-side will recombine with the hole majority carriers and generate photons with an energy corresponding to the band gap of the semiconductor (the opposite applies to holes injected into the n-side). This is known as radiative recombination. Basically all high-brightness LEDs also employ one or several wells of a low band gap material at the p–n junction. The well collects carriers and increases the local concentration of electrons and holes, which enhances the radiative recombination rate.

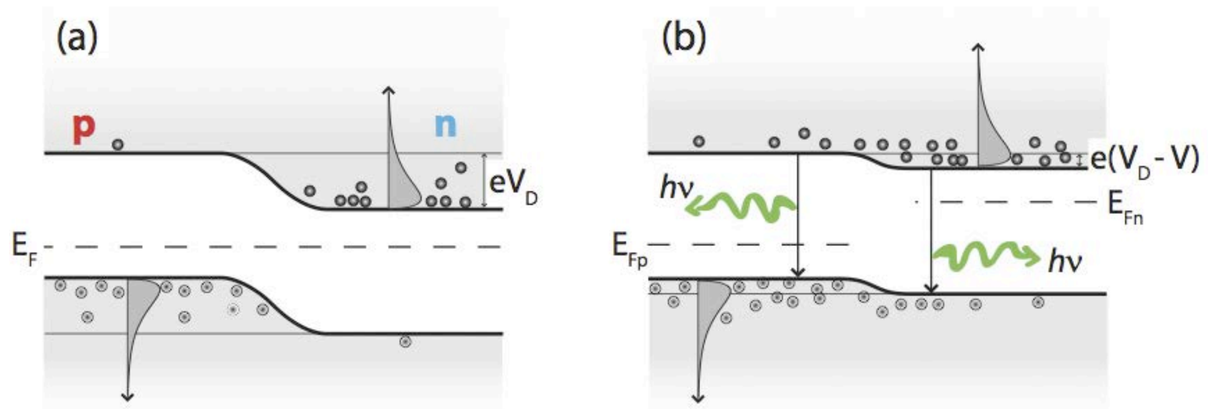

Figure 5.9. Unbiased (a) and forward biased (b) p–n junctions. (a) At zero bias few majority carriers have enough thermal energy to pass the diffusion voltage barrier eVD (the majority carrier concentrations are illustrated at the conduction and valence band edges). By applying a forward bias V, the barrier is lowered to e(VD − V), and majority carriers are injected over the barrier.

There are several loss mechanisms in a LED; not all recombinations are radiative, and non-radiative recombinations generate phonons (heat) rather than light. The ratio of radiative transitions to the total number of transitions is called the internal quantum efficiency. Moreover, light extraction from 2D layer LEDs is impeded by total internal reflection and by consequence photons are trapped in the device rather than radiating outward.

Nanowire LEDs have been fabricated in a variety of different materials and geometries. As mentioned before, nanowire are free of threading dislocations, therefore the non-radiative recombination processes will decrease, enhancing the internal quantum efficiency. In addition, the geometry provided by free standing nanowires arrays LEDs offers improvements in the light-extraction efficiency of these structures compared with their planar counterparts. When nanowire diameters below ~ 10^3 nm are combined with large refractive index differences, the efficiency of extracting light from a nanowire becomes substantial (Minot, 2007). As the wavelength of light approaches the size of the structure from where it is being emitted, the opportunity for the light wave to become totally internally reflected and eventually reabsorbed is minimized. In a nanowire light will either be directly emitted from the edge of the wire or if it is wave-guided along the wire’s long axis, it is likely to be emitted once it hits the wire’s end.

5.3.1 Wire p-i-n junction structures : samples T1163, T1164 and T1165

The wire structures used for this study are very similar to those studied in 5.2; the only difference is the replacement of n-type by a p-type GaN shell covering the 5 InGaN/GaN MQW in order to achieve a n-i-p structure.

As pointed out earlier in this chapter, the emission wavelength of InGaN structures can be controlled by the indium concentration in the QWs. In addition, indium incorporation is very sensitive to the temperature during the QW growth. Therefore, three samples T1163, T1164 and T1165 were grown at different InGaN growth temperatures (750ºC, 735ºC and 710ºC, respectively) in order to obtain QWs with various In composition. According to the calibration based on spatially- resolved secondary ion mass spectroscopy (SIMS) measurements (Koester, 2011), the resulting In composition in the radial QWs is 24% in sample T1165, 20% in T1164 and 16% in sample T1163. The thickness of the wells is 1 nm and of the barrier 8 nm, whereas the nanowire length varies from 15 to 20 µm. A p-doped GaN outer shell grown at 920ºC in N_2 is added on the MQWs using biscyclopentadienylmagnesium as a precursor source with an annealing step performed under N_2 at 750 º C for 20 min to activate Mg dopants.

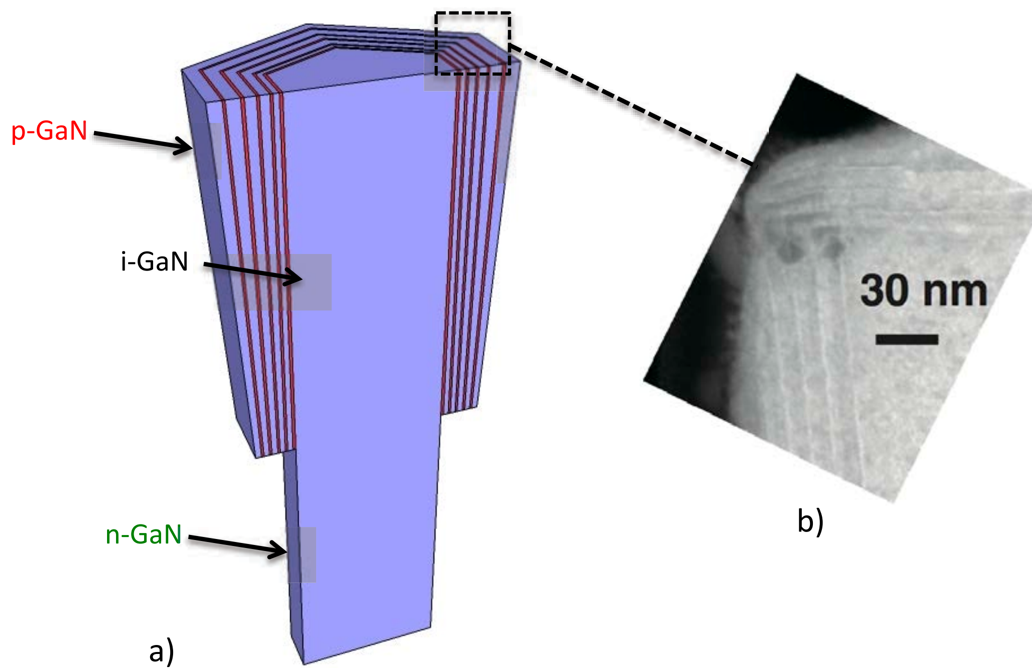

Figure 5.10 a) Scheme of the wire heterostructure b) Transmission electron microscopy image of a longitudinal slice from the top of the wire disclosing the presence of axial (polar) and radial (nonpolar) MQWs.

5.3.2 Photoluminescence

A microphotoluminescence study was carried out at 4K on single wires dispersed on a silicon substrate. Figures 5.11 show the µPL spectra from samples T1163, T1164 and T1165 taken from the MQW region. It should be mentioned that as in the case of sample T929, the PL signal has a strong dependence along the wire position (not shown here). As expected the MQW emission clearly shifts from one sample to another, the wavelength increases with the increasing In content present in the QWs. An additional spectral contribution is present centered at 2.3 eV. This broad emission is much stronger in the heavily-doped bottom part of the wire and is attributed to the GaN yellow band. The yellow luminescence (YL) band is commonly observed in undoped GaN films, but its exact source is still unresolved (Reshchikov, 2005). The presence of this YL may be caused by the diffusion and piling up of mobile point defects, such as Ga vacancies, at the surface during wire growth (Li, 2010).

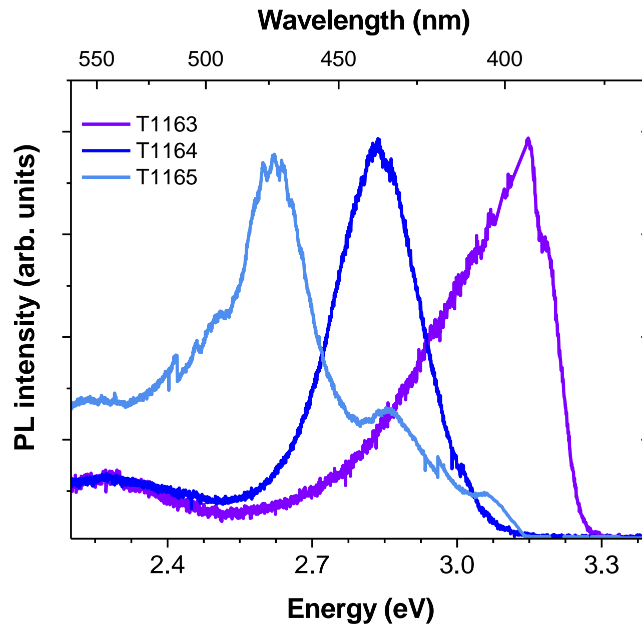

Figure 5.11 Dependence of photoluminescence spectra on the growth temperature of InGaN layers T1163=750ºC (violet), T1164=735ºC (dark blue) and T1165=710ºC (blue).

The emission peak wavelengths are plotted as a function of the InGaN layer growth temperature in Figure 5.12. The variation of the emission wavelength as a function of the QW-growth temperature shows approximately a linear dependence. The emission peak wavelength is shifted to higher energies, consequence of the decreasing indium concentration present in the InGaN active region (Yoshimoto, 1991).

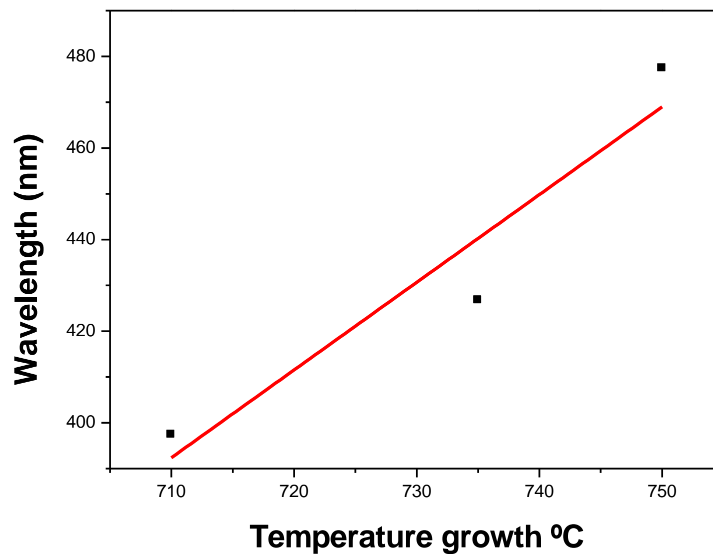

Figure 5.12 PL emission wavelengths of the three samples as a function of the growth temperature.

5.3.3 Identification of spectral contributions by cathodoluminescence

Cathodoluminescence measurements have been performed in order to analyze the spatial distribution of the different spectral components present in the wires. As mentioned before, CL spectroscopy a better spatial resolution than PL. CL was performed by Luiz Zagonel at LPS with the same set up described in the previous chapter.

Figure 5.13 shows the CL spectra of the sample T1163 taken from different positions along the wire (as show in the TEM image positions 1 to 5 are marked by a color rectangle) as well as CL images.

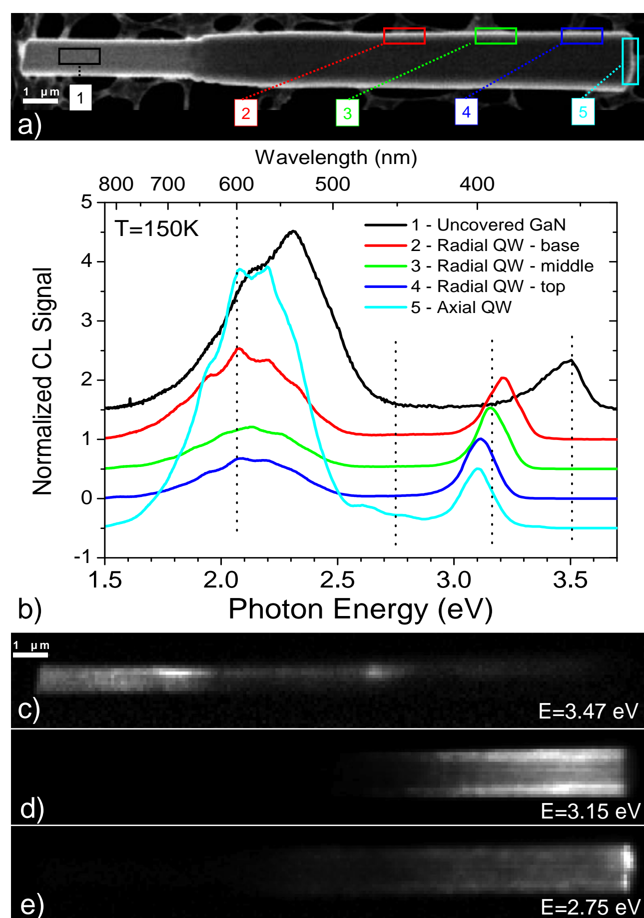

Figure 5.13 (a) Dark-field image of a wire from sample 2 analyzed by CL- STEM. (b) CL spectra collected from the regions marked in (a). Spectra are normalized and vertically shifted for clarity. (c) CL map at E=3.47eV (d) at E=3.15eV (e) at E=2.75eV.

From the CL spectra of regions 1 to 5 we can make the following remarks.

- Region 1. The emission shows a peak at 3.5 EV corresponding to the n-GaN NBE in addition, a broad yellow/green defect band peaked at around 2.35 eV.
- Regions 2 to 4. The spectra show a sub bandgap contribution related to the radial MQW shifting from 3.21 eV close to the QW base to 3.21 eV at QW top region. The spectral shift observed from region 2 to 4 can be ascribed to a QW thickness gradient, as confirmed by separate spatially-resolved SIMS in samples grown by the present technique. A broad yellow band is present peaked at 2.15 eV, which can be related to the unintentionally doped regions in the MQW.
- Region 5. The spectrum is quite similar to that of region 4; however, an emission located at 2.65 eV is present. An intense yellow band peaked at 2.15 eV, most likely related to the unintentionally doped regions in the MQW is present.

The spatial distribution of the different spectral components is reported in the CL mapping images in figure 5.13 (c - e). Figure 5.13c shows that the n-GaN NBE emission at 3.47 eV originates mostly from the GaN base. The emission located at 3.15 eV is attributed to the radial non-polar MQW (Fig. 5.13d), as it is located in the upper part of the wire. The blue emission at 2.65 eV is concentrated at the very top of the wire, so this spectral component can be unambiguously attributed to the axial polar QWs. The lower transition energy of the axial QWs with respect to the radial nonpolar QWs can be partly explained by the quantum-confined Stark effect related to the presence of an internal electric field in the axial QWs. Furthermore, the In content and well thickness in the axial QWs may be larger than those in the lateral QWs (Koester, 2011).

5.3.4 Electroluminescence

Single-wire LEDs were fabricated by a double run of e-beam lithography using a Ti/Al/Ti/Au (Ni/Au) metallization for the n-type (p-type) extremity of the wire as described in chapter 2. One of the advantages of processing this match-like structure is the fact that the MQW system is just located on the upper part of the wire leaving the n-GaN uncovered at the base so no intermediate etching of the core is necessary (Qian, 2008).

Electrical characteristics were tested using a probe station and a Keithley 2636 source-meter unit. Figure 5.14a shows a typical I–V curve from the T1163 sample measured at room temperature. It presents a well-defined current rectification which is characteristic of p-n diodes. The turn-on voltage is around 6V, which is not consistent with the band gap of a n-GaN/p-GaN device (expected at lower bias). The increase in the turn-on voltage is attributed to the dry etching processing step used to remove FOX encapsulating material from the wire surface. Indeed, it has been demonstrated that CF_4 chemistry has a negative impact on the conductivity of p-GaN films by reducing the net acceptor concentration (Cao, 1999). The optical microscopy image of a single-wire LED from sample T1163 emitting blue light at RT under a forward current (I=5μA) is shown in Fig. 5.14b. It should be pointed out that the light comes out from the wire edges and from the MQW shell. This result suggests that a substantial fraction of emitted light is coupled into the guided optical modes of the wire structure.

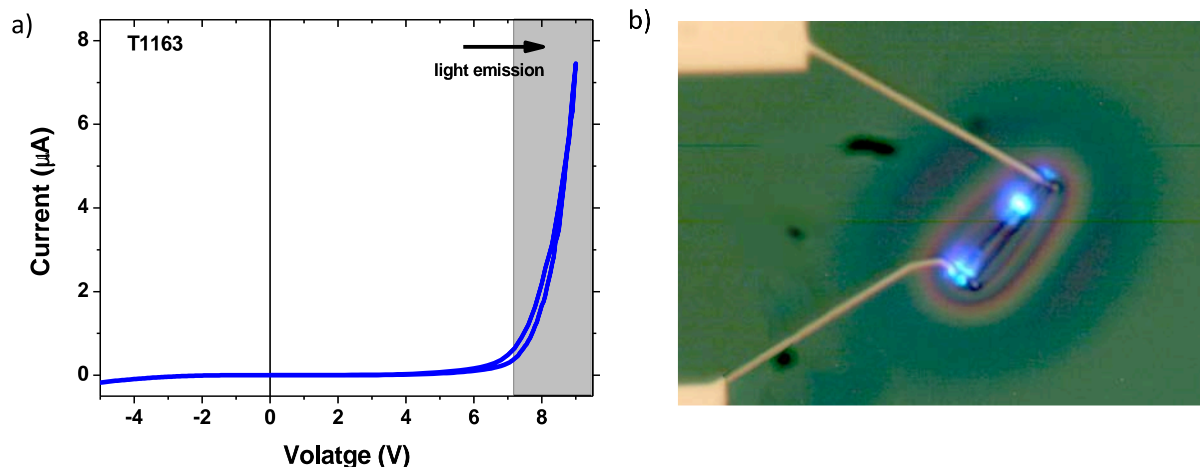

Figure 5.14 a) I-V curve from a single wire LED device. b) Optical microscopy image of a processed nanowire

emitting blue light under forward bias.

In order to determine the emission wavelength of the single wire LED devices, electroluminescence (EL) measurements were recorded using a 460-mm-focal-length grating spectrometer with a CCD array with a spectral resolution of 1 nm. Figures 5.15a and 5.15b show the recorded EL spectra for increasing injection current levels of samples T1163, T1164 and T1165. In all cases, there is a visible low energy EL peak appearing at a low injection current ($I<1$ μA). As the current is increased, the visible peak saturates and is progressively masked by a second peak growing at higher energy.

The lower-energy contribution is peaked at 2.25 eV in sample T1165, at 2.45 eV for sample T1164 and 2.70 eV in sample T1163, while the higher-energy contributions are at 3.61 eV in sample T1165, 2.89 eV for sample T1164 and 3.12 eV in T1163. As in the case for photoluminescence, we can observe a blue shift of the EL emission peaks from sample T1163 with respect to sample T1165, attributed to the smaller In content in the QWs. Taking into account the CL and PL measurements, the EL peaks centered at low energies can be correlated to the axial MQWs located at the top of the wires, whereas the high-energy contributions are related to the radial MQWs. Moreover, PL emissions from radial QWs are in good agreement with the high-energy EL contributions.

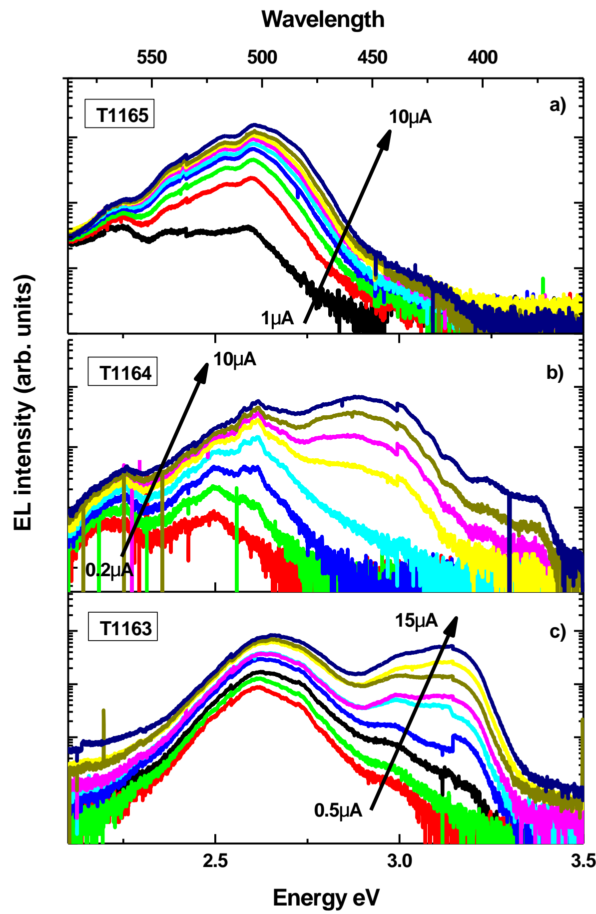

Figure 5.15 Injection-dependent electroluminescence spectra collected from single-wire LEDs from samples T1164 (top), T1156 (middle) and T1164 (bottom).

EL measurements performed at low temperature show that as the temperature is decreased, the low-energy emission from the axial MQWs becomes weaker, while the emission of the radial MQWs increases, as shown in the case of the wire from sample T1163 in Fig. 5.16.

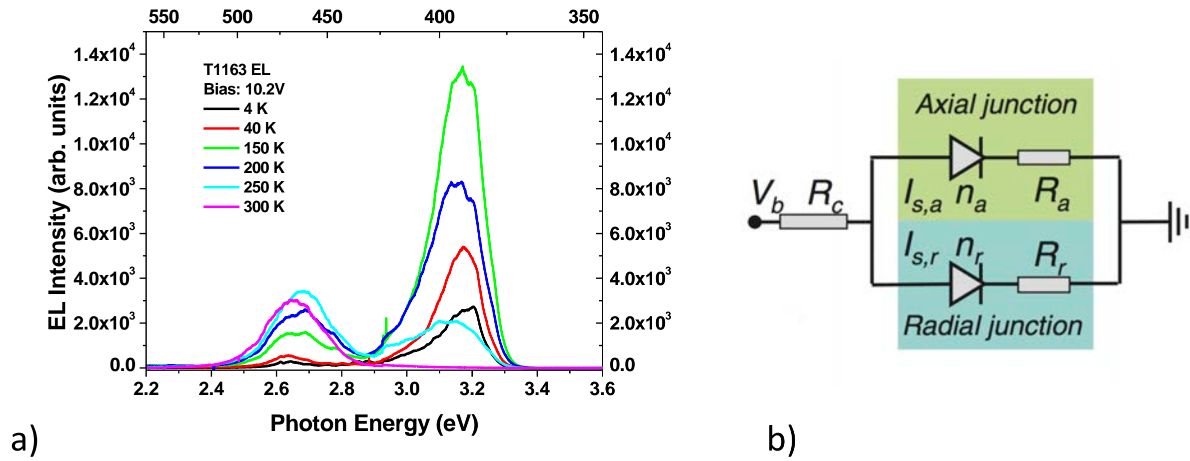

Figure 5.16 Temperature-dependent electroluminescence spectra collected from T1163. b) Scheme illustrating the two-junction model used to interpret the EL properties.

These optoelectronic properties can be interpreted by approximating the single-wire device as consisting of a radial and of an axial p–i–n junction contacted in parallel, as illustrated by the equivalent scheme in Fig. 5.16b. A previous study of NWs ensemble LEDs containing radial and longitudinal InGaN MQWs has demonstrated that the spectral properties of the EL depend on which MQW system is preferentially injected with carriers (Adv. Mater. 23 (2011) 3284). In our case, these effects may be related to the resistance of the p-type GaN layer separating the metal contact from the axial junction. As the latter is more distant from the metal p-type contact, we suggest that the increase of the series resistance with decreasing temperature due to acceptor de-activation is larger for the axial junction than for the radial junction. Therefore, only the EL from the radial MQWs is observed at low T.

5.3.5 On-chip integration

Besides application as a highly efficient light source, a second major area of interest is the use of NWs as nanoscale light sources for on-chip integration. A specific example is intra-chip communication that today uses copper interconnects that could be replaced with optical interconnects. Considerable efforts are already being made to develop laser sources integrated with Si for communication (Fang, 2006), and NW LEDs may have an important role to play in this field (Lagally & Blick, 2004)(H.-G. Park, 2008).

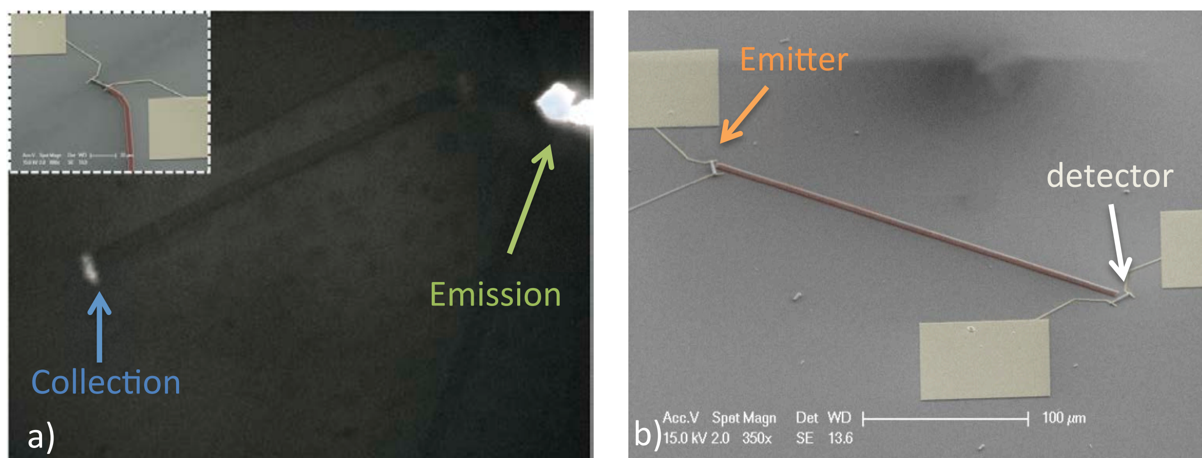

Figure 5.17. a) Optical image of the photonic circuit. The EL of the wire is efficiently guided by the SiN waveguide. (Scale bar, 20µm) The inset shows the SEM image of the contacted wire coupled to a waveguide (red). b) Integrated optical system based on emitter and detector wires.

To explore a practical application, we fabricated an electrically-driven device to light up a waveguide on a silicon chip. The results showed that MOVPE wire LEDs exhibit emission from the wire ends. Therefore, we can take advantage of this property to efficiently couple the EL to a waveguide at the end of the wire. The inset of figure 5.17a shows the LED device operated under forward bias injecting the EL emission into the Si_3N_4 waveguide. The Si_3N_4 waveguide has been fabricated as follows: first a 700 nm layer of Si_3N_4 is deposited by PEVD all over the sample, then a layer of 350nm a negative resist (ma-N 2401) is deposited by spin coating and electron-beam lithography is used to define the waveguide structure. The ma-N layer also acts as a mask for the following

reactive ion etching process to take out the rest of the Si_3N_4 layer. EL from the nanowire is efficiently guided by the waveguide, as shown on the optical image (Fig. 5.17a). This result indicates that the electrically-driven wire LED combined with the waveguide provides, in practice, a highly directional light beam in the integrated photonic circuit.

Finally, we propose a prototype of an integrated optical system based on wires connected by a waveguide. This kind of application should be highly desirable in quantum cryptography since the incorporation of quantum dots using heterostructures in nanowires has been successfully performed (Borgström, 2005)(Nguyen, 2011). The quantum dots embedded in the wire can be electrically addressed and produce single photon sources under electrical injection. Therefore, it would be possible to integrate one wire functioning as a single-photon source while placing a second wire acting as a single-photon detector.

Very preliminary results obtained showed that it is possible to guide light from one wire to another over a considerable distance of 200 μm. The optimization of high-sensitivity light detection as well as the fabrication device is under study.

Conclusions

In this chapter I presented a study of a photodetector and light emitters based on GaN wires grown by MOCVD containing InGaN/GaN MQW.

The wires morphology is that of an n-type stem followed by a non-intentionally doped GaN at the top of the wires surrounded by five radial InGaN/GaN quantum wells; the outer shell is either n-doped for photodetectors or p-doped for LED applications. From the structural point of view, STEM images showed the presence of well-defined m-plane QWs; in addition, a second system related to c-plane QWs is located at the top of the wires.

Photoluminescence from sample T929 presents two main contributions, one related to the n-GaN NBE (3.5 eV) and the other attributed to the MQW (3.05 eV). Photocurrent experiments confirmed the presence of the QWs, whereas the PC spectrum reveals a contribution below the NBE, which is not the case for reference sample (T629). OBIC measurements show that the photocurrent signal is exclusively located at the top of the wire for light excitation above and below the bandgap, attributed to the photocurrent generation in the intrinsic MQW region. The wire-based photodetector exhibits a high responsivity (8 x103 A / W) in the visible-to-UV spectral range and a frequency response with a -3 dB cutoff of 50 Hz.

Single wire p–i–n junction LEDs based on InGaN/GaN MQW core-shell structure were studied. PL measurements on single wires grown at different temperatures show a strong dependence on the excitation position along the wire; the bottom part of the wire presents a near band edge emission of GaN located at 3.5 eV while the energy of the subbandgap emission coming from the MQW revealed a shift between samples T1163 (3.15 eV) and T1184 (2.84 eV) due to the indium concentration in the QWs. The spatial distribution of the QW emission was studied on single wires by CL, finding that the axial MQWs emit at lower energy than the radial MQW system.

Electroluminescence experiments showed that only the axial polar MQWs are activated at RT with current $I<1\mu A$. When the current level is increased, carriers are more efficiently injected into the radial nonpolar MQWs, whose EL peak becomes progressively dominant. EL emissions related to radial MQW systems are in good agreement with PL measurements showing the possibility to tune the emission by varying the In content in the QWs during

growth. A photonic structure on silicon was demonstrated, showing that the light is efficiently guided from the wire to the end of the waveguide. Finally, we propose an integrated optical system based on the studied wires as we think that this kind of structure will enable a significant advance in complexity and functionality of the building blocks for future photonic nanocircuits.

Bibliography

Borgström, M. T., Zwiller, V., Müller, E., & Imamoglu, A. (2005). Optically Bright Quantum Dots in Single Nanowires. *Nano Letters*, *5*(7), 1439-1443. American Chemical Society. doi:10.1021/nl050802y

Calarco, R., Marso, M., Richter, T., Aykanat, A. I., Meijers, R., V D Hart, A., Stoica, T., et al. (2005). Size-dependent photoconductivity in MBE-grown GaN-nanowires. *Nano letters*, *5*(5), 981-4. doi:10.1021/nl0500306

Cao, X. a., Pearton, S. J., Zhang, a. P., Dang, G. T., Ren, F., Shul, R. J., Zhang, L., et al. (1999). Electrical effects of plasma damage in p-GaN. *Applied Physics Letters*, *75*(17), 2569. doi:10.1063/1.125080

Chen, H. M., & Chen, Y. F. (n.d.). Persistent photoconductivity in n -type GaN, 1-4.

Chen, R. S., Lu, C. Y., Chen, K. H., & Chen, L. C. (2009). Molecule-modulated photoconductivity and gain-amplified selective gas sensing in polar GaN nanowires. *Applied Physics Letters*, *95*(23), 233119. doi:10.1063/1.3264954

Chen, X. J., Perillat-Merceroz, G., Sam-Giao, D., Durand, C., & Eymery, J. (2010). Homoepitaxial growth of catalyst-free GaN wires on N-polar substrates. *Applied Physics Letters*, *97*(15), 151909. doi:10.1063/1.3497078

Davydov, V. Y., Klochikhin, A. A., & Emtsev, V. V. (2002). Rapid Research Note Band Gap of InN and In-Rich In x Ga 1Àx N alloys (0 . 36 < x < 1). *Physics*, *6*(2), 6-8.

Fang, A. W., Park, H., Cohen, O., Jones, R., Paniccia, M. J., & Bowers, J. E. (2006). Electrically pumped hybrid AlGaInAs-silicon evanescent laser. *Optics Express*, *14*(20), 9203. OSA. doi:10.1364/OE.14.009203

Fasol, S. N. (2001). The Blue Laser Diode. The Complete Story. *Measurement Science and Technology*, *12*(6), 755-756. doi:10.1088/0957-0233/12/6/703

Garrido, J. a, Monroy, E., Izpura, I., & Muñoz, E. (1998). Photoconductive gain modelling of GaN photodetectors. *Semiconductor Science and Technology*, *13*(6), 563-568. doi:10.1088/0268-1242/13/6/005

Glas, F. (2006). Critical dimensions for the plastic relaxation of strained axial heterostructures in free-standing nanowires. *Physical Review B*, *74*(12), 2-5. doi:10.1103/PhysRevB.74.121302

Jain, S. C., Willander, M., Narayan, J., & Overstraeten, R. V. (2000). III–nitrides: Growth, characterization, and properties. *Journal of Applied Physics*, *87*(3), 965. doi:10.1063/1.371971

Katz, O., Bahir, G., & Salzman, J. (2004). Persistent photocurrent and surface trapping in GaN Schottky ultraviolet detectors. *Applied Physics Letters*, *84*(20), 4092. doi:10.1063/1.1753056

Koester, R, Hwang, J. S., Durand, C., Dang, D. L. S., & Eymery, J. (2010). Self-assembled growth of catalyst-free GaN wires by metal-organic vapour phase epitaxy. *Nanotechnology*, *21*(1), 015602. doi:10.1088/0957-4484/21/1/015602

Koester, Robert, Hwang, J.-seok, Salomon, D., Chen, X., Bougerol, C., Barnes, J.-paul, Le, D., et al. (2011). M-Plane CoreÀShell InGaN/GaN Multiple-Quantum-Wells on GaN Wires for Electroluminescent Devices. *Nano*.

Kuo, B.-T. L.-H. Y. and Y.-K. (2005). Vegard's law deviation in band gaps and bowing parameters of the wurtzite III-nitride ternary alloys. *Proceedings of SPIE*, *5628*(1), 296-305. doi:doi:10.1117/12.575300

Lagally, M. G., & Blick, R. H. (2004). Materials science: a "bed of nails" on silicon. *Nature*, *432*(7016), 450-1. doi:10.1038/432450a

Li, Q., & Wang, G. T. (2010). Spatial distribution of defect luminescence in GaN nanowires. *Nano letters*, *10*(5), 1554-8. doi:10.1021/nl903517t

Minot, E. D., Kelkensberg, F., van Kouwen, M., van Dam, J. a, Kouwenhoven, L. P., Zwiller, V., Borgström, M. T., et al. (2007). Single quantum dot nanowire LEDs. *Nano letters*, *7*(2), 367-71. doi:10.1021/nl062483w

Monroy, E., & Omn, F. (2003). Wide-bandgap semiconductor ultraviolet photodetectors. *Semiconductors*, *33*.

Nakamura, Shuji. (1995). InGaN / AlGaN blue-light-emitting diodes, *13*(August 1994), 705-710.

Nakamura, S. (1998). The Roles of Structural Imperfections in InGaN-Based Blue Light-Emitting Diodes and Laser Diodes. *Science*, *281*(5379), 956-961. doi:10.1126/science.281.5379.956

Nguyen, H. P. T., Cui, K., Zhang, S., Fathololoumi, S., & Mi, Z. (2011). Full-color InGaN/GaN dot-in-a-wire light emitting diodes on silicon. *Nanotechnology*, *22*(44), 445202. doi:10.1088/0957-4484/22/44/445202

Park, H.-G., Barrelet, C. J., Wu, Y., Tian, B., Qian, F., & Lieber, C. M. (2008). A wavelength-selective photonic-crystal waveguide coupled to a nanowire light source. *Nature Photonics*, *2*(10), 622-626. doi:10.1038/nphoton.2008.180

Qian, FangPark, Hong-gyu, Dong, Y., Ding, Y., Li, Y. A. T., Cak, S. G., Wang, Z. L. I. N., et al. (2008). Multi-quantum-well nanowire heterostructures for wavelength-controlled lasers. *Materials Science*, 701-706. doi:10.1038/nmat2253

Reshchikov, M. a., & Morkoç, H. (2005). Luminescence properties of defects in GaN. *Journal of Applied Physics*, *97*(6), 061301. doi:10.1063/1.1868059

Sanford, N. a., Blanchard, P. T., Bertness, K. a., Mansfield, L., Schlager, J. B., Sanders, a. W., Roshko, a., et al. (2010). Steady-state and transient photoconductivity in c-axis GaN nanowires grown by nitrogen-plasma-assisted molecular beam epitaxy. *Journal of Applied Physics*, *107*(3), 034318. doi:10.1063/1.3275888

Soci, C., Zhang, a, Xiang, B., Dayeh, S. a, Aplin, D. P. R., Park, J., Bao, X. Y., et al. (2007). ZnO nanowire UV photodetectors with high internal gain. *Nano letters*, *7*(4), 1003-9. doi:10.1021/nl070111x

Wilson, T., & McCabe, E. M. (1987). Theory of optical beam induced current images of defects in semiconductors. *Journal of Applied Physics*, *61*(1), 191. doi:10.1063/1.338853

Yoshimoto, N., Matsuoka, T., Sasaki, T., & Katsui, a. (1991). Photoluminescence of InGaN films grown at high temperature by metalorganic vapor phase epitaxy. *Applied Physics Letters*, *59*(18), 2251. doi:10.1063/1.106086

Conclusions and perspectives

This thesis work is focused on the design, fabrication and characterization of optoelectronic devices based on III-N nanowires. In particular, I have studied two different device architectures namely devices based on single nanowires or ensemble of nanowires for photodetection and light emission applications.

Concerning photodetectors based on nanowire arrays, I have demonstrated that their responsivity exceeds that of thin film counterparts. This is mainly due to the device geometry which favors the light absorption, when the light travels along the diffusive path through the nanowire array, multiple light scattering occurs between the wires increasing the number of photons converted to electron-hole pairs. The photodetector can be futher improved in the following ways:

It is necessary to improve the in-plane conductivity and the optical transparency of the top contact. Since ITO has a poor transparency in the UV range, another type of conductive-transparent contact must be studied. One possibility is the use of carbon nanotubes networks or graphene [Byung-Jae Kim, 2011]. One important issue to take full advantage of the nanowires high quality material is to develop a dedicated passivation of the nanowire surface. Indeed, the nanowire surface induces trapping effects lowering the photodetector bandwidth as well as non-radiative recombination channels limiting the efficiency of carrier collection. To passivate the surface, one possible way is use another filling material [Guo W., 2011] or to switch to a core-shell geometry. In addition, a p-n core-shell structure will enable efficient carrier collection over a short distance defined by the nanowire diameter, while the optical absorption will take place on a much larger distance defined by the nanowire length. Further investigations can be performed to reduce the absorption losses by controlling the spacing between the nanowires and their position on the substrate as well as their diameters.

I have demonstrated a UV photodetector based on nanowires containing multiple GaN/AlN quantum discs. For this study two heterostructured samples were analyzed and compared to a n-i-n reference sample. The structural analyses revealed a significant variation of the quantum discs thickness as well as the presence of a lateral GaN surrounding shell on one sample which was absent on the other sample. Photoluminescence experiments performed on single nanowires have shown a spectral contribution below the band-gap for both samples. An emission above the band-gap were only found on the sample without the surrounding shell. Spatially resolved cathodoluminescence allowed to clarify and confirm the origin of both contributions. I have shown that, the surrounding shell has also a strong impact on the electronic transport along the nanowire axis providing a leakage channel for electrons. However, if no GaN shell is present, the electrons are forced to pass through the quantum disc region. As a result, a reproducible negative differential resistance could be observed up to 250K for the first time in AlN/GaN material system. Third, the photoresponse coming from the shell-free nanowires present a sub-band-gap contribution related to the interband absorption between the confined states in the large Qdiscs, while the presence of the surrounding shell masks the spectral contribution from these Qdiscs.

Future efforts in this area will address the design and fabrication of intersubband photodetectors based on the absorption between electronic confined states in the conduction band. For these detectors, the expected response lies in the mid and near infrared spectral range. A first approach can be done by processing nanowires ensembles following the strategy adopted for the visible blind photodetector described in chapter 3. However, special attention should be paid to the optimization of the nanowire epitaxy. Indeed, to avoid the excessive broadening of the intersubband absorption, the nanowires should have the same diameter as well as the quantum disc thickness. Another aspect that needs to be perfectly controlled is the doping of the active region to ensure an efficient intersubband absorption in the Qdiscs.

In the last part of this work I have demonstrated the potential of wires containing radial InGaN/GaN MQW for photodetection and light emission applications. First I have discussed the realization of a UV photodetector based on an n-i-n structure. The photocurrent response exhibits a contribution below GaN bandgap related to the absorption in the QWs. Using the OBIC mapping technique, I have shown that the photogeneration for excitations above and below the bandgap is exclusively located in the active region. Finally I have carried out a study of a

single wire LED structure. This allowed me to understand some fundamental aspects, such as the injection mechanism, the behavior at different current levels and the temperature dependence of the electroluminescence. For this purpose, three samples with In content from 16% to 24% were analyzed. I have observed that the photoluminescence emission shifts to lower energy when the indium concentration present in the active region is increased. Electroluminescence experiments have revealed two main contributions attributed to the axial and radial MQW systems: at low current levels the injection take place into the axial MQW system while a high current injection carriers are more efficiently injected into the radial nonpolar MQWs. Moreover, I have shown that the electroluminescence related to the radial MQW system is in good agreement with the PL spectra of these wires.

Future work will be concentrated on the vertical integration of nanowire LEDs. It is predicted that the light extraction from LEDs based on vertical nanowire arrays can be substantially improved by controlling the spacing and the position of the wires on the surface, thus avoiding the light being trapped by total internal reflection. Another interesting area of work is the planar integration of multiple wires by dielectrophoresis. One of the main advantages of this technique is the possibility to align the wires with a minimum energy configuration within the applied field, such as along the field lines. This will dramatically increase the throughput of the fabrication since the use of e-beam lithography will be no longer necessary, especially this could be of great interest for on-chip integration of nanowire devices.